Universitat de Girona

3D UNDERWATER SLAM USING SONAR AND LASER SENSORS

Albert Palomer Vila

Doctoral Thesis

3D Underwater SLAM Using Sonar and Laser Sensors

Albert Palomer Vila

2018

Doctoral Thesis

3D Underwater SLAM Using Sonar and Laser Sensors

Albert Palomer Vila

2018

Doctoral Program in Technology

Supervised by:

Pere Ridao
Josep Forest
David Ribas

Thesis submitted to University of Girona
in fulfillment of the requirements for the degree of

Doctor of Philosophy

Certificate of Thesis Direction

Dr. Pere Ridao, director of Computer Vision and Robotics Research Group (VICOROB) and member of Departament d'Arquitectura i Tecnologia de Computadors of Universitat de Girona, Dr. Josep Forest, member of Departament d'Arquitectura i Tecnologia de Computadors of Universitat de Girona and Dr. David Ribas former member of Departament d'Arquitectura i Tecnologia de Computadors of Universitat de Girona,

Declare:

That the work entitled *3D Underwater SLAM Using Sonar and Laser Sensors* presented by Albert Palomer Vila to obtain the degree in Doctor of Philosophy has been developed under my supervision and fulfills the requirements to obtain the International Mention.

Therefore, in order to certify the aforesaid statement, I sign this document.

Girona, October 2018

Dr. Pere Ridao

Dr. Josep Forest

Dr. David Ribas

Al meu avi, amb qui m'agradaria
haver passat més hores al mar,
navegant amb els velers que construïa

Acknowledgments

The path that has led me to this document and publications has been some times hard and frustrating, sometimes easy and fun. With these lines I want to acknowledge the people that has been helping me and/or enjoying with me during these years.

Vull començar agraint el suport dels meus pares, que són els artífexs de que jo pogués estudiar tants anys d'universitat sense haver de preocupar-me de com mantenir-me. Al cap i a la fi, gràcies per posar la base en la qual he pogut construir no només el doctorat, sinó també la meva vida. També vull agrair als meus germans: l'Ernest sap què és el que he passat ja que fa uns anys ell hi va passar, i en Pau, tot i no ser doctor, també sap el que és treballar de valent i ser un exemple, sobretot ara per cuidar el nou de casa, en Kai. Vull fer també extensiu aquest agraïment a la resta de la meva família àvies, tietes, tiets, cosines i cosins ja que algun cop han hagut de sofrir els mals quan alguna cosa de la tesi no funcionava. Per últim, vull agrair molt especialment a l'Anna Riera, que fa un temps va prendre l'esbojarrada decisió de compartir part de la vida amb mi i amb qui tinc moltíssimes ganes de fer projectes ara que ella està a Banyoles i jo hauré acabat la tesi.

Aquesta tesi no hauria arribat a bon port si no fos pel suport incondicional i immens del laboratori de robòtica submarina CIRS. El primer és agrair a en Pere Ridao, el meu director i tutor, qui per culpa meva, ha envellit uns anys més ràpid del que li toca tot i trobar sempre una solució als diferents reptes/preguntes que li plantejava. També vull agrair especialment a en David Ribas, que m'ha acompanyat des del principi amb les indicacions més precises que mai ningú m'ha donat, i a en Josep Forest que m'ha ajudat amb tota la part del calibratge del sistema d'escaneig làser. La vostra codirecció de la tesi ha estat 100% necessària, sense vosaltres això no hauria estat el mateix. També vull agrair a la resta de gent del CIRS, en especial en Guillem i en Jep amb qui vàrem començar Enginyeria Industrial fa 12 anys. Sembla que al final he guanyat jo la *Cursa de Cargols* ja que he estat l'últim en defensar. Vull agrair també l'equip de hardware, Lluís i Carles, que fan esforços per arreglar tot el que els de software xafem. A en Narcís i la Tali perquè cada cop que toques el robot i tens un dubte saben com ajudar-te. A Juan David por su ayuda, sobretodo en errores de compilación que son imposibles de entender. A en Nuno perquè m'ha escoltat quan necessitava altres ulls per entendre el món de la visió per computador. A en Marc perquè, a més de fer-me anar a l'Eurathlon, creu que l'escàner laser té un lloc en els productes IQUA Robotics. Als que ja no estan al laboratori, Arnau, Aggelos i Eric, perquè quan podíeu em desencallàveu de l'embolic on fos. També vull agrair a la gent de visió i als d'Opsis que de tant en tant també aguanten alguna que altra pregunta així com l'equip del P4, Joseta, Mireia, Annes, Bego i Olga, per fer que sigui possible centrar-nos en la recerca i estalviar-nos tots els problemes burocràtics. Finally the ones who started

after me: Eduard, Klemen, Dina, Khadidja and Roger. Your time will come, persevere and you will finish.

I want to thank Chris for the opportunity to visit Rhode Island, give me my first at sea experience on board the R/V Endeavor and introduce me to Ocean Exploration Trust (OET) and the E/V Nautilus. Without meeting you during those 4 months, I would not be where I am now. In the same way, I want to thank his team: Ian, Clara, Dave, Kris, Emanuele and Ben. Some because they helped me during my stay in Rhode Island, some because they made my days at sea on board the E/V Nautilus an even greater experience. From OET I want to thank specially Nicole who every year helps me get back to the Nautilus and enjoy the ocean exploration some more days.

Vull continuar donant les gràcies a amics i amigues que han fet més lleugera aquesta tesi, especialment a la gent de la Colla Castellera Xoriguers de la UdG, sense ells el meu pas per la universitat no hauria estat el mateix. Gràcies també a la ja Dra. Imma Noguerola, amb qui vam compartir part del camí cap al doctorat, el principi del meu i el final del seu. Als amics de Banyoles (a qui no llistaré per no deixar-ne cap) amb qui fa dècades que ens aguantem, però també amb els que han entrat en els últims anys. Un especial record per la Mònica que mai vaig poder anar a explicar a la seva classe el que faig.

Last, I would like to thank the anonymous reviewers that contributed to improve this thesis with their invaluable comments. Also the many reviewers that contributed to the different publications derived from this work.

Finally I would like to thank the agencies that partially funded this work: the FPI 2012 grant BES-2012-053857 PhD grant from the Spanish Ministry of Science, the National projects COMAROB and ARCHROV as well as the European Comission projects TRIDENT, MORPH and STRONGMAR.

List of Publications

Publications in the compendium

The presented thesis is a compendium of the following research articles:

- **Albert Palomer**, Pere Ridao, and David Ribas. "Multibeam 3D Underwater SLAM with Probabilistic Registration". In: *Sensors* 16.4 (2016). DOI: 10.3390/s16040560
  Quality index: JCR2016 Instruments & Instrumentation, Impact Factor: 2.677, Q1.
  Contributions: This paper presents a full three-dimensional (3D) Simultaneous Localization and Mapping (SLAM) using a multibeam echosounder. The paper, an extension of [2], extends to 3D the previously presented Probabilistic Iterative Closest Point (pICP) algorithm and proposes an Extended Kalman Filter (EKF) SLAM framework to produce high consistency maps. The proposed algorithm is tested with two data sets from two different Autonomous Underwater Vehicles (AUVs), one with a down-looking multibeam configuration (i.e. bathymetric two-and-a-half-dimensional (2.5D) maps) and the other one with the multibeam mounted on a pan and tilt (i.e. 3D maps).
  Author contributions: The author of the thesis took as starting point the work previously done in the laboratory [2]. In that publication the SLAM algorithm was adabted only to the specific robot and dataset reported there. In this publication the thesis author developped new subsampling techniques, reformulated the odometry measurements to incorporate the absolute measurements (depth and orientation), expanded the algorithm interface to work with other robots and finally, adapted the sub-map creation process by incorporating the normal occupancy patch closing condition as well as the integration with pan and tilt steered multibeam units. Moreover, the author changed the error metric evaluation to a more adequate one [3] for the bathymetric experiments and incorporated new results supporting the improvements, specially presenting 3D reconstructions. This improvements were done with the supervision of the other authors. Finally, the author wrote the publication which was reviewed by the other authors.

- **Albert Palomer**, Pere Ridao, Josep Forest, and David Ribas. "Underwater Laser Scanner: Ray-based Model and Calibration". Submitted to IEEE/ASME Transactions on Mechatronics on November 2017
  Quality index: JCR2016 Automation & Control systems, Impact Factor: 4.357, Q1.

Contributions: This paper presents a real-time underwater laser scanner that uses a camera and a laser line steered with a galvanometer and projects the light through a flat viewport. In this paper we develop a ray-based model of the sensor and a calibration procedure to estimate the different parameters of the sensor's model. Moreover, we also use an elliptical cone to synthesize the ray-based model for the different angles of incidence between the laser and the viewport, decreasing the computation time of the 3D points.
Author contributions: The author of this thesis did all the work for this publication with the supervision of the other authors.

- **Albert Palomer**, Pere Ridao, and David Ribas. "Inspection of an Underwater Structure using Point Cloud SLAM with an AUV and a Laser Scanner". Submitted to Journal of Field Robotics on July 2018. 2018
  Quality index: JCR2016 Robotics, Impact Factor: 4.882, Q1.
  Contributions: This paper presents the application of the newly developed underwater laser scanner in a real-time SLAM. This work pushes the stat of the art forward by demonstrating in a realistic environment that using the developed laser scanner AUVs can produce high resolution maps of structures in real time. The SLAM algorithm is demonstrated in a realistic environment in a water tank using a subsea infrastructure mock-up and the Girona 500 AUV with the laser scanner mounted in the payload area.
  Author contributions: The author of this thesis did all the work for this publication with the supervision of the other authors.

- **Albert Palomer**, Pere Ridao, Dina Youakim, David Ribas, Josep Forest, and Yvan Petillot. "3D Laser Scanner for Underwater Manipulation." In: *Sensors* 18.4 (2018), pages 1–14. DOI: 10.3390/s18041086
  Quality index: JCR2016 Instruments & Instrumentation, Impact Factor: 2.677, Q1.
  Contributions: This paper presents the application of the newly developed underwater laser scanner into two different manipulation tasks. In this work the scanner is used as the robot unique 3D perception sensor. The complete system is demonstrated in two applications: 1) an 8 degrees of freedom (DoF) underwater manipulation moving in a water tank with apriori unknown obstacles and 2) and 8 DoF intervention AUV (I-AUV) grasping an object at the bottom of a water tank.
  Author contributions: The thesis author designed and implemented all the software and methods related to laser scanner calibration as well as the laser scanner to arm calibration. He also designed and performed the experiments of the eight DoF manipulation system together with Pere Ridao, Dina Youakim and Yvan Petillot. Moreover, he also designed and performed the Underwater Vehicle-Manipulator System (UVMS) experiments together with Dina, Pere and members of the MERBOTS consortium. Finally Albert wrote the paper with some contributions from Dyna and the supervision of Pere Ridao.

as well as the book chapter:

- **Albert Palomer**, Pere Ridao, David Ribas, and Josep Forest. "Underwater 3D laser scanners: The deformation of the plane". In: *Sensing and Control for Autonomous Vehicles: Applications to Land, Water and Air Vehicles*. Edited by Thor

I. Fossen, Kristin Y. Pettersen, and Henk Nijmeijer. Volume 474. Springer International Publishing, 2017, pages 73–88. DOI: 10.1007/978-3-319-55372-6_4
Contributions: This book chapter presents a study on the deformation that a laser line projector from an underwater laser scanner suffers when it passes through a flat viewport at different incidence angles. The work proposes an elliptical cone representation for the projected light. This surface better represents the projected light than a plane (the surface used in other laser scanner works) because it can represent the wide variety of curvatures of the projected light, including a line.
Author contributions: The author of this thesis did all the work for this publication with the supervision of the other authors.

Publications derived from this thesis

The work developed in this thesis also led to the following publications:

- Simone Zandara, Pere Ridao, David Ribas, Angelos Mallios, and **Albert Palomer**. "Probabilistic Surface Matching for Bathymetry Based SLAM". in: *Proceedings of the IEEE International Conference on Robotics and Automation*. 2013

- **Albert Palomer**, Pere Ridao, David Ribas, Angelos Mallios, Nuno Gracias, and Guillem Vallicrosa. "Bathymetry-Based SLAM with Difference of Normals Point-Cloud Subsampling and Probabilistic ICP Registration". In: *Proceedings of the IEEE OCEANS 2013 conference*. 2013. DOI: 10.1109/OCEANS-Bergen.2013.6608091

- **Albert Palomer**, Pere Ridao, David Ribas, Angelos Mallios, and Guillem Vallicrosa. "Octree-Based Subsampling Criteria for Bathymetric SLAM". in: *Proceedings of the XXXV Jornadas de Automática* (2014), pages 1–6

Patents derived from this thesis

The work developed in this thesis also led to the following patent which is still pending on approval:

- **Albert Palomer**, David Ribas, Pere Rodríguez, and Josep Forest. "Conjunto de Escaneo por Láser, Vehículo y Procedimiento de Escaneo por Láser Correspondientes". P201730372. Mar. 2017

Other publications

Parallel work at the time of this thesis led to the following publications:

- **Albert Palomer**, Pere Ridao, David Ribas, Angelos Mallios, and Guillem Vallicrosa. "A comparison of G2o graph SLAM and EKF pose based SLAM with bathymetry grids". In: *IFAC Proceedings Volumes (IFAC-PapersOnline)*. Volume 9. PART 1. 2013. DOI: 10.3182/20130918-4-JP-3022.00065

- Nuno Gracias, Pere Ridao, Rafael Garcia, Javier Escartin, Franca Cibecchini, Ricard Campos, Marc Carreras, David Ribas, Lluis Magi, **Albert Palomer**, Tudor Nicosevici, Ricard Prados, Laszlo Neumann, Francesco De Filippo, and Angelos Mallios. "Mapping the Moon: Using a lightweight AUV to survey the site of the 17th Century ship 'La Lune'". In: *Proceedings of the MTS/IEEE OCEANS conference*. 2013

- Guillem Vallicrosa, **Albert Palomer**, David Ribas, and Pere Ridao. "Realtime AUV Terrain Based Navigation with Octomap". In: *XXXIV Jornadas de Automática*. Universitat de Girona (UdG). 2013

- Guillem Vallicrosa, **Albert Palomer**, David Ribas, and Pere Ridao. "Realtime AUV Terrain Based Navigation with Octomap in a natural environment". In: *ROBOT 2013: First Iberian Robotics Conference*. 2013, pages 41–53

- Guillem Vallicrosa, **Albert Palomer**, David Ribas, and Pere Ridao. "Towards Realtime AUV SLAM with Occupancy Grids". In: *Fifth International Workshop on Marine Technology (MARTECH)*. 2013

- Enric Galceran, Sharad Nagappa, Marc Carreras, Pere Ridao, and **Albert Palomer**. "Uncertainty-driven Survey Path Planning for Bathymetric Mapping". In: *IEEE/RSJ International Conference on Intelligent Robots and Systems*. Tokyo Big Sight, Japan, 2013, pages 6006–6012. DOI: 10.1109/IROS.2013.6697228

- Guillem Vallicrosa, Pere Ridao, David Ribas, and **Albert Palomer**. "Active Range-Only Beacon Localization for AUV Homing". In: *IEEE International Conference on Intelligent Robots and Systems ICRA*. Chicago, IL, USA, 2014, pages 2286–2291

- Guillem Vallicrosa, **Albert Palomer**, David Ribas, and Pere Ridao. *Realtime AUV terrain based navigation with octomap in a natural environment*. Volume 252. 2014. DOI: 10.1007/978-3-319-03413-3_4

- Narcís Palomeres, Antonio Peñalver, Miquel Massot-Campos, Guillem Vallicrosa, Pep Lluís P.L. Negre, J.J. Javier Fernández, Pere Ridao, Pedro J. P.J. Sanz, Gabriel Oliver, and **Albert Palomer**. "I-AUV Docking and Intervention in a Subsea Panel". In: *IEEE International Conference on Intelligent Robots and Systems (IROS)*. 2014, pages 2279–2285. DOI: 10.1109/IROS.2014.6942870

- **Albert Palomer**, Pere Ridao, David Ribas, and Guillem Vallicrosa. "Multi-beam Terrain / Object Classification for Underwater Navigation Correction". In: *MTS/IEEE OCEANS*. Genova, 2015. DOI: 10.1109/OCEANS-Genova.2015.7271587

- Ricard Campos, Nuno Gracias, **Albert Palomer**, and Pere Ridao. "Global Alignment of a Multiple-Robot Photomosaic using Opto-Acoustic Constraints". In: *NGCUV2015 Girona*. Volume 48. 2. Elsevier Ltd., 2015, pages 20–25. DOI: 10.1016/j.ifacol.2015.06.004

Acronyms

2.5D	two-and-a-half-dimensional.
2D	two-dimensional.
3D	three-dimensional.
ACFR	Australian Center for Field Robotics.
AHRS	Attitude and Heading Reference System.
ASC	Autonomous Surface Craft.
AUV	Autonomous Underwater Vehicle.
CBEE	Consistency Based Error Evaluation.
CIRS	Centre d'Investigació en Robòtica Submarina.
DoF	degrees of freedom.
DR	Dead Reckoning.
DVL	Doppler Velocity Log.
EKF	Extended Kalman Filter.
ERL	European Robotics League.
FLS	Forward-Looking Sonar.
GIB	GPS Intelligent Buoys.
GPS	Global Positioning System.
I-AUV	intervention AUV.
ICP	Iterative Closest Point.
IMR	Inspection, Maintenance and Repair.
INS	Inertial Navigation System.
IR	infrared.
LBL	Long Baseline.
OMPL	Open Motion Planning Library.
OSL	Ocean Systems Laboratory.
pICP	Probabilistic Iterative Closest Point.
ROV	Remote Operated Vehicle.
SAUC-E	Student Autonomous Underwater Challenge - Europe.
SfM	Structure from Motion.
SLAM	Simultaneous Localization and Mapping.
TBN	Terrain-Based Navigation.
UdG	Universitat de Girona.

USBL	Ultra-Short Baseline.
UVL	Underwater Vision Lab.
UVMS	Underwater Vehicle-Manipulator System.
VICOROB	Computer Vision and Robotics.

List of Figures

List of Tables

Contents

Abstract

The 3D perception and mapping problem are very closely related with the robot localization and has not been yet solved up to a degree that allow AUVs to interact with complex environments safely. By providing AUVs with better 3D perception and improving their localization the usage of AUVs in tasks such as Inspection, Maintenance and Repair (IMR) can increase. Since these tasks are currently done with Remote Operated Vehicles (ROVs), this would produce an economical impact in the operational cost because AUV operations are cheaper than ROV ones.

This thesis presents different solutions to the 3D perception and mapping problem using acoustic and laser sensors. The first part of this thesis presents a full 3D EKF SLAM using a multibeam echosounder. In this algorithm, the swath profiles of the multibeam are combined with the robot DR navigation to produce sub-maps of the area to explore. The central position of each sub-map is stored in a pose-based EKF SLAM. When two sub-maps are overlapping, a pICP registration algorithm estimates their relative position. This algorithm coarsely aligns the sub-maps using a point-to-point error metric and then, it uses a point-to-plane error metric to refine the alignment. Moreover, the association complexity of the pICP is decreased from $O(n^2)$ to $O(n)$ using an heuristic based on the probabilistic representation of points. The results of the pICP registration algorithm are used as observations between the different positions in the EKF. This SLAM framework is tested in different experiments using either a down-looking multibeam configuration producing 2.5D bathymetric maps or with the multibeam mounted on a pan and tilt actuator scanning from a down-looking to a forward looking configuration producing 3D scans.

The second part of the thesis presents a new underwater 3D laser scanner to increase the 3D perception resolution, accuracy and frame rate when compared to the multibeam echosounder. The underwater laser scanner consists of a camera and a laser line projector that is scanned across an area of interest using a mirror actuated with a galvanometer, both sealed with flat viewports. The use of flat viewports produce distortion in the projected laser light. This deformation is studied by proposing a ray-based model of the sensor. In this thesis we propose to use an elliptical cone to represent the surface where the light travels underwater. The elliptical cone represents the underwater laser light better than a plane (the surface used in similar underwater laser scanners) because it can represent the overall curvatures of the projected light, including a straight line. Then, we propose a calibration procedure to estimate the parameters of the ray-based model as well as the elliptical cones for the different incident angles between the laser and the viewport. The

experimental results show that the scanner has a sub-millimetric precision and that the use of an elliptical cone not only produces a better representation of the underwater light than a plane, but also outperforms the triangulation using the ray-based model without losing accuracy.

Finally, the thesis presents two practical applications of the newly developed underwater laser scanner. First, we use the scanner in a pose-based EKF SLAM where the position of different scans are corrected using a feature-based coarse registration refined with an Iterative Closest Point (ICP). The developed EKF SLAM is tested in an inspection of an underwater pipe and valve structure with the Girona 500 AUV and the laser scanner in the water tank. Second, the scanner is used in conjunction with two different underwater manipulation systems. The first manipulation experiment uses a fixed-base 8 DoF manipulator with the task of moving cyclically through 3 different way-points without colliding with the a priory unknown objects in the scene. In this experiment, the scanner is used to update the map that the planner uses to compute safe trajectories. The second manipulation experiments uses a 4 DoF manipulator mounted onto Girona 500 AUV to pick up an amphora from the bottom of the water tank. In this experiment the scanner is used to detect the amphora pose and compute the grasping approach pose as well as the grasping pose.

Resum

La percepció tridimensional (3D) i el mapeig són problemes estretament relacionats amb la localització del robot i encara no han estat solucionats fins al punt de permetre als vehicles submarins autònoms (AUVs) interactuar amb entorns complexos de manera segura. Proveint els AUVs d'una millor percepció 3D i una millor localització, l'ús dels AUVs en tasques d'inspecció, manteniment i reparació (IMR) pot incrementar-se. Donat que aquestes tasques actualment es fan amb vehicles submarins operats remotament (ROVs), això produiria un impacte econòmic en el cost d'operació perquè el cost d'operar un AUV és menor que el d'un ROV.

Aquesta tesi presenta diferents solucions al problema de percepció 3D i mapeig fent servir sensor acústics i de làser. La primera part d'aquesta tesi presenta un algorisme 3D de localització simultània i mapeig (SLAM) basat en un filtre de Kalman estès (EKF) i fent servir una sonda acústica multifeix. L'algorisme combina els perfils del terra del multifeix amb la navegació per estima (DR) per produir submapes de l'àrea d'exploració. La posició central de cada submapa es guarda en un EKF SLAM. Quan dos submapes es solapen, la formulació probabilística del mètode de registre punt més proper iteratiu (pICP) n'estima la posició relativa. Aquest algorisme fa servir una associació punt a punt per obtenir una primera alineació aproximada dels submapes i, després, utilitza una associació punt a pla per tal de refinar l'alineament. A més a més, la complexitat de l'associació del pICP es redueix de $O(n^2)$ a $O(n)$ utilitzant una heurítsica basada en la representació probabilística dels punts. Els resultats del pICP es fan servir com a observacions relatives entre les diferents posicions de l'EKF. Aquest algorisme de SLAM s'ha provat en diferents experiments fent servir sonars multifeix muntats en diferents configuracions: en el muntatge convencional mirant cap al fons marí per produir mapes batimètrics dos-i-mig-dimensionals (2.5D) així com muntat en un actuador rotatiu de dos eixos movent el multifeix iterativament des de la posició inferior cap a la posició frontal produint mapes 3D.

La segona part de la tesi presenta un escàner làser submarí 3D per incrementar, respecte del sensor acústic multifeix, la resolució, precisió i freqüència de la percepció 3D. L'escàner làser submarí està format per una càmera i un projector de línia làser que escaneja una àrea d'interès fent servir un mirall actuat per un galvanòmetre, ambdós sellats per una finestra plana. L'ús d'aquests tipus de finestra produeix una distorsió en la llum làser projectada. Aquesta deformació s'estudia creant un model del sensor basat en raigs. En aquesta tesi proposem utilitzar un con el · líptic per representar la superfície per la qual la llum es propaga a sota l'aigua. El con el · líptic representa millor el feix de llum submarí

que un pla (la superfície típicament utilitzada en altres escàners làser submarins) perquè pot representar els diferents graus de curvatura de la llum projectada, incloent una línia recta. També proposem un mètode de calibratge per estimar els paràmetres del model basat en raigs així com dels cons el · líptics pels diferents angles d'incidència entre la finestra i el làser. Els resultats experimentals mostren com l'escàner làser té una precisió submil · limètrica i que l'ús del con el · líptic no només produeix una millors representació que un pla, sinó que també millora el temps de càlcul, sense perdre precisió, quan es compara amb el model de raigs.

Finalment, aquesta tesi presenta dues aplicacions pràctiques d'ús de l'escàner làser submarí. Primer, el sensor es fa servir en un EKF SLAM de posició on les posicions del robot corresponents a cada escaneig es corregeixen mitjançant un registre bast de núvol de punts basat en característiques que es refinen amb un registre de punt més proper iteratiu (ICP). L'algorisme d'EKF SLAM es posa a prova en la inspecció d'una estructura de tubs i vàlvules amb el robot Girona 500 AUV i l'escàner làser en un tanc d'aigua. En segon lloc, l'escàner es fa servir conjuntament amb dos sistemes de manipulació diferents. El primer experiment de manipulació fa servir un manipulador de 8 graus de llibertat (DoF) que té la tasca de moure's de manera cíclica a tres posicions sense xocar amb els objectes de l'entorn, desconeguts a priori. En aquest experiment, l'escàner làser es fa servir per actualitzar el mapa que l'algorisme planificador de trajectòries fa servir per calcular trajectòries segures. El segon experiment de manipulació fa servir un manipulador de 4 DoF muntat en el Girona 500 AUV per agafar una àmfora del fons del tanc d'aigua. En aquest experiment l'escàner làser s'utilitza per detectar l'àmfora i calcular-ne la posició d'aproximació i la d'agafar l'objecte.

Resumen

La percepción tridimensional (3D) y el mapeo son problemas íntimamente relacionados con la localización del robot y aún no se han solucionado hasta el punto de permitir a los robots autónomos submarinos (AUVs) interactuar con entornos complejos de manera segura. Dotando los AUVs de una mejor percepción 3D y una mejor localización, el uso de AUVs en tareas de inspección, mantenimiento y reparación (IMR) puede incrementar. Dado que actualmente estas tareas se hacen con robots submarinos operados remotamente (ROVs), esto produciría un impacto económico en el coste de operación ya que el coste de los AUVs es menor que el de los ROVs.

Esta tesis presenta distintas soluciones al problema de la percepción 3D y el mapeo utilizando sensores acústicos y de láser. La primera parte de la tesis presenta un algoritmo 3D de localización simultánea y mapeo (SLAM) basado en un filtro de Kalman extendido usando una sonda acústica multihaz. El algoritmo combina los perfiles del fondo marino de la sonda multihaz con la navegación por estima (DR) para producir submapas del área de exploración. La posición central de cada submapa se guarda en un EKF SLAM. Cuando dos submapas se solapan, la formulación probabilística del método de registro punto más próximo iterativo (pICP) estima su posición relativa. Este algoritmo utiliza una asociación punto a punto para obtener una primera alineación aproximada de los submapas y luego, utiliza una asociación punto a plano para refinar el alineamiento. Además, la complejidad de la asociación de puntos del pICP se reduce de $O(n^2)$ a $O(n)$ utilizando una heurística basada en la representación probabilística de los puntos. Los resultados del pICP se usan como observaciones relativas entre las distintas posiciones del EKF. Este algoritmo de SLAM se ha probado en distintos experimentos usando un sonar multihaz montado mirando hacia abajo produciendo mapas dos-y-medio-dimensionales (2.5D) así como montado en un actuador rotativo de dos ejes moviéndolo de mirando hacia abajo a mirando en frente para producir mapas 3D.

La segunda parte de la tesi presenta un escáner láser submarino 3D para incrementar, respeto al sensor acústico multihaz, la resolución, la precisión y la frecuencia de la percepción 3D. El escáner láser submarino está formado por una cámara y un proyector de línea láser que escanea un área de interés utilizando un espejo actuado por un galvanómetro, ambos sellados por una ventana plana. El uso de este tipo de ventanas produce una deformación en la luz láser proyectada. Esta deformación se estudia creando un modelo del sensor basado en rayos. En esta tesis proponemos utilizar un cono elíptico para representar la superfície por la cual la luz se propaga debajo el agua. El cono elíptico representa mejor el haz de luz submarino que un plano (la superfície típicamente utilizada

en otros escáneres láser submarinos) porque representa los distintos grados de curvatura de la luz proyectada, incluso una línea recta. También proponemos un método de calibrar para estimar los parámetros del modelo basado en rayos así como los conos elípticos para los distintos ángulos de incidencia entre la ventana y el láser. Los resultados experimentales muestran como el escáner láser tiene una precisión sub milimétrica y que el uso del cono elíptico no solo produce una mejor representación que un plano, sino que también mejora el tiempo de cálculo comparado con el modelo de rayos sin perder precisión.

Finalmente, esta tesis presenta dos aplicaciones prácticas de uso del escáner láser submarino. Primero, el sensor se usa en un EKF SLAM de posición donde cada posición del robot correspondiente a cada escaneo se corrige mediante un registro basto de nube de puntos basado en características que se refinan mediante un registro de punto más próximo iterativo (ICP). El algoritmo de EKF SLAM es testeado en la inspección de una estructura de tuberías y válvulas con el robot Girona 500 AUV y el escáner láser en un tanque de agua. En segundo lugar, el escáner se utiliza conjuntamente con dos sistemas de manipulación distintos. El primer experimento de manipulación utiliza un manipulador de 8 grados de libertad (DoF) que tiene como misión moverse de manera cíclica entre tres posiciones sin chocar con el entorno, a priori desconocido. En este experimento, el escáner láser se utiliza para actualizar el mapa que el algoritmo planificador de trayectorias usa para calcular trayectorias seguras. El segundo experimento de manipulación utiliza un manipulador de 4 DoF montado en el Girona 500 AUV par agarrar una ánfora del fondo de un tanque de agua. En este experimento el escáner láser se utiliza para detectar la ánfora y calcular la posición de aproximación y agarre del objeto.

1

Introduction

In this chapter we present the main problems that motivated this Ph.D. thesis: to develop new techniques for underwater 3D perception to improve real world underwater applications. The motivations as well as the relationship with real-world applications and the constrains of the state of the art are introduced in Section 1.1. Next, we state the objectives of this thesis in Section 1.2 and we describe briefly the context in which this work has been done in Section 1.3. Finally the organization of the thesis is presented in Section 1.4.

1.1 Motivation

Ocean exploration has increased significantly during the last decades in different fields. This is not particularly surprising since 71% of the Earth surface are oceans and only 5% of them can be considered explored [22]. On one hand, the science community is constantly exploring in fields such as oceanography [23], marine geology [24], underwater archaeology [25, 26], environmental monitoring [27] and damage assesment [28]. On the other hand, cable laying, oil and gas drilling, offshore wind farms and, in general, offshore industries are increasing their operations in the oceans with a big increase of the Inspection, Maintenance and Repair (IMR) applications [29, 30]. Early underwater exploration begun using manned submersibles, which is a technology still in use. However, the use of Remote Operated Vehicles (ROVs) increases the safety of the operation as well as the bottom time because the crew of vehicle can be changed without the need of the ROV returning to the surface. This, also decreases the cost of operation and exploration when compared to manned submersibles. ROVs are used every day in ocean exploration and offshore operations, however, they require a support vessel which makes the operation expensive. This has pushed the technology forward and the use of Autonomous Underwater Vehicles (AUVs) is being normalized every day.

AUVs provide a stand-alone platform detached from any support infrastructure that can perform missions without a direct human intervention or supervision [31]. In order to get really autonomous AUVs, several key enabling technologies both software and hardware need to be further developed. From a hardware point of view research has focused on technologies such as batteries [32], acoustic modems [33, 34] or optical modems [35, 36]. On the software engineering side some of the most active technology development fields are autonomous localization [37, 38], mapping and three-dimensional (3D) perception [39], autonomous path planning and re-planning [40, 41] or autonomous intervention [42].

The 3D perception and mapping problem are very closely related to the robot localization. If the robot is poorly localized, the map resulting of accumulating all the 3D information that the robot gathered would not be consistent and therefore, poorly informative. Obtaining more informative maps (i.e. more accurate 3D perception and mapping) opens the capabilities of the AUVs in the fields where interaction with the environment is necessary such as path planning and manipulation.

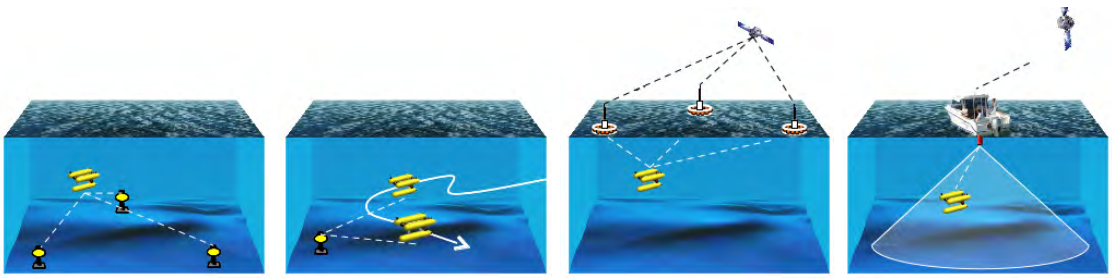

(a) LBL **(b)** Single beacon **(c)** Inverted LBL **(d)** USBL

Figure 1.1: Different types of acoustic absolute positioning fixes.

Underwater navigation is based on Dead Reckoning (DR) integrating Doppler Velocity Log (DVL), pressure and Attitude and Heading Reference System (AHRS) sensors. Using this navigation approach, the vehicle estimate of its position suffers from an unbounded error drift regardless of the use of high end Inertial Navigation System (INS) [43]. Using

measurements from a Global Positioning System (GPS) receiver is a widely used solution to bound such error. However, electromagnetic waves do not propagate efficiently through the water, making the GPS solution not available when the vehicle is submerged. In this case, Long Baseline (LBL) systems (see Fig. 1.1a) can be used for the same purpose although the calibration of the acoustic network is required prior to the operation [44]. The calibration step can be reduced or eliminated by using single beacon methods [45, 46] (see Fig. 1.1b), inverted LBL or GPS Intelligent Buoys (GIB) [47, 48] (see Fig. 1.1c) or Ultra-Short Baseline (USBL) [49] (see Fig. 1.1d) systems. However, these methods confine the operational region to the area of coverage of the sensor network. Terrain-Based Navigation (TBN) methods can remove this restriction when an a priori terrain map of the area is available [18, 50, 51]. However, for a robot to be truly autonomous, it should localize itself with the on-board sensors and without any external infrastructure. If the vehicle can build and localize itself within a map while it is preforming its missions, this restrictions would be avoid. This is fully summarized in the concept of Simultaneous Localization and Mapping (SLAM).

Multiple underwater SLAM algorithms using either optical or sonar sensors are present in the literature. On one hand, optical sensors provide high resolution and refresh rate at a relatively low cost although they cannot operate in turbid waters. On the other hand, sonar sensors can work in environments with turbid water because of the low attenuation of sound in water. However, their cost is substantially higher when compared to optical sensors and their resolution and refresh rate is lower.

(a) 2D photomosaic of a 17th century shipwreck [12].

(b) 3D reconstruction of the lower right corner of Fig. 1.2a [12].

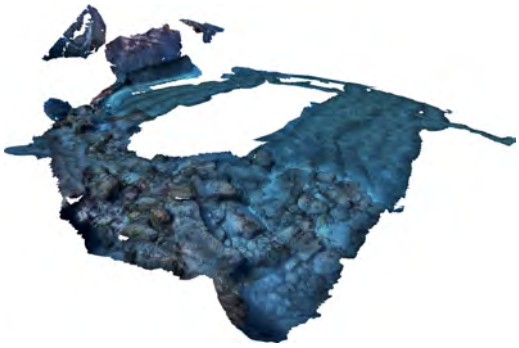

(c) 3D reconstruction of a natural environment using a multi-vehicle approach [52].

Figure 1.2: Different underwater image processed products.

The underwater computer vision community has presented several works using passive lighting (i.e. ambient light or lamps and spotlights illuminating the whole scene). Two-dimensional (2D) photomosaicking has been studied and several solutions have been presented [25, 53] with later works incorporating multiple vehicles [21] as well as implementations developed having the end-used application in mind [54] or studying long term evolution of underwater areas of interest [55] (see Fig. 1.2a). However, the assumption of a planar world is wrong due to the parallax effect, which is more notorious in areas with high relief. To solve this problem, the research community has also worked in 3D reconstructions using monocular [56, 57] and stereo cameras [52, 58, 59, 60] in different SLAM and Structure from Motion (SfM) approaches (see Figs. 1.2b and 1.2c). All these techniques are strongly dependent in the texture in the image to extract key points and describe them using feature descriptors to match them across several images.

The underwater community has also proposed SLAM algorithms using sonar. Similarly to 2D photomosaicking, [61] presented a feature-based registration method to register Forward-Looking Sonar (FLS) imagery while [62] developed a Fourier-based method to build large-scale mosaics (see Fig. 1.3a). Moreover, several feature based methods have been developed using sonar profilers for 2D SLAM [63, 64, 65, 66]. However, features can not be extracted in a robust way in natural environments. For this reason, the research evolved to featureless methods [67, 68] (see Figs. 1.3b and 1.3c). In the same way but using multibeam echosounders, two-and-a-half-dimensional (2.5D) or bathymetric SLAM has also focused in featureless approaches [69, 70, 71] or even spectral registration of 3D sonar data [72]. In contrast, [73] presented a 3D evidence grids SLAM tested in an underwater tunnel in Mexico using multiple pencil-beam echosounders to perceive the 3D information around the underwater vehicle. However, as far as the authors knowledge, the state of the art was not presenting any full 3D underwater SLAM solution using a multibeam echosounder.

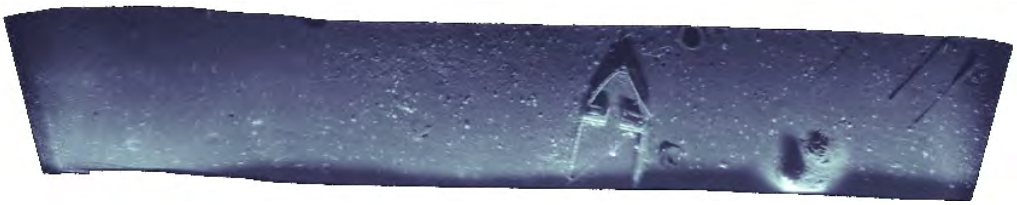

(a) 2D FLS mosaic using [62].

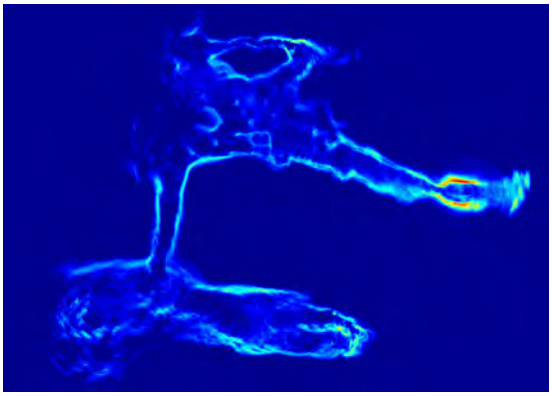

(b) 2D acoustic map [67].

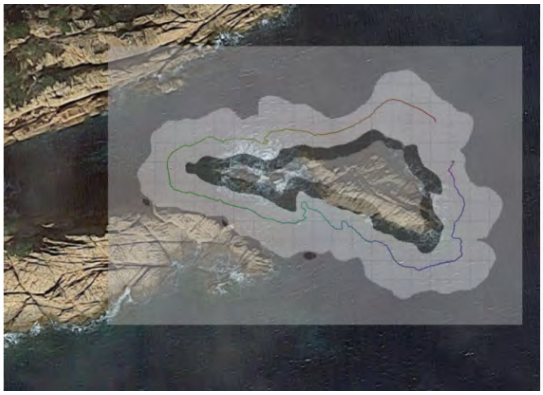

(c) 2D occupancy map [68] where gray is free space.

Figure 1.3: Different underwater sonar 2D SLAM results.

The first contribution of this thesis presents the extension of [2] to a full 3D underwater SLAM using a multibeam echosounder [1]. In this work, we extended to 3D the probabilistic registration algorithm [74] previously used in man-made environments [75] as well as natural environments [67]. This work presents results using a normal down-looking multibeam echosounder configuration (2.5D) of an area of geological interest as well as a dataset gathered in a harbor where the sonar was mounted on a pan and tilt unit scanning both the seabed and the harbor pier walls (3D).

Although this is a good approach to produce 3D maps, the acquisition time of a 3D scan steering a multibeam using a pan and tilt unit is slow. In contrast in-air 3D perception sensors, specially depth cameras and stereo imaging systems, provide video frame rate 3D point clouds. We have already discussed that stereo imaging is strongly dependent in features. However, depth cameras use different technology based in projecting its own structured light to retrieve the 3D information. Most of the commercially available depth cameras work with infrared (IR) light and, although the distortion introduced by the sealing housing can be compensated, IR is propagated only some tens of centimetres into the water [76, 77]. Improving the underwater 3D perception and putting it closer to the performance of in-air technology is key, specially if we are interested in automating IMR operations, whose demand is increasing.

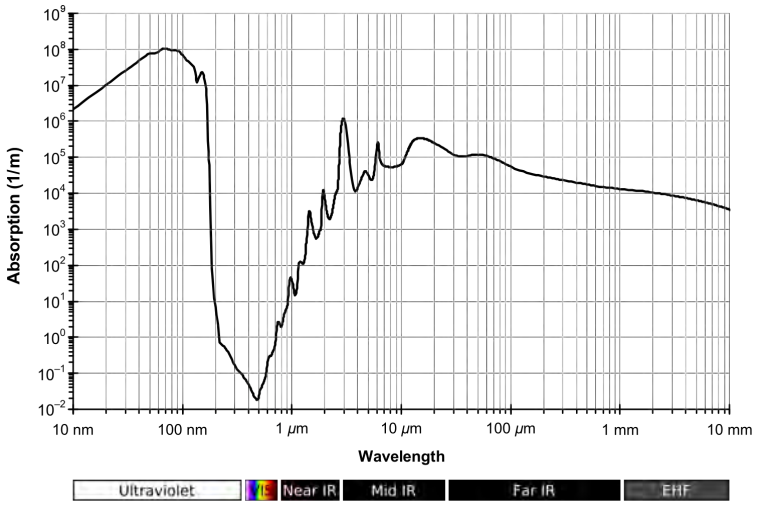

Figure 1.4: Water absorption spectrum for a wide variety of wavelengths [78].

In contrast to IR, visible light is less attenuated underwater (see Fig. 1.4). Several authors have presented works using different types of visible light to produce 3D reconstructions. Although [79] presents sub-millimetric accuracy in the 3D reconstruction results using binary patterns, the reconstruction time of each frame does not allow the system to work on-line. Moreover, the non-coherent light used in [79] does not propagate as good as laser light which is highly collimated and has a higher optical density. Using laser, [80] presents a work where a laser line is projected static with respect to the vehicle, producing profiles similar to those of the multibem echosounder having the same full scan acquisition time restriction (i.e. the laser camera system has to be moved to gather scans). In [81], the authors also prsent a fixed camera-laser system,in this case, recovering the RGB information of a laser point using a secondary camera. Moreover, [71, 82] include this two fixed camera-laser system into SLAM frameworks. In a similar way, [83] scans the laser

line by mounting it on a robotic arm but the scan time does not allow for on-line full scan gathering. An even more evolved system was presented in [84], where the same varying laser soure problem as in [83] is solved by projecting two perpendicular laser planes and a self calibrating method used at each individual shot. Using a laser source and a diffractive optical element, [85] projects a multiple line pattern used to produce one-shot 3D reconstructions. Although this set up allows for on-line scan gathering as it takes only one image to compute the reconstruction, the 25 projected lines produce a 3D reconstruction with higher density of points along the laser lines and lower density across these. Other works present non-fixed camera-laser systems where the laser line is scanned across the image using an actuator. This produces a much faster scan than when steering the overall laser-camera system underwater because the inertia and friction of steering the laser emitter [86, 87] or a mirror [88, 89, 90] is much lower. Moreover, this can increase the density of points across the different projected laser lines as the step of the actuator can be changed according to several parameters such as distance to target.

In all these systems where light is projected through a viewport towards an scene, and the projected pattern is used to retrieve the 3D information of the observed surface, it is very important to know how the structured light is distorted because of the refraction. Neglecting the effects of the refraction will produce errors in the triangulation of the 3D points. This effect can be minimized when using dome-shaped viewports [91]. However, building dome-shaped viewports is more complex than flat viewports and, if the center of the dome is not perfectly aligned with the focal point of the light, some distortion produced by the refraction is still be present.

The second contribution of this thesis studies the refraction of the projected light and how the lines are deformed when passing through the flat viewport used to seal the laser projectors [7]. In this work we proposed to use an elliptical cone to represent the surface that the laser light travels on in the underwater medium. The intersection of an elliptical cone with a plane, in other words how the light would be projected onto a plane, can be a straight line or a curve depending on the cone's parameters. That, describes accurately the different projected shapes of the laser due to a wide variety of incidence angles between the light and the viewport.

As far as the authors know, the prior literature that about non-fixed camera-laser systems with flat viewports did not take into account the curvature of the deformation. Previous authors [88, 90] assumed that the refraction only affects the plane equation. This assumption only holds when the laser and the flat viewport are perpendicular. The third contribution of this thesis presents a new real-time underwater non-fixed camera-laser scanner and the full ray-based model and calibration procedure for the system with flat viewport [4]. The presented ray-based model and calibration do take into account the full 3D refraction of the projected light. Moreover, we also compute the elliptical cones detailed in [7] from the calibrated system. Therefore, they can be used for real time triangulation of the points, drastically reducing the speed of the 3D points computation when compared to the ray-based model.

As we have previously explained, ocean operations have increased significantly in the past years. We believe that, this newly developed sensor is a key enabling technology, specially for IMR applications. In this way, the fourth and fifth contributions of this thesis correspond to underwater applications requiring the use of this sensor.

The fourth contribution presents a pose-based SLAM, similar to the first contribution [1], but using the designed underwater laser scanner [5]. In this work we use state of

the art techniques to register point clouds gathered with the underwater laser scanner mounted on an AUV. The registration is used in a pose-based Extended Kalman Filter (EKF) SLAM to correct the robot drift while mapping an underwater structure including pipes and valves.

The fifth and last contribution of this thesis describes the use of our laser scanner together with two different manipulation platforms [6]. In this work, the underwater laser scanner is used to provide real-time 3D point clouds of the environment where the manipulator platform is moving. The work presents two different experiments. The first one uses an 8 degrees of freedom (DoF) fixed-base manipulator to move around a cluttered environment without colliding with any of the present objects. The second one uses an 8 DoF Underwater Vehicle-Manipulator System (UVMS) to autonomously grasp an object located at the bottom of a water tank.

1.2 Objectives

With the motivations of this thesis described, we can now state our main goal as:

> *To research and develop methods and techniques for 3D underwater SLAM using sonar and laser profiling sensors, applying them to navigation, mapping and intervention.*

This generalistic purpose goal can be divided into different small goals:

O.1 Underwater 3D SLAM using a multibeam echosounder: Develop a SLAM framework to correct the navigation drift of underwater vehicles as well as to estimate a consistent 3D map using a multibeam echosounder capable of scanning in 3D. This involves 3 sub-objectives:

- **O.1.1 Probabilistic registration:** Extend to 3D the probabilistic registration previously used in some of the works in our research group [67, 74, 92]
- **O.1.2 SLAM framework:** Propose a SLAM framework that can use the results of the registration algorithm to improve the robot localization as well as the produced map.
- **O.1.3 Experimental validation:** Demonstrate the capabilities of the proposed method through experimental validation.

O.2 Underwater laser scanner: To design, develop and test a real-time 3D laser scanner. To achieve real-time, a laser plane will be steered with a high-speed galvanometer, avoiding the movement of high inertia masses. The scene will be grabbed with a camera able to segment and provide the enlighten pixels at high-speed. This objective involves the following sub-goals:

- **O.2.1 Variable Speed/Resolution:** The scanner will be adaptable to different applications with different speed/resolution requirements. It will be able to provide point clouds at high-speed but low-resolution or at slow-speed but high-resolution.
- **O.2.2 Ray distortion model:** A model of the propagation of the laser plane across the different media, air-viewport-water, will be studied. The method is intended

to explain the non linear distortion suffered by a laser plane when traversing a flat viewport at different incidence angles.

O.2.3 Sensor Model and Calibration: Develop a calibration procedure for the 3D laser scanner able of taking into account the ray distortion model in order to improve the system accuracy.

O.3 Underwater laser scanner applications: Test the real-time 3D laser scanner in different underwater IMR applications:

O.3.1 Structure Inspection: Use the developed laser scanner for mapping and inspection applications. Integrate the sensor in a pose-based SLAM where the registrations between point clouds gathered at different times by the laser scanner are used to correct the robot navigation drift.

O.3.2 Intervention: Demonstrate the capabilities of the system as a 3D sensor to be used for subsea manipulation.

1.3 Context

The work presented in this thesis has been supported by the Spanish Ministry of Science, Innovation and University with the FPI 2012 grant BES-2012-053857 and the projects DPI2011-27977-C03-02 (COMAROB) and DPI2014-57746-C3-3-R (ARCHROV) as well as the European Commission funded project H2020-TWINN-2015 (CSA)-692427 (STRONGMAR). The thesis has been conducted at the Underwater Robotics Research Center, Centre d'Investigació en Robòtica Submarina (CIRS), of the Computer Vision and Robotics (VICOROB) Institute of the Universitat de Girona (UdG). The research of this group started in 1992 and have received funding support for national and European research projects. During the last 19 years, the team has developed several AUVs prototypes:

- GARBI [93] was the first underwater vehicle designed at the UdG and it was initially conceived as an ROV and later redesigned as an AUV.
- URIS [94] was a very light AUV.
- Ictineu [95] won the first Student Autonomous Underwater Challenge - Europe (SAUC-E) competition in 2006 [96].
- Sparus was the first torpedo shaped AUV and also won SAUC-E in 2010 [96].
- Girona 500 [97] was designed as a very felxible AUV with mapping and intervention capabilities. The vehicle is currently operational and has been used during this thesis. Recently, it was licensed to Iqua Robotics S.L. being now available as a commercial platform [98].
- Sparus II [99, 100] is an evolution of Sparus. It won the Eurathlon competition in 2014 and 2015 [101] as well as the European Robotics League (ERL) Emergency Robots in 2017 [102]. It is currently operational and it has also been licensed to Iqua Robogics S.L.which made it commercially available [98].

However, the research done at CIRS is not only focused in the development of AUVs. Instead, it is mainly focused in providing the developed vehicles with new capabilities. These includes path planning [103, 104, 105, 106], autonomous intervention [107, 108, 109, 110] and SLAM using acoustic [62, 66, 67, 68, 111]. Moreover, the research also includes computer vision applied in the underwater domain and covers fields such as 3D reconstruction [57], underwater panoramic imaging [112, 113], image dehazing [114] multi-vehicle mapping [52] and fish detection [115]. The joint work between CIRS and Underwater Vision Lab (UVL) resulted in applications such as dam inspection [29], AUV mapping of archeological sites [12] and AUV mapping and intervention in a harbour [116].

1.3.1 Participation in Research Projects

This thesis has contributed to the following projects in which CIRS has participated:

- EU H2020 Project STRONGMAR: STRengthening MARritime technology Research Center (ref. H2020-TWINN-2015 (CSA)-692427), funded by the European Commission.
- MINECO Project ARCHROV (part of MERBOTS): marine ARChaeology through HROV/AUV cooperation (ref. DPI2014-57746-C3-3-R), funded by the Spanish Ministry of Science and Innovation.
- MINECO Project COMAROB (part of TRITON): Robótica cooperativa Marina para el mapeo acústico y la intervención (ref. DPI2011-27977-C03-02), funded by the Spanish Ministry of Science and Innovation.
- EU FP7 Project MORPH: Marine robotic system of self-organizing, logically linked physical nodes (ref. FP7-ICT-2011-7-288704), funded by the European Commission.
- EU FP7 Project TRIDENT: Marine Robots and Dexterous Manipulation for Enabling Autonomous Underwater Multipurpose Intervention Missions (ref. ICT-248497), funded by the European Commission.

Finally, this thesis has also benefited from two research stay. The first stay was done at the University of Rhode Island (U.S.) under the supervision of Dr. Chris Roman, assistant professor at the Department of Oceanography. Dr Roman's research focus on system and method development for acoustic and photographic seafloor mapping [69, 117, 118]. The second stay was at the Ocean Systems Laboratory (OSL) of Heriot-Watt University (UK). OSL is a science and engineering research centre focusing in autonomous systems and underwater acoustic sensors theory and processing [119, 120, 121].

1.4 Document Structure

From the point of view of the sensor used to perceive the environment, this thesis has two distinguished parts. The first part focuses on the use of a multibeam echosounder to perform underwater 3D SLAM and is presented in Chapter 2. The second one uses a newly developed underwater laser scanner being presented in Chapters 3 to 6. As the multibeam, the laser scanner is also a range sensor providing point clouds. Nevertheless, it increases significantly the accuracy of the 3D measurements, the frame rate as well as the

density of the point clouds. Then, the refraction of light is studied to propose a model as well as a calibration procedure for the laser scanner. Finally, we use the developed scanner in two different contexts. First, we present a method for 3D SLAM with application to mapping and inspection. Next, the scanner is used for subsea manipulation. This thesis is structured as follows:

- **Chapter 2: Multibeam 3D Underwater SLAM with Probabilistic Registration** presents an underwater pose-based EKF SLAM using a multibeam echosounder to produce consistent 3D maps of underwater environments.
- **Chapter 3: Underwater 3D Laser Scanners: The Deformation of the Plane** studies the feasibility of using an elliptical cone surface to represent a laser line that has been distorted when passing through a flat viewport before going into the water.
- **Chapter 4: Underwater Laser Scanner: Ray-based Model and Calibration** presents a new underwater laser scanner sensor and its ray-based model and calibration.
- **Chapter 5: Inspection of an Underwater Structure using Point Cloud SLAM with an AUV and a Laser Scanner** presents a pose-based EKF SLAM that uses the point cloud data from the underwater laser scanner developed in the context of this thesis.
- **Chapter 6: 3D Laser Scanner for Underwater Manipulation** presents two real applications to manipulation of the underwater laser scanner developed in the context of this thesis.
- **Chapter 7: Results and Discussion** summarizes the results obtained in this thesis as well as provides an overall discussion of the presented work.
- **Chapter 8: Conclusions and Future Work** summarizes the conclusions based on the contributions of this thesis and proposes futures work in the thesis fields.
- **Appendix A: Line-Cone Intersection** presents the mathematical manipulations to solve the system of equations in Eq. (14) from Chapter 4.

2

Multibeam 3D Underwater SLAM with Probabilistic Registration

In this chapter, we propose a full 3D underwater SLAM using a multibeam echosounder mounted on an AUV. The method divides the mission of the vehicle into submaps and registers them when overlapping conditions are met. The algorithm stores each submap pose in an pose-based EKF SLAM and uses the result of the registration process as an update between them. The algorithm is tested using two different set ups, one with the normal down-looking multibeam configuration and one with the multibeam mounted on a pan and tilt actuator. The proposed work is described in detail and published in the following journal paper with extended results available in Section 7.1:

Title: Multibeam 3D Underwater SLAM with Probabilistic Registration
Authors: **Albert Palomer**, Pere Ridao, and David Ribas
Journal: Sensors
Volume: 16, Number: 4, Published: 2016
DOI: 10.3390/s16040560
Quality index: JCR2016 Instruments & Instrumentation, Impact Factor: 2.677, Q1

sensors

MDPI

Article

Multibeam 3D Underwater SLAM with Probabilistic Registration

Albert Palomer *, Pere Ridao and David Ribas

Vicorob Research Institute, Universitat de Girona, c/Pic de Peguera 13-Parc Científic i Tecnològic de la UdG-CIRS Building, Girona l17003, Spain; pere@eia.udg.edu (P.R.); dribas@udg.edu (D.R.)
* Correspondence: apalomer@eia.udg.edu; Tel.: +34-972-419-651

Academic Editor: Jaime Lloret Mauri
Received: 15 January 2016; Accepted: 14 April 2016; Published: 20 April 2016

Abstract: This paper describes a pose-based underwater 3D Simultaneous Localization and Mapping (SLAM) using a multibeam echosounder to produce high consistency underwater maps. The proposed algorithm compounds swath profiles of the seafloor with dead reckoning localization to build surface patches (*i.e.*, point clouds). An Iterative Closest Point (ICP) with a probabilistic implementation is then used to register the point clouds, taking into account their uncertainties. The registration process is divided in two steps: (1) point-to-point association for coarse registration and (2) point-to-plane association for fine registration. The point clouds of the surfaces to be registered are sub-sampled in order to decrease both the computation time and also the potential of falling into local minima during the registration. In addition, a heuristic is used to decrease the complexity of the association step of the ICP from $O(n^2)$ to $O(n)$. The performance of the SLAM framework is tested using two real world datasets: First, a 2.5D bathymetric dataset obtained with the usual down-looking multibeam sonar configuration, and second, a full 3D underwater dataset acquired with a multibeam sonar mounted on a pan and tilt unit.

Keywords: AUV; multibeam; SLAM; 3D; bathymetry

1. Introduction

For Autonomous Underwater Vehicles (AUVs), addressing the navigation and mapping problems is crucial to achieve a fully operational status. Dead reckoning navigation systems suffer from an unbounded drift error, regardless of using high-end Internal Navigation Systems (INS) [1]. To avoid this, such systems are commonly aided with absolute positioning fixes. Using the measurements from a Global Positioning System (GPS) receiver is a typical solution during operations taking place on the surface. When the vehicle is submerged, Long Base Line (LBL) systems [2] can be used for the same purpose, although complex calibration of the acoustic beacon network is required prior to its operation. Using single beacon/transponder methods may reduce the calibration burden [3,4] or even eliminate it, at the cost of a reduced accuracy, when inverted LBL [5] or Ultra Short Base Line (USBL) [6] systems are used instead.

All those methods share the limitation of confining the robot operation to the area of coverage of the system. Terrain-based navigation (TBN) methods [7] can mitigate this limitation when an *a priori* Digital Terrain Map (DTM) is available on the target area. However, for an underwater vehicle to become truly autonomous, it should be able to localize itself using only on-board sensors and without the help of any external infrastructure. The Simultaneous Localization And Mapping (SLAM) concept aims to achieve that. Although more than 20 years of research have provided different approaches to solve the SLAM problem, mostly in land mobile robotics [8], there are still few solutions for underwater use, mainly due to the sensing limitations imposed by the medium and the complexity of the environment.

Underwater SLAM can be divided in two main categories: sonar and vision based SLAM. Although vision sensors may suffer from poor visibility in turbid waters, they provide fast refresh rates and high-resolution data at a fraction of the cost of a sonar sensor. Several noteworthy examples of underwater visual SLAM have been presented during recent years [9–12]. On the other hand, sonar sensors can work in bad visibility conditions, penetrating further (10–150 m) because of the low attenuation of sound in water. However, the refresh rate and resolution are medium to low and are generally expensive. Although the number of underwater SLAM examples using sonar is still reduced, they are promising.

Regarding imaging sonar mosaicking, [13] presented a feature-based registration method for two-dimensional forward-looking sonar images, while [14] developed a Fourier-based registration method to build large-scale mosaics. Moreover, several feature-based methods have been reported using: (1) point features extracted from mechanically/electronically scanned imaging sonars [15–17] or using a synthetic aperture imaging sonar [18]; and (2) line features extracted from a Mechanical Scanning Imaging Sonar (MSIS) in a man-made environment [19]. However, it is extremely difficult to extract features robustly in a natural underwater environment. Therefore, some researchers have focused on using featureless methods such as scan matching or occupancy grids. The work presented in [20] proposed a SLAM algorithm using a Particle Filter (PF) and range measurements from multiple pencil-beam sonars to generate an occupancy grid of a sinkhole. The method was time and computationally efficient because of the use of an octree structure to represent the environment. Although bathymetric (elevation 2.5D) maps are commonly used in the context of TBN, there have been few studies reporting successful SLAM implementations using bathymetric maps generated with data from a multibeam profiler. The pioneering work in [21] used cross correlation and Iterative Closest Point (ICP) for coarse and fine registration of bathymetric surfaces. More recently, [22] presented the bathymetric distributed particle SLAM (BPSLAM), an algorithm based on the distributed particle SLAM (DPSLAM) [23], which used a PF similar to the one proposed in [20] but representing the environment as a bathymetric map distributed across the ancestry of a given particle. It is worth mentioning that those methods were specifically designed for 2.5D elevation data, and, therefore, they are not suited for full 3D underwater environments.

This paper presents the extension to 3D of the work previously presented in [24]. The registration algorithm is a 3D-capable evolution of the 2D MSIS probabilistic Iterative Correspondence (MSISpIC) algorithm [25], which has been already applied to 2D SLAM in underwater man-made [26,27] and natural [28] environments. Our method is similar to the previous work of [21] but takes advantage of recent results obtained using the probabilistic ICP algorithms mentioned above, which are better suited to dealing with the uncertainty inherent in sonar data. Moreover, our method is not restricted to using solely 2.5D bathymetric data, and, hence, new results obtained with full 3D data are also reported here.

The 3D underwater SLAM framework presented here corrects the robot trajectory in order to produce high consistency underwater maps. The algorithm, like other state of the art SLAM techniques [21], divides the mission into a set of submaps, or surface patches, created by combining multibeam data and an estimate of the navigation until certain criteria are fulfilled. Every time a submap is created, possible overlaps with other existing patches are checked to look for loop closures. If any are found, the registration process takes place between the patches in order to refine the robot navigation. One of the novelties of the proposed method is the implementation of a two-step Probabilistic ICP (pICP) with point-to-point and point-to-plane for rough and fine registration, respectively. The improved registration method also incorporates a point cloud subsampling strategy to decrease the number of involved points as well as a novel method to decrease the complexity in the association step of the pICP from $O(n^2)$ to $O(n)$.

The rest of the paper is organized as follows. First, Section 2 focuses on the submap creation. In Section 3, the registration algorithm is explained, followed by the SLAM algorithm in Section 4.

Sensors **2016**, *16*, 560

Section 5 presents the experiments and results, and, finally, Section 6 presents the conclusions and future work.

2. Submap Creation

For bathymetric mapping, multibeam sonars are generally fixed to the vehicle so that the 2D swath profiles are generated perpendicular to the surge direction. In that way, 2.5D surfaces are built by composing the multibeam data with the displacement of the vehicle. Alternatively, more complex environments can be inspected by sweeping a multibeam sonar mounted on a pan and tilt unit, so it is the rotation of the sonar head, and not solely the vehicle motion, that leads to the coverage of the surfaces. The point clouds resulting from the collection of multibeam data (Figure 1), along with other information such as boundaries or position with respect to the world, are what we refer to in this work as patches or submaps. This section describes the process of building these submaps during a mission.

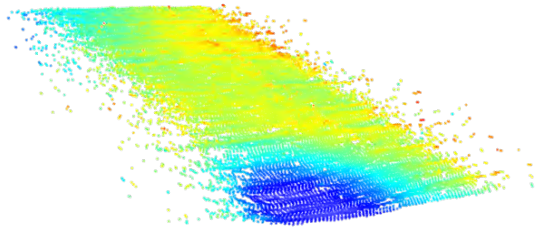

(**a**) Fixed multibeam

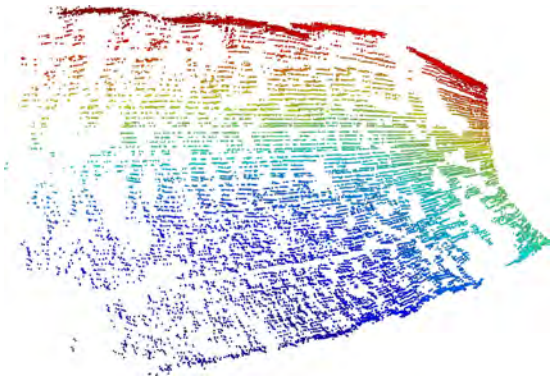

(**b**) Sweeping multibeam

Figure 1. Two different submaps colored according to depth. In (**a**), the multibeam was mounted in a fixed downward-looking configuration, typically from bathymetric mapping; In (**b**), the sonar head was mounted on a pan and tilt unit and swept vertically to cover a portion of steep terrain.

2.1. Dead Reckoning

To be able to construct the submaps, regardless of whether the sonar is being swept or mounted on a fixed position, it is necessary to estimate the AUV position at the time each multibeam reading was acquired. As will be later detailed in Section 2.2, our procedure uses the relative displacements made by the vehicle between consecutive multibeam swaths to compound the point clouds. Moreover, given the probabilistic nature of the proposed registration algorithm, it is also necessary to estimate how the uncertainty evolves during these motions. To obtain this information, an Extended Kalman Filter (EKF) is used.

The state vector of the filter (see Equations (1) and (2)) contains 12 elements representing the current six Degrees of Freedom (DoF) vehicle position and velocity, as well as two more elements

corresponding with the stored x and y position of the vehicle at the time when the last multibeam reading was obtained (x_{mb}, y_{mb}):

$$\hat{\boldsymbol{x}}_k = \begin{bmatrix} x & y & z & \phi & \theta & \psi & u & v & w & p & q & r & x_{mb} & y_{mb} \end{bmatrix}_k^T \tag{1}$$

$$\boldsymbol{P}_{\boldsymbol{x}_k} = E\left(\left[\boldsymbol{x}_k - \hat{\boldsymbol{x}}_k \right] \left[\boldsymbol{x}_k - \hat{\boldsymbol{x}}_k \right]^T \right)^T \tag{2}$$

A constant velocity kinematic model is used for prediction of the vehicle states, while those regarding the stored previous vehicle position are assumed static. In the correction stage, updates are performed asynchronously with the measurements coming from an Attitude and Heading Reference System (AHRS), a Doppler Velocity Log (DVL), and a pressure sensor. The filter iterates normally until a new multibeam reading is received. When this occurs, one last prediction is made to get an updated estimation of the vehicle's position before calculating $\boldsymbol{o}_k = N(\hat{\boldsymbol{o}}_k, \boldsymbol{P}_{\boldsymbol{o}_k})$, a new vector containing the displacement executed by the vehicle in the horizontal plane during the period of time between the current and the previous multibeam readings, as well as the z position and orientation of the vehicle at the current time:

$$\hat{\boldsymbol{o}}_k = \begin{bmatrix} x - x_{mb}, & y - y_{mb}, & z, & \phi, & \theta, & \psi \end{bmatrix}_k^T \tag{3}$$

$$\boldsymbol{P}_{\boldsymbol{o}_k} = \boldsymbol{J}_o \boldsymbol{P}_{\boldsymbol{x}_k} \boldsymbol{J}_o^T; \;\; \boldsymbol{J}_o = \begin{bmatrix} \boldsymbol{I}_{2\times 2} & \boldsymbol{0}_{2\times 4} & \boldsymbol{0}_{2\times 6} & -\boldsymbol{I}_{2\times 2} \\ \boldsymbol{0}_{4\times 2} & \boldsymbol{I}_{4\times 4} & \boldsymbol{0}_{4\times 6} & \boldsymbol{0}_{4\times 2} \end{bmatrix} \tag{4}$$

Note that the two first elements of $\boldsymbol{o}_k$ correspond to incremental values, while the other four are absolute with respect to the base reference frame used for the dead reckoning. The calculation of those increments is motivated by the cumulative drift that affects the motion in the horizontal plane. Since those states are only estimated indirectly by the velocity measurements from the DVL, the uncertainty in the xy position grows without bound. As will be introduced in the following section, working with those increments allows for a better distribution of the uncertainties within the point cloud. On the other hand, the remaining states in $\boldsymbol{o}_k$ are observed directly by other sensors (the z position is observed by the pressure sensor, and the orientation by the AHRS), and therefore their uncertainties are bounded.

Once $\boldsymbol{o}_k$ has been calculated, it is stored until the current submap is finalized. To continue with the execution of the dead reckoning filter, and to keep track of the displacements from the current position to that of the next multibeam measurement, it is necessary to replace the last two elements of the state vector (x_{mb}, y_{mb}) with the current position of the vehicle x and y:

$$\hat{\boldsymbol{x}}_k^* = \begin{bmatrix} x & y & z & \phi & \theta & \psi & u & v & w & p & q & r & x & y \end{bmatrix}_k^T \tag{5}$$

$$\boldsymbol{P}_{\boldsymbol{x}_k^*} = \boldsymbol{J}_o^* \boldsymbol{P}_{\boldsymbol{x}_k} \boldsymbol{J}_o^{*T}; \;\; \boldsymbol{J}_o^* = \begin{bmatrix} \boldsymbol{I}_{12\times 12} & \boldsymbol{0}_{12\times 2} \\ \boldsymbol{I}_{2\times 2} & \boldsymbol{0}_{2\times 12} \end{bmatrix} \tag{6}$$

Given that, the execution of the filter can continue by replicating the procedure we have just described.

2.2. Submap Forming

During the execution of the mission, the information required for the generation of the patches is stored in a temporal data structure $\boldsymbol{S}_{temp}$:

$$\boldsymbol{S}_{temp} = \begin{Bmatrix} \boldsymbol{O} & \boldsymbol{M} & \boldsymbol{R} \end{Bmatrix} \tag{7}$$

where $\boldsymbol{O} = \{\boldsymbol{o}_1, ..., \boldsymbol{o}_n | \boldsymbol{o}_i = N(\hat{\boldsymbol{o}}_i, \boldsymbol{P}_{\boldsymbol{o}_i})\}$ is the set of displacements and positions as computed in Equations (3) and (4), while $\boldsymbol{M} = \{\boldsymbol{m}_1, ..., \boldsymbol{m}_n\}$, with $\boldsymbol{m}_i = \{\delta_1, ..., \delta_m | \delta_i = N(\hat{\delta}_i, \boldsymbol{P}_{\delta_i})\}$, is the set of

Sensors **2016**, *16*, 560

all the multibeam swaths $\boldsymbol{m}$, each one containing the corresponding polar range measurements $\boldsymbol{\delta}$. Finally, $\boldsymbol{R} = \{\boldsymbol{r}_1, ..., \boldsymbol{r}_n | \boldsymbol{r}_i = N(\hat{\boldsymbol{r}}_i, \boldsymbol{P}_{\boldsymbol{r}_i})\}$ is the set of transformations required to represent the multibeam data with respect to the vehicle frame. This is particularly relevant in the case of a multibeam sonar mounted on a pan and tilt unit, since the transformations will change continuously because of the sweeping motion.

When the amount of accumulated data is deemed sufficient (see the conditions below), the current patch is closed and the contents of $\boldsymbol{S}_{temp}$ are used to generate the point cloud and other information that will be necessary later during the registration process. In addition, the position of the recently terminated patch is stored in the state vector of the pose-based EKF in charge of the SLAM process (see Section 4). Before beginning a new patch, the $\boldsymbol{S}_{temp}$ is reset to store a new batch of data.

The criteria to close a patch depend on which scenario we are dealing with. If the sonar is scanning a tri-dimensionally rich environment by means of a pan and tilt unit, each complete sweep is taken as an independent submap because, unless a very fast vehicle is used, successive scans will re-visit the same area, which only contributes to increasing the number of points without incorporating significant new information. On the other hand, the situation with typical bathymetric survey missions where the multibeam is fixed on the vehicle is substantially different. Scanned areas are generally not re-visited (not in the same transect), and the seabed is often scarce in features, which may make the successful matching of surface patches difficult. In this case, a combination of three criteria is used to determine when to close a patch:

- **Minimum size:** A minimum size is defined to avoid handling a large number of tiny patches augmenting unnecessarily the length of the SLAM state vector and reducing the overlapping.
- **Maximum size:** The maximum size is bounded to avoid handling huge patches with a high uncertainty in the surface points due to the accumulated dead reckoning error.
- **Normal occupancy:** The surface relief is analyzed to determine when the patch is rich enough to be successfully matched. The procedure basically consists in finding surface normals for each point on the cloud and representing their parametrization on a histogram. If the histogram is sufficiently occupied, the submap is closed.

Once sufficient data has been acquired and the submap is closed, all the stored data is processed to generate the point cloud and the information required for the potential registration with other submaps. In [21], the reference frame for each submap was defined as the position of the robot when the patch was started. Here, the point cloud is generated with respect to a new reference frame $\mathbb{I}$, which is placed on top of the central position of the trajectory executed during the creation of the patch, but oriented like the base frame $\mathbb{B}$ used for the dead reckoning navigation. By placing this frame in the center of the submap, the uncertainty of the points grows from the center of the patch to the edges (see Figure 2b) instead of growing from the beginning to the end (see Figure 2a). This gives a more convenient distribution of the uncertainty in the point cloud which improves the registration [29].

The process of generating the point cloud begins by selecting the central position that will be associated to $\mathbb{I}$, and that will be referenced hereafter with the mp subindex. Then, the $\boldsymbol{q}_k$ vector relating a given k position in which a multibeam reading was acquired, and the $\mathbb{I}$ reference frame can be computed from the corresponding $\boldsymbol{o}_k$ and $\boldsymbol{o}_{mp}$ (both pertaining to $\boldsymbol{O}$ and stored in $\boldsymbol{S}_{temp}$) as:

$$\hat{\boldsymbol{q}}_k = \begin{cases} \begin{bmatrix} x_{\boldsymbol{q}_{k-1}} + x_{\boldsymbol{o}_k}, & y_{\boldsymbol{q}_{k-1}} + y_{\boldsymbol{o}_k}, & z_{\boldsymbol{o}_k} - z_{\boldsymbol{o}_{mp}}, & \phi_{\boldsymbol{o}_k}, & \theta_{\boldsymbol{o}_k}, & \psi_{\boldsymbol{o}_k} \end{bmatrix}^T & k > mp \\ \begin{bmatrix} 0, & 0, & 0, & \phi_{\boldsymbol{o}_k}, & \theta_{\boldsymbol{o}_k}, & \psi_{\boldsymbol{o}_k} \end{bmatrix}^T & k = mp \\ \begin{bmatrix} x_{\boldsymbol{q}_{k+1}} - x_{\boldsymbol{o}_{k+1}}, & y_{\boldsymbol{q}_{k+1}} - y_{\boldsymbol{o}_{k+1}}, & z_{\boldsymbol{o}_k} - z_{\boldsymbol{o}_{mp}}, & \phi_{\boldsymbol{o}_k}, & \theta_{\boldsymbol{o}_k}, & \psi_{\boldsymbol{o}_k} \end{bmatrix}^T & k < mp \end{cases} \quad (8)$$

where $x_{\boldsymbol{a}}$ should be read here as the element x contained in the vector $\boldsymbol{a}$. Note that for computing $\boldsymbol{q}_k$, the vectors $\boldsymbol{q}_{k-1}$ (if $k > mp$) or $\boldsymbol{q}_{k+1}$ (if $k < mp$) also need to be known. This means that the calculation needs to be done sequentially starting by the mp position and then moving towards both ends of the submap (1 and n). The uncertainty of $\boldsymbol{q}_k$ is then computed as:

$$\boldsymbol{P}_{\boldsymbol{q}_k} = \begin{cases} \boldsymbol{J}_1 \boldsymbol{P}_{\boldsymbol{q}_{k-1}} \boldsymbol{J}_1^T + \boldsymbol{J}_2 \boldsymbol{P}_{\boldsymbol{o}_k} \boldsymbol{J}_2^T + \boldsymbol{J}_3 \boldsymbol{P}_{\boldsymbol{o}_{mp}} \boldsymbol{J}_3^T & k > mp \\ \boldsymbol{J}_4 \boldsymbol{P}_{\boldsymbol{o}_k} \boldsymbol{J}_4^T & k = mp \\ \boldsymbol{J}_1 \boldsymbol{P}_{\boldsymbol{q}_{k+1}} \boldsymbol{J}_1^T + \boldsymbol{J}_5 \boldsymbol{P}_{\boldsymbol{o}_{k+1}} \boldsymbol{J}_5^T + \boldsymbol{J}_3 \boldsymbol{P}_{\boldsymbol{o}_{mp}} \boldsymbol{J}_3^T + \boldsymbol{J}_4 P_{\boldsymbol{o}_k} \boldsymbol{J}_4^T & k < mp \end{cases} \tag{9}$$

being $\boldsymbol{J}_j$ the Jacobians of the function:

$$\boldsymbol{J}_1 = \begin{bmatrix} \boldsymbol{I}_{2\times 2} & \boldsymbol{0}_{2\times 4} \\ \boldsymbol{0}_{4\times 2} & \boldsymbol{0}_{4\times 4} \end{bmatrix} \tag{10}$$

$$\boldsymbol{J}_2 = \boldsymbol{I}_{6\times 6} \tag{11}$$

$$\boldsymbol{J}_3 = \begin{bmatrix} \boldsymbol{0}_{2\times 2} & \boldsymbol{0}_{2\times 1} & \boldsymbol{0}_{2\times 3} \\ \boldsymbol{0}_{1\times 2} & -1 & \boldsymbol{0}_{1\times 3} \\ \boldsymbol{0}_{3\times 2} & \boldsymbol{0}_{3\times 1} & \boldsymbol{0}_{3\times 3} \end{bmatrix} \tag{12}$$

$$\boldsymbol{J}_4 = \begin{bmatrix} \boldsymbol{0}_{3\times 3} & \boldsymbol{0}_{3\times 3} \\ \boldsymbol{0}_{3\times 3} & \boldsymbol{I}_{3\times 3} \end{bmatrix} \tag{13}$$

$$\boldsymbol{J}_5 = -\boldsymbol{J}_1 \tag{14}$$

It is worth noting that $\boldsymbol{q}_k$ is composed of both relative (first three elements representing a displacement) and absolute (last three elements being the orientation) measurements. Assuming that correlations in attitude estimates are negligible, computing the relative increment of the orientation would end up adding uncertainty in these 3 DoF artificially. This would apply also to the z displacement. However, we observed that if the same approach is taken in this DoF, the lever-arm effect in the registration process (the depth is referenced to the water surface) makes it much more prone to error. Therefore, we decided to reference the z position to the actual depth of the AUV regardless of the increment of uncertainty in order to make the registration process more stable.

With all the $\boldsymbol{q}_k$ computed, the point cloud can now be generated. The first step is to transform all the polar range measurements $\boldsymbol{\delta}_i = N(\hat{\boldsymbol{\delta}}_i, \boldsymbol{P}_{\boldsymbol{\delta}_i})$ which are represented in the sensor frame to that of the vehicle using the $\boldsymbol{r}_k$ transformations stored in $\boldsymbol{R}$:

$$\hat{\boldsymbol{p}}_i^{\times} = \hat{\boldsymbol{r}}_k \oplus g(\hat{\boldsymbol{\delta}}_i) \tag{15}$$

$$\boldsymbol{P}_{\boldsymbol{p}_i^{\times}} = \boldsymbol{J}_{1\oplus} \boldsymbol{P}_{\boldsymbol{r}_k} \boldsymbol{J}_{1\oplus}^T + \boldsymbol{J}_{2\oplus} (\boldsymbol{J}_g \boldsymbol{P}_{\boldsymbol{\delta}} \boldsymbol{J}_g^T) \boldsymbol{J}_{2\oplus}^T \tag{16}$$

where $g(.)$ is the polar to Cartesian conversion function, $\boldsymbol{J}_g$ is its corresponding Jacobian and $\oplus$ is the compounding operator with Jacobians $\boldsymbol{J}_{1\oplus}$ and $\boldsymbol{J}_{2\oplus}$ as defined in [30]. With the point $\boldsymbol{p}_i^{\times}$ referenced to the vehicle frame and $\boldsymbol{q}_k$ being the vehicle position referenced to $\mathbb{I}$, we can calculate the position of a point $\boldsymbol{p}_i$ as:

$$\hat{\boldsymbol{p}}_i = \hat{\boldsymbol{q}}_k \oplus \hat{\boldsymbol{p}}_i^{\times} \tag{17}$$

$$\boldsymbol{P}_{\boldsymbol{p}_i} = \boldsymbol{J}_{1\oplus} \boldsymbol{P}_{\boldsymbol{q}_k} \boldsymbol{J}_{1\oplus}^T + \boldsymbol{J}_{2\oplus} \boldsymbol{P}_{\boldsymbol{p}_i^{\times}} \boldsymbol{J}_{2\oplus}^T \tag{18}$$

After all these calculations, the information regarding the patch is saved in a new structure $\boldsymbol{S}$ as:

$$\boldsymbol{S} = \begin{bmatrix} \boldsymbol{x} & \boldsymbol{O} & \boldsymbol{W} & \boldsymbol{B} \end{bmatrix} \tag{19}$$

where $\boldsymbol{x} = N(\hat{\boldsymbol{x}}, \boldsymbol{P}_{\boldsymbol{x}})$ is the position of the frame $\mathbb{I}$ that will be used to anchor the submap in the state vector of the pose-based SLAM framework described in Section 4; $\boldsymbol{O}$ is the same set of transformations as in $\boldsymbol{S}_{temp}$; $\boldsymbol{W} = \{\boldsymbol{p}_1, ..., \boldsymbol{p}_n | \ \boldsymbol{p}_i = N(\hat{\boldsymbol{p}}_i, \boldsymbol{P}_{\boldsymbol{p}_i})\}$ is the set of points referenced to $\mathbb{I}$ that have been calculated and, finally, $\boldsymbol{B}$ is a volume containing all the points that pertain to the patch. On the horizontal plane, $\boldsymbol{B}$ is the polygon containing all the $\hat{\boldsymbol{p}}_i$ points, while, on the z direction, the boundary is defined by the minimum and maximum depth of all the points $\hat{\boldsymbol{p}}_i$ (see Figure 2).

Sensors **2016**, *16*, 560

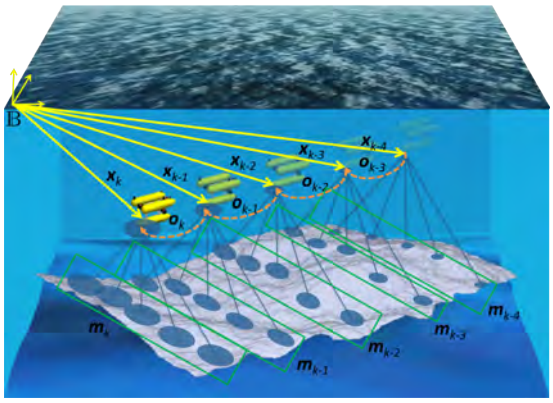

(**a**) Dead Reckoning

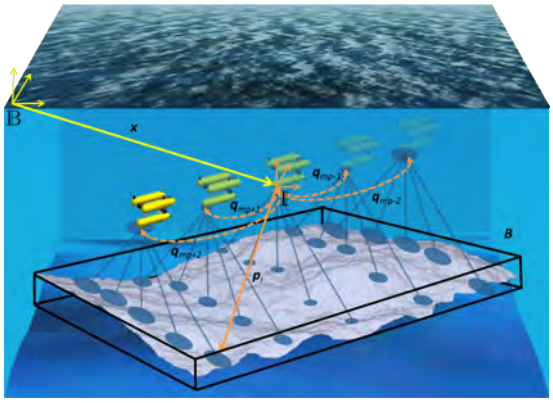

(**b**) Scan Forming

Figure 2. Example of the dead reckoning (**a**) and the scan forming (**b**).

3. Registration Algorithm

This section explains the procedure to register two submaps using probabilistic ICP. The inputs of the algorithm are a reference submap $\boldsymbol{S}_{ref}$, which has been already stored in the SLAM framework; a newly generated submap $\boldsymbol{S}_{new}$, and an initial guess of their relative displacement $\boldsymbol{q}_0 = N(\hat{\boldsymbol{q}}_0, \boldsymbol{P}_{\boldsymbol{q}_0})$ obtained from the navigation. The algorithm uses a two-stage correction procedure. First, a point-to-point correction is performed to roughly align the two submaps (until their relative displacement in two consecutive iterations falls below a threshold), and then, a point-to-plane correction is executed to refine the result. Point-to-point association tends to produce undesired effects in the presence of small misalignments (see for instance the lateral displacement depicted in Figure 3a). This is because associated points do not necessarily correspond to the exact same spot in the original surface and therefore their arbitrary occurrence may prevail over the general shape of the surface. However, point-to-point association is powerful when large displacements are present (see Figure 3b). On the other hand, point-to-plane associations tend to be driven by the shape of the surface and hence, perform better in the presence of small misalignments (see Figure 3a), but may fail when dealing with large displacements (see Figure 3b). To complement their strengths and weaknesses, we combine both methods by using an error threshold which determines when to switch from one strategy to the other.

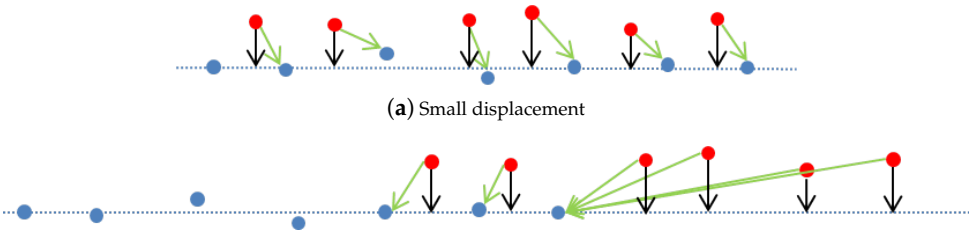

(**a**) Small displacement

(**b**) Large displacement

Figure 3. Point-to-point and point-to-plane comparison in the presence of small displacement (**a**) and large displacement (**b**). In blue, the points of the reference scan with the plane, in red, the points of the new scan. Green arrows correspond to point-to-point association while black ones represent point-to-plane.

3.1. Point-to-Point Association

Given a certain point $\boldsymbol{n}_i = N(\hat{\boldsymbol{n}}_i, \boldsymbol{P}_{\boldsymbol{n}_i})$ from the new patch $\boldsymbol{S}_{new}$, and a matching candidate $\boldsymbol{r}_j = N(\hat{\boldsymbol{r}}_j, \boldsymbol{P}_{\boldsymbol{r}_j})$ from the reference surface $\boldsymbol{S}_{ref}$, both represented in Cartesian coordinates and referenced to their respective frames ($\mathbb{I}_{new}$ and $\mathbb{I}_{ref}$), the association error $\boldsymbol{e}_{ij} = N(\hat{\boldsymbol{e}}_{ij}, \boldsymbol{P}_{\boldsymbol{e}_{ij}})$ can be defined as:

$$\hat{\boldsymbol{e}}_{ij} = \hat{\boldsymbol{r}}_j - \hat{\boldsymbol{q}}_0 \oplus \hat{\boldsymbol{n}}_i \tag{20}$$

$$\boldsymbol{P}_{ij} = \boldsymbol{P}_{\boldsymbol{r}_j} + \boldsymbol{J}_{1\oplus}\boldsymbol{P}_{\boldsymbol{q}_0}\boldsymbol{J}_{1\oplus}^T + \boldsymbol{J}_{2\oplus}\boldsymbol{P}_{\boldsymbol{n}_i}\boldsymbol{J}_{2\oplus}^T \tag{21}$$

so the point-to-point association may be solved through a simple individual compatibility test over the corresponding Mahalanobis distance:

$$d^2 = \hat{\boldsymbol{e}}_{ij}^T \boldsymbol{P}_{ij}^{-1} \hat{\boldsymbol{e}}_{ij} < \chi_{d,\alpha}^2 \tag{22}$$

All the points individually compatible with $\boldsymbol{n}_i$ form the set $\boldsymbol{A}_i$. From this set, the one with smaller Mahalanobis distance is chosen to be associated with $\boldsymbol{n}_i$.

3.2. Point-to-Plane Association

At the second stage, the metric changes and the point-to-plane distance is used instead. Now, the set of compatible points $\boldsymbol{A}_i$ is used to estimate a local plane $\boldsymbol{\Pi}(\boldsymbol{\nu}_i, d_i)$ whose equations are given by $\boldsymbol{\nu}_i^T \boldsymbol{x} - d_i = 0$, being d_i the plane distance to the origin and $\boldsymbol{\nu}_i$ its normal vector. Because of the probabilistic nature of our algorithm, we are interested not only in the plane parameters but also in their uncertainty. An iterative method is reported in [31] for this purpose, being too computationally expensive for our case. In [32], the authors use a two-step minimization method for estimating: (1) the plane using region growing algorithms and (2) its uncertainty. Finally, in [33], the error of a set of samples is minimized using the uncertainty related to the range of the sensor by means of a weighted Principal Component Analysis (PCA). This last method is the one which best fits our requirements because of its reduced computational complexity, and also because of its nature, since it does not search for the points forming the plane, but fits the plane among the given points.

Given a plane $\boldsymbol{\Pi}(\boldsymbol{\nu}, d)$, whose equation is $\boldsymbol{\nu}^T \boldsymbol{x} = d$, the likelihood of observing a plane point $\boldsymbol{r}_j \in \boldsymbol{A}_i$ is given by:

$$p(\boldsymbol{r}_j | \boldsymbol{\nu}, d) = \frac{1}{\sqrt{2\pi |\boldsymbol{P}_{\boldsymbol{r}_j}|}} \exp\left((\boldsymbol{\nu}^T \boldsymbol{r}_j - d) * \boldsymbol{\nu})^T \boldsymbol{P}_{\boldsymbol{r}_j}^{-1} ((\boldsymbol{\nu} \boldsymbol{r}_j - d) * \boldsymbol{\nu} \right) \tag{23}$$

The objective here is to maximize the sum of the log-likelihood of the previous equation. The problem cannot be solved in a simple way since the error of the uncertainty depends twice

Sensors **2016**, *16*, 560

on the normal $\boldsymbol{\nu}$. To solve the problem in an efficient way, it was necessary to approximate the uncertainty by the trace of $\boldsymbol{P}_{r_j}$: $\mathrm{Tr}\left(\boldsymbol{P}_{r_j}\right)$. In this way, the error ellipsoid is approximated to a sphere, and it is possible to solve the equation analytically and as efficiently as in [33] (please refer to this work for a more extended derivation).

The log-likelihood that we want to maximize, ignoring constants, is the approximate least squares problem:

$$\ell = \underset{\nu,d}{\operatorname{argmax}} \quad -\frac{1}{2}\sum_{i=1}^{N}\frac{(\boldsymbol{\nu}^T\boldsymbol{r}_j - d)^2}{\mathrm{Tr}\left(\boldsymbol{P}_{r_j}\right)^2} \tag{24}$$

with Lagrangian

$$\mathcal{L} = -\frac{1}{2}\sum_{i=1}^{N}\frac{(\boldsymbol{\nu}^T\boldsymbol{r}_j - d)^2}{\mathrm{Tr}\left(\boldsymbol{P}_{r_j}\right)^2} - \lambda(\boldsymbol{\nu}^T\boldsymbol{\nu} - 1) \tag{25}$$

Setting $\frac{\partial\mathcal{L}}{\partial d} = 0$, we find the solution

$$d_\star = \boldsymbol{\nu}_\star^T\boldsymbol{p}_\mu, \qquad \text{with} \qquad \boldsymbol{p}_\mu = \left(\sum_{i=1}^{N}\mathrm{Tr}\left(\boldsymbol{P}_{r_j}\right)^{-2}\boldsymbol{r}_j\right)\left(\sum_{i=1}^{N}\mathrm{Tr}\left(\boldsymbol{P}_{r_j}\right)^{-2}\right)^{-1} \tag{26}$$

$\boldsymbol{p}_\mu$ being the weighted center of the set of points $\boldsymbol{A}_i$. Finally,

$$\boldsymbol{\nu}_\star = \underset{\nu}{\operatorname{argmin}} \quad \boldsymbol{\nu}^T\left(\sum_{i=1}^{N}\frac{(\boldsymbol{r}_j - \boldsymbol{p}_\mu)(\boldsymbol{r}_j - \boldsymbol{p}_\mu)^T}{\mathrm{Tr}\left(\boldsymbol{P}_{r_j}\right)^2}\right)\boldsymbol{\nu} \tag{27}$$

The minimizing normal $\boldsymbol{\nu}_\star$ is defined by the eigenvalues of the covariance matrix of the points as in the common weighted PCA method. The uncertainty of the estimator is found as:

$$\boldsymbol{P}_f = -\boldsymbol{H}^+ = \begin{pmatrix} \boldsymbol{P}_\nu & \boldsymbol{P}_\nu\boldsymbol{P}_d \\ \boldsymbol{P}_d\boldsymbol{P}_\nu & \boldsymbol{P}_{d,} \end{pmatrix} \tag{28}$$

where $\boldsymbol{H}$ is the Hessian of the Lagrangian in the optimal plane.

Given the point $\boldsymbol{n}_i$ and the plane $\boldsymbol{\Pi}_i(\boldsymbol{\nu}_i, d_i)$ estimated from all the compatible points in $\boldsymbol{A}_i$, the point $\boldsymbol{a}_i$ is defined as the orthogonal projection of $\boldsymbol{n}_i$ over the plane $\boldsymbol{\Pi}_i(\boldsymbol{\nu}_i, d_i)$:

$$\hat{\boldsymbol{a}}_i = \hat{\boldsymbol{q}}_0 \oplus \hat{\boldsymbol{n}}_i - ((\hat{\boldsymbol{q}}_0 \oplus \hat{\boldsymbol{n}}_i)^T\hat{\boldsymbol{\nu}}_i - \hat{d}_i)\hat{\boldsymbol{\nu}}_i \tag{29}$$

$$P_{\boldsymbol{a}_i} = \frac{\partial\boldsymbol{a}_i}{\partial\boldsymbol{q}_0}\boldsymbol{P}_{\boldsymbol{q}_0}\frac{\partial\boldsymbol{a}_i}{\partial\boldsymbol{q}_0}^T + \frac{\partial\boldsymbol{a}_i}{\partial\boldsymbol{n}_i}\boldsymbol{P}_{\boldsymbol{n}_i}\frac{\partial\boldsymbol{a}_i}{\partial\boldsymbol{n}_i}^T + \frac{\partial\boldsymbol{a}_i}{\partial\boldsymbol{\nu}_i}\boldsymbol{P}_{\boldsymbol{\nu}_i}\frac{\partial\boldsymbol{a}_i}{\partial\boldsymbol{\nu}_i}^T + \frac{\partial\boldsymbol{a}_i}{\partial d_i}\boldsymbol{P}_{d_i}\frac{\partial\boldsymbol{a}_i}{\partial d_i}^T \tag{30}$$

This new virtual point $\boldsymbol{a}_i$ is actually the point that will be associated with $\boldsymbol{n}_i$ to execute the new registration phase using the same point-to-point equations we already presented in Equations (20) and (21), but using $\boldsymbol{a}_i$ instead of $\boldsymbol{r}_j$.

3.3. Minimization

At the end of each association stage, a minimization process is executed to estimate the robot displacement $\boldsymbol{q}_{\min}$ that minimizes the addition of the Mahalanobis distance of the association error:

$$\boldsymbol{q}_{\min} = \underset{\boldsymbol{q}}{\operatorname{argmin}}\sum\{\boldsymbol{\xi}\boldsymbol{P}_{\boldsymbol{\xi}}^{-1}\boldsymbol{\xi}\} \tag{31}$$

$\boldsymbol{\xi}$ being a vector composed of all the $\hat{\boldsymbol{e}}_{ij}$ error vectors (see Equation (20)) after associating all the points (either virtual or real) and $\boldsymbol{P}_{\boldsymbol{\xi}}$ the block diagonal matrix with their corresponding covariances $\boldsymbol{P}_{\boldsymbol{e}_{ij}}$ (Equation (21)). This minimization is done using weighted least squares:

$$\boldsymbol{q}_{\min} = [\boldsymbol{J}^T \boldsymbol{P}_{\boldsymbol{\xi}}^{-1} \boldsymbol{J}]^{-1} \boldsymbol{J}^T \boldsymbol{P}_{\boldsymbol{\xi}}^{-1} \boldsymbol{\xi} \tag{32}$$

$\boldsymbol{J}$ being the Jacobian matrix of the error function at the previous estimation evaluated in all the points.

3.4. Submap Simplification

Traditional ICP-based methods may encounter some problems in a scenario like the one depicted in Figure 4a, where two almost flat surfaces share a poorly visible feature. For instance, ICP tends to associate each point with its closest neighbour according to a particular metric. Because of that, it may be difficult to correctly associate the feature areas when the displacement is large (*i.e.*, they are far from each other, and the proximity of flat areas may lead to a local minimum). This particular issue will benefit from the proposed probabilistic ICP approach, since the uncertainty of the points should constrain the possible matching candidates to those compatible with the real accumulated error. For instance, uncertainties may be large in the horizontal plane, making it possible to match two distant features, but small in the z direction, so points in the flat areas will not be compatible with those in the features.

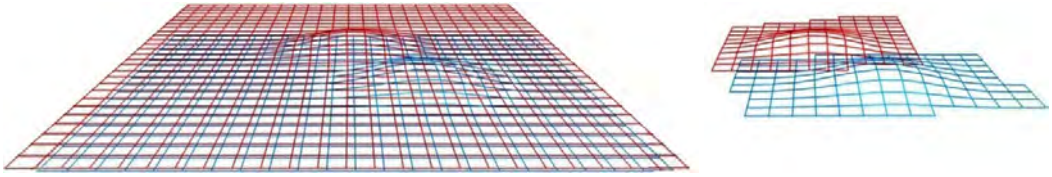

(**a**) (**b**)

Figure 4. A 3D visual concept of the idea behind octree use: two surfaces to be matched (**a**); the same surfaces resampled (**b**).

Another inconvenience related to traditional ICP-based methods is the weak contribution of flat areas to the registration (they all look alike and their matching possibilities are high). Moreover, when few features are present in scenarios of large flat areas, the planar areas may prevail and lead to poor matching. ICP algorithms have better results when the associated points are significant (*i.e.*, distinguishable from each other). For that reason, a new sampling procedure to reduce the number of points in the cloud by removing the less informative ones is presented (see Figure 4b). Since the surface distribution is not available, the sampling procedure is performed using the discrete points. This resampling improves the odds of successful matchings, even when large displacements are present, as well as decreasing the computation time in the registration by drastically decreasing the number of points to be associated, thus increasing the performance of the algorithm.

The approach proposed here uses an octree structure to sample the scan in its most significant areas (*i.e.*, areas with rich relief). The subsampling algorithm works as follows: the point cloud is contained in a discretized tridimensional space structured as an octree. Using the points contained in each cell of the octree, a relief-based subsampling criteria is evaluated recursively, and if the condition is fulfilled, the cell is divided into eight subcells. After the subdivision process comes to an end, only one point is taken from each cell of the octree (see Figure 5). This makes areas with bigger (*i.e.*, not significant) cells contribute with fewer points than areas with smaller (*i.e.*, significant) cells. In [34], several different criteria were studied to drive the octree subdivision. Although some criteria were more suitable for specific types of environments, in this work, the *difference from principal plane* method

Sensors **2016**, *16*, 560 11 of 23

has been selected given its overall performance in both 2.5D and 3D. This criteria basically dictates that a cell should be divided if the average distance between the points in the cell, and the best fitting plane of the cloud is higher than a given threshold. For a more detailed description, please refer to [34].

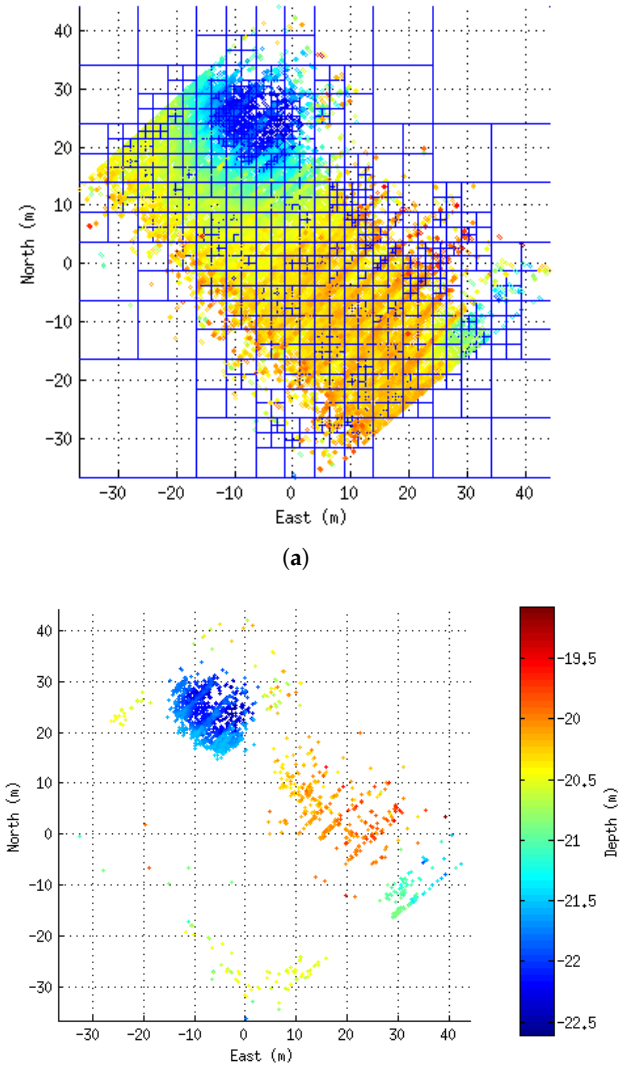

Figure 5. The contribution of octree in point resampling: octree construction, top view (**a**); points after resampling (**b**).

3.5. Association in Linear Time

The association step in ICP based methods has an $O(n^2)$ computational cost because it is necessary to compare each reference point $\boldsymbol{r}_j$ in $\boldsymbol{S}_{ref}$ against all the $\boldsymbol{n}_i$ points in $\boldsymbol{S}_{new}$ to compute their distances. Moreover, the probabilistic implementation of the ICP method requires several matrix operations, including an inversion, to calculate the uncertainty of the association of the points from the two point clouds. Hereafter, a new method for reducing complexity taking advantage of the uncertainty estimates of the points, which are already available, is proposed.

A probabilistic point $\boldsymbol{p}$ with uncertainty $\boldsymbol{P}$ can be represented graphically as an ellipsoid defined by a χ^2 distribution at a certain confidence level α and for d degrees of freedom (DoF):

$$\left\{(\boldsymbol{x}|(\boldsymbol{x}-\boldsymbol{p})^T\boldsymbol{P}^{-1}(\boldsymbol{x}-\boldsymbol{p}) = \chi^2_{d,\alpha}\right\} \tag{33}$$

Given that, in our approach, a 3D grid is generated covering the two patches to be matched, and for each point in $\boldsymbol{S}_{ref}$, the cells falling inside its uncertainty ellipse are marked (see Figure 6a). During the association process, the same procedure is followed for each point in $\boldsymbol{S}_{new}$.

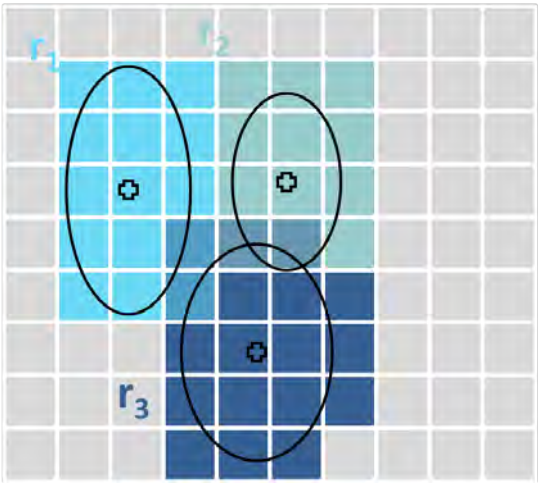

(**a**) Before Matching

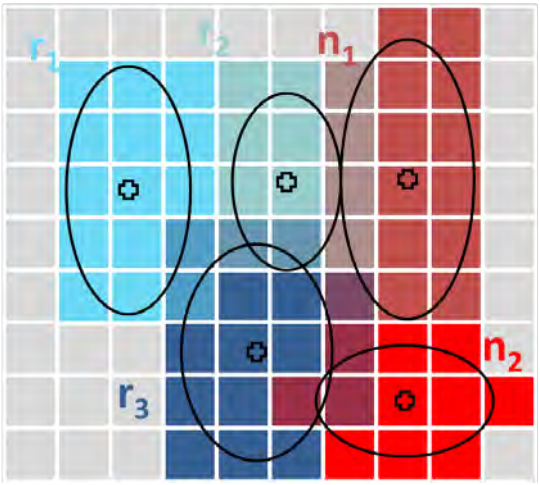

(**b**) During Association

Figure 6. The figure shows how the support grid is used during the association step. First, the points in the reference scan (**blue**) are inserted into the cells using their uncertainty ellipses (**a**). Then, each point in the new scan **(red)** is also laid inside the grid (**b**). In this case, $\boldsymbol{n}_1$ overlaps with $\boldsymbol{r}_2$ and $\boldsymbol{r}_3$ while $\boldsymbol{n}_2$ overlaps only with $\boldsymbol{r}_3$. Moreover, $\boldsymbol{r}_1$ has no potential associations.

Sensors **2016**, *16*, 560

At this point, the following heuristic is applied: To check the compatibility of two points $\boldsymbol{n}_i$ and $\boldsymbol{r}_j$, we define their ellipsoids given a certain confidence level α. If the ellipsoids do not intersect with each other, the corresponding points are assumed not to be individually compatible. In other words, if:

$$\begin{aligned} &\left\{(\boldsymbol{x}|(\boldsymbol{x}-\boldsymbol{n}_i)^T\boldsymbol{P}_{\boldsymbol{n}_i}^{-1}(\boldsymbol{x}-\boldsymbol{n}_i)=\chi^2_{d,\alpha}\right\}\cap \\ &\left\{(\boldsymbol{x}|(\boldsymbol{x}-\boldsymbol{r}_j)^T\boldsymbol{P}_{\boldsymbol{r}_j}^{-1}(\boldsymbol{x}-\boldsymbol{r}_j)=\chi^2_{d,\alpha}\right\}=\emptyset \end{aligned} \tag{34}$$

then,

$$(\boldsymbol{n}_i-\boldsymbol{r}_j)(\boldsymbol{P}_{\boldsymbol{n}_i}+\boldsymbol{P}_{\boldsymbol{r}_j})^{-1}(\boldsymbol{n}_i-\boldsymbol{r}_j)^T>\chi^2_{d,\alpha} \tag{35}$$

Note that evaluating the compatibility in this way is still computationally expensive. However, in our method, the space occupied by the ellipses has been previously registered inside a grid, so it is possible to rapidly find the intersecting ellipsoids using a direct grid look-up (see Figure 6b). In other words, association candidates for a given point in the new scan can be easily identified by searching only among the cells occupied by its own ellipse, for tags denoting occupancy of those same cells by ellipses corresponding to points in the reference scan. In that way, candidates are directly determined, without a need to evaluate all the remaining points in the reference scan, and thus, the complexity is reduced to $O(n)$.

4. SLAM Algorithm

This section describes the EKF implementation of the pose-based SLAM framework in charge of optimizing the surface map.

Every time a submap is finished, the estimate of the robot pose at the reference point of each surface patch $\boldsymbol{x}_S$ is incorporated to the state vector $\boldsymbol{x}$ so it contains all the information regarding the submap distribution:

$$\hat{\boldsymbol{x}}_k=\left[\hat{\boldsymbol{x}}_{S_n}\ \ldots\ \hat{\boldsymbol{x}}_{S_1}\right]_k^T \tag{36}$$

with a pose state $\boldsymbol{x}_S$ being:

$$\boldsymbol{x}_S=[x\ y\ z\ \phi\ \theta\ \psi\ ]^T \tag{37}$$

where (x,y,z) is the position of the robot and (ϕ,θ,ψ) are the roll, pitch and yaw angles. The poses are referred to the same common frame $\mathbb{B}$ that was used during the dead reckoning. The covariance matrix for this state is defined as:

$$\boldsymbol{P}_k=E\left([\boldsymbol{x}_k-\hat{\boldsymbol{x}}_k][\boldsymbol{x}_k-\hat{\boldsymbol{x}}_k]^T\right) \tag{38}$$

4.1. Prediction and State Augmentation

The submap poses stored in the state vector are assumed to be static during the execution of the mission. Therefore, the prediction stage of the EKF just maintains the estimated values for the state vector and its covariance. However, every time a new patch is completed, and its pose is introduced in the state vector. This is done during the prediction stage. To be able to fit the requirements of this algorithm (such as the location of the frame $\mathbb{I}$), a new procedure has been developed for the prediction and state augmentation. The procedure explained hereafter uses the previously computed $\boldsymbol{o}_k$ to find the relationship between the patch $\boldsymbol{S}_n$ and $\boldsymbol{S}_{n+1}$ by adding all the incremental displacements in the xy plane and copying the position of the other 4 DoF at the position chosen as frame $\mathbb{I}$ in patch $\boldsymbol{S}_{n+1}$.

Let $\boldsymbol{S}_{n+1}$ be the new patch to be added to the state vector and $\boldsymbol{S}_n$ the last one already added. Then, we need to estimate the transformation ${}^n\boldsymbol{q}_{n+1}=N({}^n\hat{\boldsymbol{q}}_{n+1},\boldsymbol{P}_{{}^n\boldsymbol{q}_{n+1}})$ relating $\boldsymbol{S}_n$ and $\boldsymbol{S}_{n+1}$. The process begins by defining two functions that will be applied to the set of stored $\boldsymbol{o}_k$ relationships between the two patches:

$$f_1(\hat{\boldsymbol{o}})=f_1\left(\begin{bmatrix}x, & y, & z, & \phi, & \theta, & \psi\end{bmatrix}\right)=\begin{bmatrix}x, & y, & 0, & 0 & 0, & 0\end{bmatrix} \tag{39}$$

$$f_2(\hat{\boldsymbol{o}}) = f_2\left(\begin{bmatrix} x, & y, & z, & \phi, & \theta, & \psi \end{bmatrix}\right) = \begin{bmatrix} 0, & 0, & z, & \phi, & \theta, & \psi \end{bmatrix} \tag{40}$$

with Jacobians:

$$\boldsymbol{F}_1 = \begin{bmatrix} \boldsymbol{I}_{2\times 2} & \boldsymbol{0}_{2\times 4} \\ \boldsymbol{0}_{4\times 2} & \boldsymbol{0}_{4\times 4} \end{bmatrix}, \qquad \boldsymbol{F}_2 = \begin{bmatrix} \boldsymbol{0}_{2\times 2} & \boldsymbol{0}_{2\times 4} \\ \boldsymbol{0}_{4\times 2} & \boldsymbol{I}_{4\times 4} \end{bmatrix} \tag{41}$$

Then, taking the stored $\boldsymbol{O} = \{\boldsymbol{o}_1, ..., \boldsymbol{o}_m\} \in \boldsymbol{S}_n$, the parameter $\boldsymbol{q}_1 = N(\hat{\boldsymbol{q}_1}, \boldsymbol{P}_{q_1})$ representing the distance from the central position of the $\boldsymbol{S}_n$ patch (defined with the subindex mp) and its last position can be calculated as:

$$\hat{\boldsymbol{q}}_1 = \sum_{k=mp+1}^{m} f_1(\hat{\boldsymbol{o}}_k), \qquad \boldsymbol{P}_{q_1} = \sum_{k=mp+1}^{m} \boldsymbol{F}_1 \boldsymbol{P}_{o_k} \boldsymbol{F}_1^T \tag{42}$$

Next, using the stored $\boldsymbol{O} \in \boldsymbol{S}_{n+1}$, the parameter $\boldsymbol{q}_2 = N(\hat{\boldsymbol{q}_2}, \boldsymbol{P}_{q_2})$ representing the distance from the beginning of $\boldsymbol{S}_{n+1}$ to its center plus the final orientation of the patch can be obtained as:

$$\hat{\boldsymbol{q}}_2 = f_2(\hat{\boldsymbol{o}}_{mp}) + \sum_{k=1}^{mp} f_1(\hat{\boldsymbol{o}}_k), \qquad \boldsymbol{P}_{q_2} = \boldsymbol{F}_2 \boldsymbol{P}_{o_{mp}} \boldsymbol{F}_2^T + \sum_{k=1}^{mp} \boldsymbol{F}_1 \boldsymbol{P}_{o_k} \boldsymbol{F}_1^T \tag{43}$$

Finally, the complete transformation ${}^n\boldsymbol{q}_{n+1}$ relating the centers of both patches is calculated as:

$${}^n\hat{\boldsymbol{q}}_{n+1} = \hat{\boldsymbol{q}}_1 + \hat{\boldsymbol{q}}_2, \qquad \boldsymbol{P}_{{}^n\hat{q}_{n+1}} = \boldsymbol{P}_{q_1} + \boldsymbol{P}_{q_2} \tag{44}$$

Knowing this ${}^n\boldsymbol{q}_{n+1}$ transformation, the state of the filter can be augmented with the new position of $\boldsymbol{S}_{n+1}$ by doing:

$$\hat{\boldsymbol{x}}_k^+ = \begin{bmatrix} \hat{\boldsymbol{x}}_{\boldsymbol{S}_n} \odot^n \hat{\boldsymbol{q}}_{n+1} & \hat{\boldsymbol{x}}_{\boldsymbol{S}_n} & \hat{\boldsymbol{x}}_{\boldsymbol{S}_{n-1}} & \dots & \hat{\boldsymbol{x}}_{\boldsymbol{S}_1} \end{bmatrix}_k^T \tag{45}$$

$$\boldsymbol{P}_{\hat{\boldsymbol{x}}_k^+} = \boldsymbol{J}_{1\odot} \boldsymbol{P}_{\hat{\boldsymbol{x}}_k} \boldsymbol{J}_{1\odot}^T + \boldsymbol{J}_{2\odot} \boldsymbol{P}_{{}^n\hat{\boldsymbol{q}}_{n+1}} \boldsymbol{J}_{2\odot}^T \tag{46}$$

Note that the $\odot$ operator is introduced here to define the way in which the global coordinates of the $\boldsymbol{S}_n$ patch are combined with the relationship between consecutive patches $\boldsymbol{S}_n$ and $\boldsymbol{S}_{n+1}$ to find the position of the patch $\boldsymbol{S}_{n+1}$ in the world frame. The $\odot$ operator is described as:

$$\hat{\boldsymbol{x}}_{\boldsymbol{S}_n} \odot^n \hat{\boldsymbol{q}}_{n+1} = \begin{bmatrix} x_{\boldsymbol{x}_{\boldsymbol{S}_n}} + x_{{}^n\hat{\boldsymbol{q}}_{n+1}} \\ y_{\boldsymbol{x}_{\boldsymbol{S}_n}} + y_{{}^n\hat{\boldsymbol{q}}_{n+1}} \\ z_{{}^n\hat{\boldsymbol{q}}_{n+1}} \\ \phi_{{}^n\hat{\boldsymbol{q}}_{n+1}} \\ \theta_{{}^n\hat{\boldsymbol{q}}_{n+1}} \\ \psi_{{}^n\hat{\boldsymbol{q}}_{n+1}} \end{bmatrix} \tag{47}$$

with Jacobians:

$$\boldsymbol{J}_{1\odot} = \begin{bmatrix} \boldsymbol{I}_{2\times 2} & \boldsymbol{0}_{2\times(4+6(n-1))} \\ \boldsymbol{0}_{4\times 2} & \boldsymbol{0}_{4\times(4+6(n-1))} \\ & \boldsymbol{I}_{6n\times 6n} \end{bmatrix}, \quad \boldsymbol{J}_{2\odot} = \begin{bmatrix} \boldsymbol{I}_{6\times 6} \\ \boldsymbol{0}_{6n\times 6} \end{bmatrix} \tag{48}$$

4.2. Matching Strategy

When a new patch is available, potential matches are searched among the previously created patches. This is done by determining the intersection between the volumes $\boldsymbol{B}$ (see Equation (19)) of the two potentially matching patches. In this way, two patches are considered to be intersecting if more than a given % of their volumes is shared. The new patch may potentially intersect with several of the patches that already exist, which may or may not be consecutive in time (see the ones overlapping with patch number 13 in Figure 7). As can also be observed, consecutive patches (such as number 1 and 2, or 8 and 9) may have a small overlap with the new patch. For this reason, a new approach is used that consists in joining consecutive patches to maximize the intersecting area. However, this

Sensors **2016**, *16*, 560

is not recommended for contiguous non-consecutive patches since the drift between them might be significant (e.g., patches number 1 and 6). The proposed approach involves three steps: (1) search for patches intersecting with the new one; (2) search for consecutive patches among those previously selected; and (3) join the patches that are found to be consecutive. The resulting patches are the result of combining the points of the two surfaces and representing them in the frame $\mathbb{I}$ of the earliest created patch.

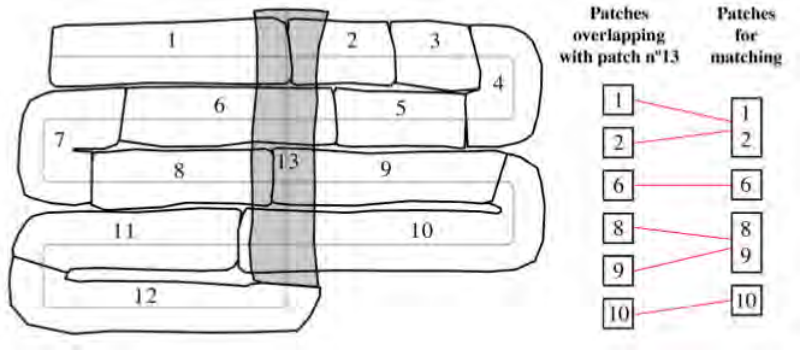

Figure 7. Patch number 13 overlaps with patches 1, 2, 6, 8, 9 and 10. For improving the matching process, patches that are consecutive (1 and 2 as well as 8 and 9) are merged. This results in four patches taking part in the matching process.

4.3. Scan Matching

In order to execute the probabilistic registration algorithm, given two overlapping scans $\boldsymbol{S}_i$ and $\boldsymbol{S}_n$ with related poses $\hat{\boldsymbol{x}}_{\boldsymbol{S}_i}$ and $\hat{\boldsymbol{x}}_{\boldsymbol{S}_n}$, an initial guess $\boldsymbol{q}_0 = N(\hat{\boldsymbol{q}}_0, \boldsymbol{P}_{\boldsymbol{q}_0})$ of their relative displacement is necessary. This can be easily extracted from the state vector using the tail-to-tail transformation:

$$\hat{\boldsymbol{q}}_0 = \ominus \hat{\boldsymbol{x}}_{\boldsymbol{S}_i} \oplus \hat{\boldsymbol{x}}_{\boldsymbol{S}_n} \tag{49}$$

where $\oplus$ and $\ominus$ are the compounding and inverse compounding operators as defined in [30]. Since the tail-to-tail transformation is actually a non-linear function of the state vector $\hat{\boldsymbol{x}}_k$, the uncertainty of the initial guess can be computed using:

$$\boldsymbol{P}_{\boldsymbol{q}_0} = \boldsymbol{H}\boldsymbol{P}_{\boldsymbol{x}_k}\boldsymbol{H}^T \tag{50}$$

where $\boldsymbol{H}$ is the Jacobian computed as:

$$\boldsymbol{H} = [\boldsymbol{J}_{2\oplus_{6\times6}} \;\; \boldsymbol{0}_{6\times6(n-i-1)} \;\; \boldsymbol{J}_{1\oplus}\boldsymbol{J}_{\ominus_{6\times6}} \;\; \boldsymbol{0}_{6\times6(i-1)}] \tag{51}$$

where $\boldsymbol{J}_{1\oplus}$, $\boldsymbol{J}_{2\oplus}$ and $J_{\ominus}$ are the Jacobians of the compounding and inverse compounding functions as defined in [30]. Finally, $\boldsymbol{0}_{6\times6(n-i-1)}$ and $\boldsymbol{0}_{6\times6(i-1)}$ are zero matrices whose dimensions are determined according to the position in the state vector of the surfaces to be registered.

Once the initial displacement guess is available, the registration algorithm presented in Section 3 can be used to produce an updated measurement of this displacement.

4.4. State Update

The initial guess in Equation (49) defines the relationship between two patch poses in the state vector. This can be expressed by means of the following measurement model:

$$\boldsymbol{z}_k = h(\boldsymbol{x}_k, \boldsymbol{v}_k) = \ominus \boldsymbol{x}_{\boldsymbol{S}_i} \oplus \boldsymbol{x}_{\boldsymbol{S}_n} + \boldsymbol{v}_k \tag{52}$$

z_k being the estimated displacement $q_{\min}$ and v_k a zero-mean white Gaussian noise with covariance $P_{q_{\min}}$ accounting for the errors in the registration process. Given that, the standard EKF equations can be used to update the state vector.

5. Experiments and Results

The algorithm has been used to produce the maps for two different underwater datasets. The first one is a bathymetric (2.5D) survey carried out by the *Sirius* AUV [35] on a site of geological interest off the coast of Tasmania (Australia) which has been previously used for bathymetric SLAM [22], while the second one is a full 3D dataset gathered in the Sant Feliu de Guíxols Harbor (Spain) using the *Girona 500* AUV [36] with the multibeam mounted on a pan and tilt unit. The parameters and thresholds that were set for the execution of the algorithm in these experiments can be found in Table 1. Unfortunately, none of the datasets used during the experimental testing have ground truth of the terrain. Therefore, the only option to assess the performance of the algorithm is evaluating the consistency of the resulting map.

Table 1. Thresholds used for the experiments.

	Experiment	
	2.5D	**3D**
Minimum patch size (Section 2.2)	30 m	-
Maximum patch size (Section 2.2)	80 m	-
Normal occupancy (Section 2.2)	23%	-
Patch overlapping (Section 4.2)	30%	30%
Point cloud subsampling (Section 3.4)	0.5 m	1.5 m
Relative displacement to switch from point-to-point to point-to-plane association (Section 3)	1 cm	1 cm

5.1. Bathymetric Survey

This dataset includes depth from a pressure sensor, bottom lock velocities from a DVL, attitude measurements from an AHRS and bathymetric data from a multibeam echosounder installed in the conventional down-looking configuration. The mission surveyed a rectangular area of geological interest several times to generate multiple loop closures. The explored area, mainly flat, has a number of pockmarks with depths of approximately three meters.

Figure 8 shows the elevation maps built using the dead reckoning navigation (Figure 8a) as well as the one obtained with the proposed technique (Figure 8b). In these two maps, it is possible to observe several differences in the pockmarks. While in the corrected solution (Figure 8b), the pockmarks appear clearly and without much bathymetry-related artefacts on the dead reckoning map, and they are blurred and with some artefacts.

To better assess the correction, the consistency-based error [37] is computed for each cell of the bathymetric map. In Figure 9, it can be seen how the areas of high discrepancy (yellow to dark red) on the dead reckoning error map (Figure 9a) are drastically reduced when the proposed technique is applied (Figure 9b). Table 2 contains the numerical evaluation of the results over the bathymetric data. There, it is possible to see that using the 2.5D statistics (Sum and Mean for the consistency-based error) the improvement is around 19%. Moreover, an additional 3D statistic we have named #Cells has been computed. This statistic consists in counting the number of cells that each map occupies within the same 3D grid. If a map occupies less cells, it is probably because their point clouds are more densely packed due to a better registration. Using this statistic, the improvement of the proposed approach compared to the dead reckoning navigation is 2.17%.

Sensors **2016**, *16*, 560

Table 2. Numerical results of the algorithm applied to the pockmarks dataset. The first column (Sum) contains the sum of the error in all the cells, the second one (Mean) contains the mean of the error while the 3rd one (#Cells) contains the number of cells occupied on a 3D grid of 0.5 m resolution.

	Sum	**Mean**	**#Cells**
Dead reckoning	70,986.2	0.3988	37,3121
SLAM	57,521.8	0.3223	36,5014
Improvement *	18.97%	19.2%	2.17%

* The improvement is computed as $\frac{dr-slam}{dr}$ where dr stands for dead reckoning.

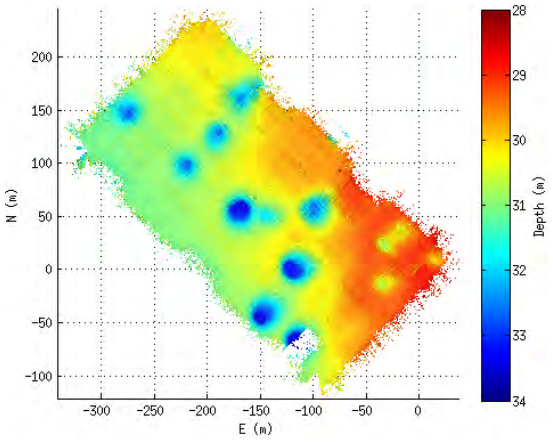

(**a**) Dead Reckoning

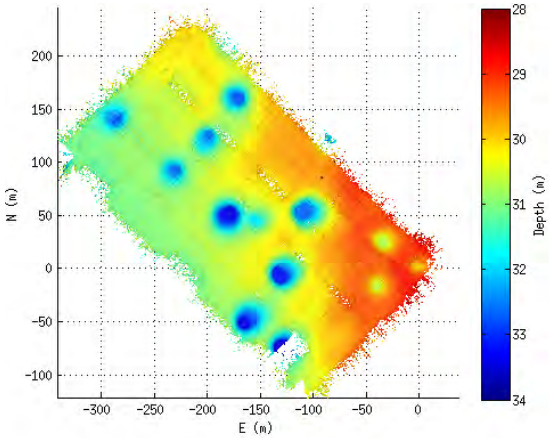

(**b**) SLAM

Figure 8. Bathymetric maps of the area. The color goes from deep (**dark blue**) to shallow (**dark red**). The bathymetry is gridded at 0.5 m. (**a**) Dead Reckoning; (**b**) SLAM.

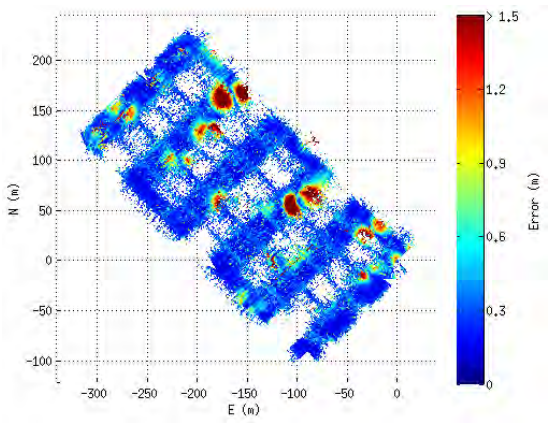

(**a**) Dead Reckoning

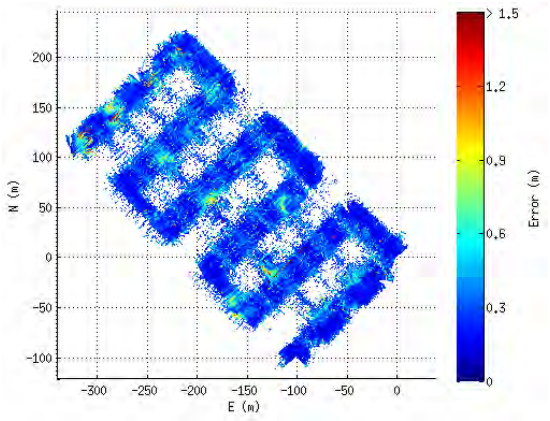

(**b**) SLAM

Figure 9. Consistency-based error maps. The error is color plotted from low (**dark blue**) to high (**dark red**) with 0.5 m grid resolution. (**a**) Dead Reckoning; (**b**) SLAM.

5.2. 3D Experiments

The data was gathered during some field trials for the MORPH European project in 2015. The experiment involved a formation of four marine vehicles (an Autonomous Surface Craft (ASC) and 3 AUVs) exploring a submerged area of the St. Feliu harbor. The *Girona 500* was leading the formation while exploring with the multibeam sonar mounted on a pan and tilt unit (Figure 10) both the seabed and the pier walls, so the formation could be adapted to the presence of obstacles. The mission performed one and a half loops following a zero-shaped trajectory at one corner of the harbor (Figure 11).

During the experiment, the *Girona 500* (Figure 10) was equipped with a DVL, an AHRS, a pressure sensor and a multibeam echosounder. An acoustic modem on *Girona 500* was also used to gather position measurements from a USBL mounted on the ASC navigating on the surface with help of a GPS receiver. The multibeam mounted on the pan and tilt unit allowed us to get full 3D scans by vertically steering the multibeam in front of the robot. Note that, in this experiment, the closure of the surface patches is determined by the completion of a sweep of the pan and tilt, and not by the size or richness of the covered area (see Table 1).

Sensors **2016**, *16*, 560

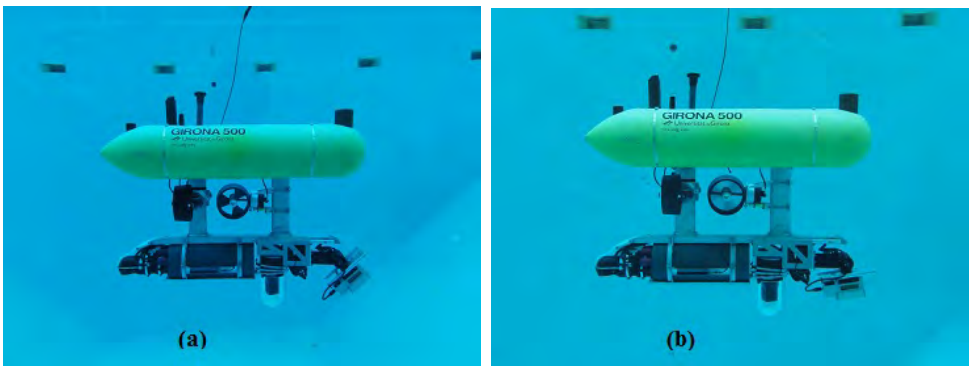

Figure 10. The *Girona 500* AUV in the water tank with the configuration used for the experiments. The multibeam sonar and the pan and tilt unit can be seen at the lower-right side of the vehicle facing in two different directions. In (**a**) the multibeam is tilted at a pitch of around 45º while in (**b**) it is in a downward-looking position.

Figure 11. Trajectory of the experiment over the Google Maps image of the St. Feliu de Guíxols harbor.

As far as we know, there is no general method to evaluate the consistency of a 3D map. However, it is possible to use the 3D statistic #Cells presented in the previous section. As previously commented, if a map occupies fewer cells, it is probably because their point clouds are better registered. Nonetheless, this has to be supervised since it is also possible to find other positions of the point clouds that can minimize the number of occupied cells. For this reason, the consistency of the 3D experiments will also be evaluated subjectively (visually assessing the consistency) as well as numerically (counting the number of occupied cells).

The top view of the 3D maps produced after the experiments are presented in Figure 12. There, three surfaces are created for different navigation methods: dead reckoning (Figure 12a), USBL-aided (Figure 12b) and the currently proposed algorithm (Figure 12c). Regarding the number of occupied cells, the proposed method occupies 32570 cells, 5.76% less than the dead reckoning model (34559)

while the one aided by the USBL occupies 7.24% less cells (32057). Moreover, the black squares represented in each one of the views highlight the places where it is easier to observe the consistency of the map near to the harbor wall. This area is analyzed in detail in Figure 13. In the left column, the one corresponding to the dead reckoning navigation (views Figure 13a,d,g), clearly shows two parallel lines on the point clouds which correspond to the wall being observed during the first and second laps of the mission. In the other two columns, the one corresponding to the USBL navigation (views Figure 13b,e,h), and the one of the proposed SLAM algorithm (views Figure 13c,f,i) show a single wall, and, thus, a better agreement between the different scans. However, if the point cloud from the USBL navigation is analyzed in detail in the bottom left corner (see Figure 13h), there are still some residues of the two observations of the wall that do not appear in the one from the proposed approach.

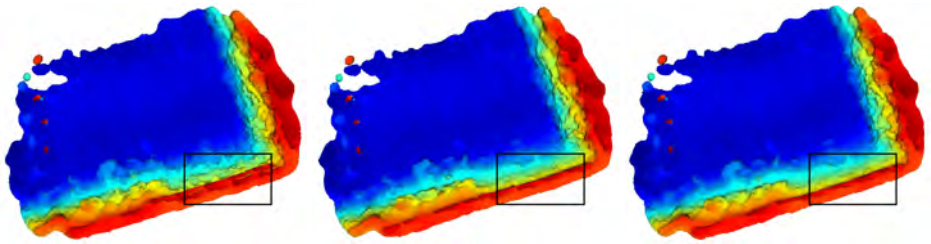

(**a**) Dead Reckoning (34559) (**b**) USBL-aided navigation (32057) (**c**) Proposed approach (32570)

Figure 12. Top view of the 3D reconstruction of St. Feliu Harbor using dead reckoning navigation (**a**), USBL-aided navigation (**b**) and the proposed SLAM algorithm (**c**).The bottom part of the model is the vertical wall of the pier. Under each view, written inside parentheses, the number of cells occupied by each model's point clouds can be observed. The meshes are reconstructed using [38] and colored according to the depth (deeper parts are in blue, shallower ones in red).

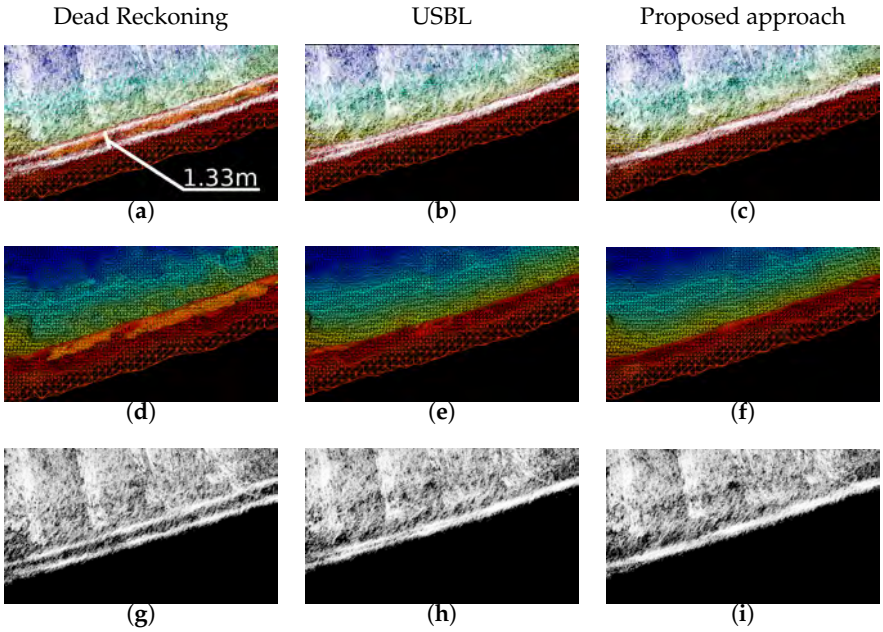

Figure 13. Zoom in the highlighted area of Figure 12. First row (**a**-**c**) shows the point clouds and the reconstructed meshes. Second (**d**–**f**) and third (**g**–**i**) rows show the mesh and point clouds respectively. The columns, from left to right are related to the results obtained with: (1) dead reckoning (**a**, **d** and **g**); (2) USBL-aided (**b**, **e** and **h**) and (3) proposed approach (**c**, **f** and **i**).

6. Conclusions

This paper has presented a probabilistic underwater 3D SLAM for multibeam sonar data that deals with the subdivision of the surface into patches, taking into account the motion uncertainty during their formation. An adaptive sampling procedure for the sensor data has been introduced to deal with areas of the patches that are not relevant (*i.e.*, without relief) to avoid the pICP converging to local minima as well as reducing the computational time. Furthermore, an heuristic has been used to decrease the complexity of the association step of the pICP from $O(n^2)$ to $O(n)$ taking advantage of the probabilistic ellipsoid of each point and using a support grid.

The algorithm has been tested using two real world datasets. In both of them, it is possible to observe how the consistency of the model obtained using the proposed algorithm is higher than that obtained with dead reckoning and is even comparable to the one obtained using USBL navigation in the case of the 3D dataset.

Future work will have to focus on correcting the internal patch error. In the method presented here, only the relative positions of the patches are corrected, but the patch itself is not modified once closed. Although the proposed method has been proved to be useful for obtaining consistent maps, it is not possible to use it online due to its computational cost if the point sampling is not tuned properly. Therefore, further investigation could be done in this field to allow the algorithm to work online. Finally, in the future, we plan to test the algorithm using a camera-laser system, which produces data of similar characteristics to that of a multibeam sonar (2D swath profiles) but with a much different uncertainty level in the measurements.

Acknowledgments: This work was supported by the Spanish project DPI2014-57746-C3-3-R (ARCHROV) and two European Commission's Seventh Framework Program projects: FP7-ICT-2011-7-288704 (MORPH) and FP7-INFRASTRUCTURES-2012-312762 (EUROFLEETS2). We would also like to thank Oscar Pizarro and Stephen Barkby for sharing the bathymetric dataset and information. In addition, we want to thank the staff who permitted the survey mission for the dataset with the *Sirius* AUV, including Ian Mahon, Matthew Johnson-Roberson, Duncan Mercer, George Powell, Ritesh Lal, Paul Rigby, Jeremy Randle and Bruce Crundwell.

Author Contributions: The work presented in this paper has been done as a collaboration by all the authors. Pere Ridao and David Ribas were the project leaders and in charge of the direction and supervision, while Albert Palomer implemented and tested the algorithms with the datasets. All the authors discussed the results obtained and reviewed the manuscript.

Conflicts of Interest: The authors declare no conflict of interest.

References

1. Panish, R.; Taylor, M. Achieving high navigation accuracy using inertial navigation systems in autonomous underwater vehicles. In Proceedings of the MTS/IEEE Oceans, Santander, Spain, 6–9 June 2011; pp. 1–7.
2. Kinsey, J.C.; Whitcomb, L.L. Preliminary field experience with the DVLNAV integrated navigation system for oceanographic submersibles. *Control Eng. Pract.* **2004**, *12*, 1541–1549.
3. Batista, P.; Silvestre, C.; Oliveira, P. Single Beacon Navigation: Observability Analysis and Filter Design. In Proceedings of the American Control Conference (ACC), Baltimore, MD, USA, 30 June–2 Juny 2010; pp. 6191–6196.
4. Vallicrosa, G.; Ridao, P.; Ribas, D. AUV Single Beacon Range-Only SLAM with a SOG Filter. *IFAC Workshop Navig. Guid. Control Underw. Veh.* **2015**, *48*, 26–31.
5. Thomas, H.G. GIB Buoys: An Interface Between Space and Depths of the Oceans. In Proceedings of the Workshop on Autonomous Underwater Vehicles, Cambridge, MA, USA, 20–21 August 1998; pp. 181–184.
6. Mandt, M.; Gade, K.; Jalving, B. Integrateing DGPS-USBL position measurements with inertial navigation in the HUGIN 3000 AUV. In Proceedings of the 8th Saint Petersburg International Conference on Integrated Navigation Systems, Saint Petersburg, Russia, 28–30 May 2001.
7. Carreño, S.; Wilson, P.; Ridao, P.; Petillot, Y.; Carreno, S.; Wilson, P.; Ridao, P.; Petillot, Y. A survey on Terrain Based Navigation for AUVs. In Proceedings of the MTS/IEEE Oceans, Seattle, WA, USA, 20–23 September 2010; pp. 1–7.

8. Bailey, T.; Durrant-Whyte, H. Simultaneous Localization and Mapping (SLAM): Part II. *IEEE Robot. Autom. Mag.* **2006**, *13*, 108–117.
9. Eustice, R.; Pizarro, O.; Singh, H. Visually Augmented Navigation in an Unstructured Environment Using a Delayed State History. In Proceedings of the IEEE International Conference on Robotics and Automation (ICRA), New Orleans, LA, USA, 26 April–1 May 2004; Volume 1, pp. 25–32.
10. Williams, S.; Mahon, I. Simultaneous Localisation and Mapping on the Great Barrier Reef. In Proceedings of the IEEE International Conference on Robotics and Automation (ICRA), New Orleans, LA, USA, 26 April–1 May 2004; Volume 2, pp. 1771–1776.
11. Eustice, R.; Singh, H.; Leonard, J.; Walter, M.; Ballard, R. Visually Navigating the RMS Titanic with SLAM Information Filters. In Proceedings of the Robotics Science and Systems, Cambridge, MA, USA, 8–11 June 2005.
12. Johnson-Roberson, M.; Pizarro, O.; Williams, S.B.; Mahon, I. Generation and Visualization of Large-Scale Three-Dimensional Reconstructions from Underwater Robotic Surveys. *J. Field Robot.* **2010**, *27*, 21–51.
13. Aykin, M.D.; Negahdaripour, S. On Feature Matching and Image Registration for Two-dimensional Forward-scan Sonar Imaging. *J. Field Robot.* **2013**, *30*, 602–623.
14. Hurtós, N.; Ribas, D.; Cufí, X.; Petillot, Y.; Salvi, J. Fourier-based Registration for Robust Forward-looking Sonar Mosaicing in Low-visibility Underwater Environments. *J. Field Robot.* **2015**, *32*, 123–151.
15. Leonard, J.J.; Carpenter, R.N.; Feder, H.J.S. Stochastic Mapping Using Forward Look Sonar. *Robotica* **2001**, *19*, 467–480.
16. Carpenter, R.N. Concurrent Mapping and Localization with FLS. In Proceedings of the Workshop on Autonomous Underwater Vehicles, Cambridge, MA, USA, 20–21 August 1998; pp. 133–148.
17. Williams, S.; Newman, P.; Rosenbaltt, J.; Dissanayake, G.; Durrant-whyte, H. Autonomous underwater navigation and control. *Robotica* **2001**, *19*, 481–496.
18. Newman, P.; Leonard, J. Pure Range-Only Sub-Sea SLAM. In Proceedings of the IEEE International Conference on Robotics and Automation (ICRA), Taipei, Taiwan, 14–19 September 2003; pp. 1921–1926.
19. Ribas, D.; Ridao, P.; Domingo, J.D.; Neira, J. Underwater SLAM in Man-Made Structured Environments. *J. Field Robot.* **2008**, *25*, 898–921.
20. Fairfield, N.; Jonak, D.; Kantor, G.A.; Wettergreen, D. Field Results of the Control, Navigation, and Mapping Systems of a Hovering AUV. In Proceedings of the 15th International Symposium on Unmanned Untethered Submersible Technology, Durham, NH, USA, 19–20 August 2007.
21. Roman, C.; Singh, H. A Self-Consistent Bathymetric Mapping Algorithm. *J. Field Robot.* **2007**, *24*, 23–50.
22. Barkby, S.; Williams, S.B.; Pizarro, O.; Jakuba, M. A Featureless Approach to Efficient Bathymetric SLAM Using Distributed Particle Mapping. *J. Field Robot.* **2011**, *28*, 19–39.
23. Eliazar, A.; Parr, R. DP-SLAM: Fast, Robust Simultaneous Localization and Mapping without Predetermined Landmarks. In Proceedings of the IEEE International Conference on Robotics and Automation (ICRA), Taipei, Taiwan, 14–19 September 2003; Volume 18, pp. 1135–1142.
24. Zandara, S.; Ridao, P.; Ribas, D.; Mallios, A.; Palomer, A. Probabilistic Surface Matching for Bathymetry Based SLAM. In Proceedings of the IEEE International Conference on Robotics and Automation (ICRA), Karlsruhe, Germany, 6–10 May 2013.
25. Hernández, E.; Ridao, P.; Ribas, D.; Mallios, A. Probabilistic sonar scan matching for an AUV. In Proceedings of the IEEE/RSJ International Conference on Intelligent Robots and Systems (IROS), St. Louis, MO, USA, 10–15 October 2009; pp. 255–260.
26. Mallios, A.; Ridao, P.; Ribas, D.; Maurelli, F.; Petillot, Y. EKF-SLAM for AUV navigation under probabilistic sonar scan-matching. In Proceedings of the IEEE/RSJ International Conference on Intelligent Robots and Systems (IROS), Taipei, Taiwan, 18–22 October 2010; pp. 4404–4411.
27. Burguera, A.; Oliver, G.; González, Y. Scan-Based SLAM with Trajectory Correction in Underwater Environments. In Proceedings of the IEEE/RSJ International Conference on Intelligent Robots and Systems (IROS), Taipei, Taiwan, 18–22 October 2010; pp. 2546–2551.
28. Mallios, A.; Ridao, P.; Ribas, D.; Hernández, E. Scan Matching SLAM in Underwater Environments. *Auton. Robots* **2014**, *36*, 181–198.
29. Burguera, A.; González, Y.; Oliver, G. A Probabilistic Framework for Sonar Scan Matching Localization. *Adv. Robot.* **2008**, *22*, 1223–1241.

30. Smith, R.; Self, M.; Cheeseman, P. Chapter 3: Estimating Uncertain Spatial Relationships in Robotics. In *Autonomous Robot Vehicles*; Cox, I.J., Wilfong, G.T., Eds.; Springer: New York, NY, USA, 1990; Volume 1, pp. 167–193.
31. Kanazawa, Y.; Kanatani, K. Reliability of fitting a plane to range data. *IEICE Trans. Inf. Syst.* **1995**, *E78D*, 1630–1635.
32. Weingarten, J. Feature-based 3D SLAM. Ph.D. Thesis, École Polytechinque Fédérale de Lausanne, Lausanne, Switzerland, 6 September 2006.
33. Pathak, K.; Vaskevicius, N.; Birk, A. Revisiting uncertainty analysis for optimum planes extracted from 3D range sensor point-clouds. In Proceedings of the IEEE International Conference on Robotics and Automation (ICRA), Kobe, Japan, 12–17 May 2009; pp. 1631–1636.
34. Palomer, A.; Ridao, P.; Ribas, D.; Mallios, A.; Vallicrosa, G. Octree-Based Subsampling Criteria for Bathymetric SLAM. In Proceedings of the XXXV Jornadas de Automática, Valencia, Spain, 3–5 September 2014; pp. 1–6.
35. Williams, S.; Pizarro, O.; Mahon, I.; Johnson-roberson, M. Chapter 9: Simultaneous Localisation and Mapping and Dense Stereoscopic Seafloor Reconstruction Using an AUV. In *Experimental Robotics: The Eleventh International Symposium*; Springer: Berlin, Geramny, 2009; pp. 407–416.
36. Ribas, D.; Palomeras, N.; Ridao, P.; Carreras, M.; Mallios, A. Girona 500 AUV: From Survey to Intervention. *IEEE ASME Trans. Mechatron.* **2012**, *17*, 46–53.
37. Roman, C.; Singh, H. Consistency based error evaluation for deep sea bathymetric mapping with robotic vehicles. In Proceedings of the IEEE International Conference on Robotics and Automation (ICRA), Orlando, FL, USA, 15–19 May 2006; pp. 3568–3574.
38. Kazhdan, M.; Hoppe, H. Screened Poisson Surface Reconstruction. *ACM Trans. Graph.* **2013**, *32*, 1–13.

3

Underwater 3D Laser Scanners: The Deformation of the Plane

This chapter studies the refraction of light when passing through the viewport that seals a laser line projector. Here we model the laser as a set of rays and follow each path of light through the different reflections and refractions that they suffer. We observe that when the angle between the flat viewport and the laser plane is not perpendicular the projection of the light is distorted (i.e. not a line anymore). In this chapter we compare the state of the art light representation (plane) with our proposed surface (elliptical cone). The experiments show that the elliptical cone better represents the projected light. The proposed work is described in detail and published in the following book chapter:

Title: Underwater 3D laser scanners: The deformation of the plane
Authors: **Albert Palomer**, Pere Ridao, David Ribas, and Josep Forest
Book: Sensing and Control for Autonomous Vehicles: Applications to Land, Water and Air Vehicles
Volume: 474, Pages: 73–88, Published: 2017
DOI: 10.1007/978-3-319-55372-6_4

Albert Palomer, Pere Ridao, David Ribas, and Josep Forest. “Underwater 3D laser scanners: The deformation of the plane”. In: Sensing and Control for Autonomous Vehicles: Applications to Land, Water and Air Vehicles. Edited by Thor I. Fossen, Kristin Y. Pettersen, and Henk Nijmeijer. Volume 474. Springer International Publishing, 2017, pages 73–88.

http://doi.org/10.1007/978-3-319-55372-6_4

Abstract

Development of underwater 3D perception is necessary for autonomous manipulation and mapping. Using a mirror-galvanometer system to steer a laser plane and using triangulation, it is possible to produce full 3D perception without the need of moving the sensor. If the sensor does not meet certain hardware requirements, the laser plane is distorted when it passes through the different media (air–viewport–water). However, the deformation of this plane has not been studied. In this work a ray-tracing model is presented to study the deformation of the laser plane. To validate it, two types of datasets have been used, one synthetically generated using the model presented below, and another one using real data gathered underwater with an actual laser scanner. For both datasets an elliptic cone is fitted on the data and compared to a plane fit (the surface commonly used for triangulation). In the two experiments, the elliptic cone proved to be a better fit than the plane.

Keywords

Incidence Angle

Laser Surface

Laser Plane

Underwater Environment

Elliptic Cone

4

Underwater Laser Scanner: Ray-based Model and Calibration

In this chapter we present a ray-based model and a calibration procedure for a newly developed underwater laser scanner. This work build on top of the previously presented work [7] (see Chapter 3) and uses its proposed elliptical cone to produce real-time high resolution point clouds. The results present different analysis of scanned objects to asses the scanner error. Appendix A presents the mathematical manipulations to solve the system of equations in Eq. (14). This work has been submitted to the following journal and is currently under review:

Title: Underwater Laser Scanner: Ray-based Model and Calibration
Authors: **Albert Palomer**, Pere Ridao, Josep Forest, and David Ribas
Submitted to: IEEE/ASME Transactions on Mechatronics
Quality index: JCR2016 Automation & Control systems, Impact Factor: 4.357, Q1

5

Inspection of an Underwater Structure using Point Cloud SLAM with an AUV and a Laser Scanner

In this chapter we present a pose-based EKF SLAM using the underwater laser scanner developed in the context of this thesis. In this work we use state of the art techniques to register 3D scans gathered with the laser scanner and then update a pose-based EKF SLAM in a similar way as in [1] (see Chapter 2). The laser scanner is mounted onto Girona 500 AUV and used to map in real time an underwater pipe and valve structure while correcting the navigation drift of the robot. This work has been submitted to the following journal and is currently under review:

Title:	Inspection of an Underwater Structure using Point Cloud SLAM with an AUV and a Laser Scanner
Authors:	**Albert Palomer**, Pere Ridao, and David Ribas
Submitted to:	Journal of Field Robotics
Quality index:	JCR2016 Robotics, Impact Factor: 4.882, Q1

6

3D Laser Scanner for Underwater Manipulation

This chapter presents the integration of the underwater laser scanner developed in the context of this thesis with two different manipulation platforms. The work introduces a calibration procedure to determine the laser scanner position with respect to the robotic arm that will be used to perform the manipulation task. In the two different manipulation platform the real-time data gathered with the underwater laser scanner was used to move around a cluttered environment without touching the objects in the first experiment and detect and pick up an object from the bottom of the water tank in the second experiment. The proposed work is described in detail and published in the following book chapter:

Title: 3D Laser Scanner for Underwater Manipulation.
Authors: **Albert Palomer**, Pere Ridao, Dina Youakim, David Ribas, Josep Forest, and Yvan Petillot
Journal: Sensors
Volume: 18, Number: 4, Pages: 1–14, Published: 2018
DOI: 10.3390/s18041086
Quality index: JCR2016 Instruments & Instrumentation, Impact Factor: 2.677, Q1

sensors

MDPI

Article

3D Laser Scanner for Underwater Manipulation

Albert Palomer [1,*], Pere Ridao [1], Dina Youakim [1], David Ribas [2], Josep Forest [1] and Yvan Petillot [3]

1 Computer Vision and Robotics Research Institute (VICOROB), Universitat de Girona, 17003 Girona, Spain; pere@eia.udg.edu (P.R.); dina.isaac@udg.edu (D.Y.); josep.forest@udg.edu (J.F.)
2 IQUA Robotics, 17003 Girona, Spain; david.ribas@iquarobotics.com
3 Ocean Systems Laboratory, Heriot-Watt University, Edinburgh EH14 4AS, UK; y.r.petillot@hw.ac.uk
* Correspondence: apalomer@eia.udg.edu; Tel.: +34-681-08-11-40

Received: 16 February 2018; Accepted: 28 March 2018; Published: 4 April 2018

Abstract: Nowadays, research in autonomous underwater manipulation has demonstrated simple applications like picking an object from the sea floor, turning a valve or plugging and unplugging a connector. These are fairly simple tasks compared with those already demonstrated by the mobile robotics community, which include, among others, safe arm motion within areas populated with a priori unknown obstacles or the recognition and location of objects based on their 3D model to grasp them. Kinect-like 3D sensors have contributed significantly to the advance of mobile manipulation providing 3D sensing capabilities in real-time at low cost. Unfortunately, the underwater robotics community is lacking a 3D sensor with similar capabilities to provide rich 3D information of the work space. In this paper, we present a new underwater 3D laser scanner and demonstrate its capabilities for underwater manipulation. In order to use this sensor in conjunction with manipulators, a calibration method to find the relative position between the manipulator and the 3D laser scanner is presented. Then, two different advanced underwater manipulation tasks beyond the state of the art are demonstrated using two different manipulation systems. First, an eight Degrees of Freedom (DoF) fixed-base manipulator system is used to demonstrate arm motion within a work space populated with a priori unknown fixed obstacles. Next, an eight DoF free floating Underwater Vehicle-Manipulator System (UVMS) is used to autonomously grasp an object from the bottom of a water tank.

Keywords: 3D; underwater; laser; manipulation; point clouds

1. Introduction

Autonomous Underwater Vehicles (AUVs) are mostly used for survey missions. Nevertheless, a large number of potential applications require intervention going beyond their current capabilities (e.g., the maintenance of permanent observatories, submerged oil wells, the search and recovery of black-boxes, etc.). Such applications are currently tackled using work-class Remotely Operated underwater Vehicles (ROVs) with a significant cost dominated by the cost of the ship. Advancing towards Intervention Autonomous Underwater Vehicles (IAUVs) may reduce drastically the cost of these operations. Although scientists have significantly advanced the state of the art during the last decade, today's technology is still far from the capabilities already demonstrated in other robotics fields. For instance, to the best of the authors knowledge, none of the systems reported in the underwater robotics mobile manipulation literature have published experimental results using motion-planning and obstacle avoidance methods, while in other robotic domains (mobile robotics, humanoids, etc.), such techniques are routinely used. Mobile robots have demonstrated the capability to identify objects using depth-RGB images, allowing them to better understand the scene where the manipulation takes

place [1,2]. Knowing the surrounding objects, we introduce semantics in the intervention process. It allows understanding, for instance, which objects are graspable and how they should be grasped, bringing the manipulation operation to the next level. Underwater robots are very far from exhibiting those capabilities. The authors think that one of the reasons explaining why underwater mobile manipulators are so immature with respect to land-based robots is due to the lack of proper sensing devices. With the appearance of the Kinect, 3D sensing has drastically reduced in cost, becoming a very popular sensor for mobile manipulation. Unfortunately, it does not work properly underwater, and a clear alternative does not exist yet.

This paper presents a new real-time 3D laser scanner designed to improve the capabilities of the Underwater Vehicle-Manipulator Systems (UVMSs). The scanner is able to provide 3D scans at different resolutions and frequencies (number of scans per second). A method to calibrate the laser-arm system is also proposed, and the complete system is demonstrated in two applications: (1) an eight Degrees of Freedom (DoF) underwater manipulator moving in a water tank populated with a priori unknown obstacles and (2) an eight DoF Intervention Autonomous Underwater Vehicles (IAUVs) grasping an object from the seabed.

The paper is organized as follows. First, a review of the literature is presented in Section 2. Then, Section 3 explains the mechatronics and Section 4 the calibration methods. The experimental results are presented in Section 5 before concluding in Section 6.

2. Related Work

The research on autonomous underwater intervention goes back to the early 1990s with the pioneering works of OTTER [3], ODIN [4], UNION [5] and AMADEUS [6], although field demonstration did not arrive until the first decade of the 21st Century. The first fully-autonomous intervention at sea, was demonstrated by ALIVE [7], where a hovering-capable AUV was able to home and dock to a sub-sea intervention panel to open/close a valve. In this project, the panel was a priori known, and the features of the panel were used to compute the relative position of the AUV with respect to it. The first object manipulation from a floating vehicle was achieved in 2009 within the SAUVIM project [8]. It demonstrated the capability of searching for an object whose position was roughly known a priori. The object was endowed with artificial landmarks, and the robot autonomously located and hooked it to a recovery device while hovering. The first multi-purpose object search and recovery strategy was demonstrated in the TRIDENTproject in 2012. First, the object was searched using a down-looking camera and photo mosaic techniques. Next, it was demonstrated how to autonomously "hook" the object to a water tank [9]. The experiment was repeated in a harbour environment using a four DoF arm [10], and later on with a seven DoF manipulator equipped with a three-finger hand [11]. In this project, the object was known, and its position was computed using correspondence between the image and a priori model.

Given the importance of Inspection, Maintenance and Repair (IMR) tasks for the offshore industry, representative tasks usually performed by ROVs, like valve turning and connector plugging or unplugging, have been automated with different approaches. Fixed-base, fully-autonomous valve turning has been demonstrated twice. In [7], a mechanical scanning imaging sonar was used to locate and home to a sub-sea panel using visual servoing techniques for docking the vehicle with two hydraulic grasps. Once docked, a hydraulic seven DoF manipulator was used to open/close a valve that was highlighted with a circle. Similarly, [12] used an active localization strategy based on a sum of Gaussian filter to discover the sub-sea panel with which the AUV should interact [13]. Next, visual servoing methods based on the a priori known appearance of the sub-sea panel were used to autonomously dock the robot into a funnel-based docking station. In this case, no latching mechanism was used. Therefore, to keep the AUV docked to the intervention panel, it was necessary to keep pushing it with a small force until the intervention operation was concluded. This resulted in minor motion of the vehicle with respect to the panel and forced the usage of computer vision techniques to detect the valve handle in order to turn it. In the same work, a first autonomous

demonstration of a connector unplugging and plugging operation with a fixed-base was also carried out. In this work, the panel and its texture were known, allowing the vehicle position to be computed from a single image, and an artificial landmark was positioned next to the valve to identify it. The work done by the authors in the PANDORA project demonstrated more a challenging scenario by performing autonomous free-floating valve turning operations on a sub-sea panel using a learning by demonstration paradigm [14]. More recently, a task priority redundancy control approach has been used by the authors for the kinematics control of an UVMS, again to demonstrate the free-floating autonomous valve turning [15]. In these two works, the valve panel was known a priori, providing good robot localization. Moreover, the algorithm had to deal only with the angle of the valve because its position was already known from the panel. Finally, to the best of the authors' knowledge, none of the state of the art underwater works deal with scenes cluttered with obstacles to avoid while executing the manipulation.

Despite all this work, the lack of Kinect-like underwater sensors has forced the use of computer vision techniques instead of 3D point cloud algorithms for autonomous manipulation. The only available sensors that produce 3D point clouds that could be used in for this purposes are: (1) a Kinect mounted in an underwater housing; (2) stereo cameras; and (3) laser scanners. Although the distortion introduced by the viewport can be corrected when using a Kinect in an underwater housing, the infra-red light that it uses is attenuated too fast, reaching only 20-cm distances [16]. In contrast, stereo cameras can work at longer ranges, up to a few meters, but they are constrained to the existence of features in the observed scene. Without features, the stereo pair cannot reconstruct the environment. Laser scanners overcome such a limitation by using structured light projection. Therefore, they work in more scenarios than stereo cameras. However, laser scanners suffer from a distortion on the reconstructed cloud proportional to the motion of the sensor while it was gathering the scan. Already existing laser scanners normally use a laser plane and a fixed camera, being able to reconstruct a single profile. Often, those scanners are actuated with one DoF, in order to be able to provide a sector scan (commonly mounted on a tripod, or from a landed ROV). Since it takes a significant time to gather a sector scan (a few seconds), although they may be appropriate from mapping, they are not suitable for manipulation, which requires a fast scanning speed. Instead, the scanner proposed here steers the laser beam using a fast mirror providing a significantly faster scanning speed enabling advanced manipulation tasks similar to those shown by land mobile manipulators and/or humanoids such as moving a manipulator without colliding with the environment, detecting and identifying an object and its position or grasping that object in a cluttered environment.

3. Mechatronics

In this section, the proposed laser scanner is introduced first, and then, the robotics systems in which it is integrated are presented.

3.1. Laser Scanner

The proposed laser scanner consists of a galvanometer steering a mirror, a laser line projector, a camera and housing with two sealing viewports, one for the camera and one for the laser. The laser is projected into the mirror and reflected to the scene through the laser viewport. The galvanometer actuates the mirror in a way that for each image, the laser line is projected onto a different part of the scene. The camera and the galvanometer are synchronized electronically in a way that, for each galvanometer position, the camera is triggered once. This produces an image on the camera that contains only one single line. By accumulating all the laser points computed for each mirror position during a full scan, the sensor can produce a 3D point cloud similar to the one obtained by stereo imaging or depth cameras (see Figure 1). The proposed laser scanner can operate from 0.5–5 m, depending on water visibility conditions and surface light absorption, at a frame rate from 0.09 Hz at full resolution (0.008 degrees of galvanometer rotation between projected lines) up to 6 Hz at lower resolution (see Figure 2). The combination of the hardware elements (camera and galvanometer-mirror)

in conjunction with the elliptical cone light representation (see Section 4.1.5) makes this scanner faster than state of the art systems.

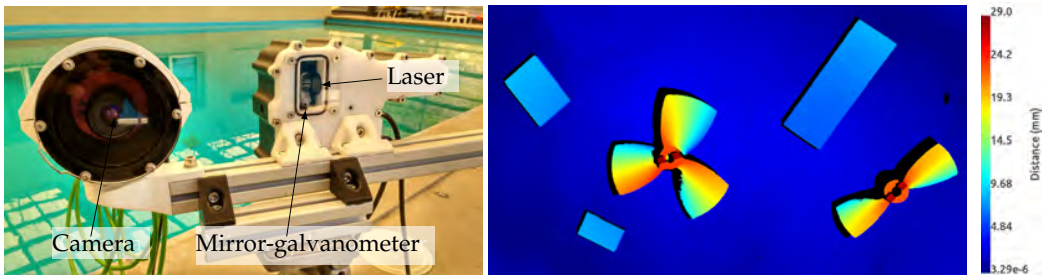

(**a**) (**b**)

Figure 1. The laser scanner mounted on a tripod (**a**) and an example of the point cloud gathered with it coloured according to each point's distance to the background (**b**).

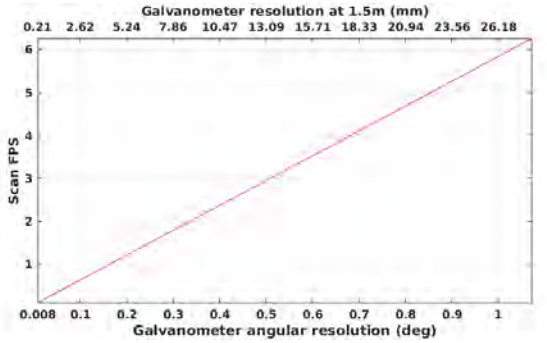

Figure 2. Laser scanner frame rate.

The laser scanner model that describes the sensor is depicted in Figure 3 and consists of: (1) the laser pose with respect to the camera ${}^{\{C\}}\boldsymbol{t}_{\{L\}} = \left[t_x\ t_y\ t_z\ t_\phi\ t_\theta\ t_\psi\right]^T$; (2) the mirror-galvanometer model $\boldsymbol{\Pi} = \{\rho, \delta, {}^{\{C\}}\boldsymbol{t}_{\{M\}}\}$ where ρ is the galvanometer mechanical step (the rotation of the mirror plane around the $\overrightarrow{x}$ axis of the mirror frame $\{M\}$ can be computed using the step s and ρ), δ is the mirror surface distance to the mirror rotation axis and ${}^{\{C\}}\boldsymbol{t}_{\{M\}}$ is the transformation from the camera frame to the mirror frame; (3) the laser viewport $\boldsymbol{\Omega}_L = \{\boldsymbol{\pi}_L\ t_L\}$ with central plane $\boldsymbol{\pi}_L$ and thickness t_L representing the two laser viewport interfaces $\boldsymbol{\pi}_{L,0}$ and $\boldsymbol{\pi}_{L,1}$; (4) the camera model with the pin-hole parameters $\{f_x, f_y, c_x, c_y\}$ and the radial $\{k_1, k_2, k_3\}$ and tangent $\{p_1, p_2\}$ distortion parameters; and (5) the camera viewport $\boldsymbol{\Omega}_C = \{\boldsymbol{\pi}_C\ t_C\}$ representing the two camera viewport interfaces $\boldsymbol{\pi}_{C,0}$ and $\boldsymbol{\pi}_{C,1}$.

Given this model, the path that a ray of light emitted at an angle α around the $\overrightarrow{z}$ direction of $\{L\}$ (i.e., $\boldsymbol{r}_{\alpha,0}$) can be computed using reflection and refraction. The ray $\boldsymbol{r}_{\alpha,0}$ is reflected onto the mirror surface $\boldsymbol{\pi}_s$ at the angular step s producing $\boldsymbol{r}_{\alpha,1}$. This is then refracted on both sides of the laser viewport. First on $\boldsymbol{\pi}_{L,0}$ producing $\boldsymbol{r}_{\alpha,2}$ and then on $\boldsymbol{\pi}_{L,1}$ producing $\boldsymbol{r}_{\alpha,3}$, which is projected onto the scene. The light path on the camera side is traced the opposite way from its actual direction. Therefore, the light path is computed from the camera to the scene. The ray $\boldsymbol{r}_{\boldsymbol{u},2}$, the reflection of $\boldsymbol{r}_{\alpha,3}$ on the scene that lit the pixel $\boldsymbol{u}$, is traced from the camera ray $\boldsymbol{r}_{\boldsymbol{u},0}$. This ray is refracted on both sides of the camera viewport, first with $\boldsymbol{\pi}_{C,0}$ producing $\boldsymbol{r}_{\boldsymbol{u},1}$ and, then, with $\boldsymbol{\pi}_{C,1}$ producing $\boldsymbol{r}_{\boldsymbol{u},2}$.

Given these two light paths, the 3D point associated with the laser detection on the camera image at the pixel $\boldsymbol{u}$ can be computed by intersecting the two rays $\boldsymbol{r}_{\boldsymbol{u},2}$ and $\boldsymbol{r}_{\alpha,3}$. For a camera ray $\boldsymbol{r}_{\boldsymbol{u},2}$, there must be only one laser ray $\boldsymbol{r}_{\alpha,3}$ that intersects with the camera ray, otherwise, the pixel $\boldsymbol{u}$ could not be

Sensors **2018**, *18*, 1086 5 of 18

lit by the laser. To find which α produces the intersection, a minimization process over the distance between the two rays is done. Computing the 3D points using this technique is time consuming because of the minimization process. In [17], the authors present results proving that an elliptical cone surface represents the light after the flat viewport refraction (i.e., the elliptical cone contains the rays $\boldsymbol{r}_{\alpha,3} \forall \alpha \in [\alpha_0, \alpha_1]$ where $\alpha_1 - \alpha_0$ is the aperture of the laser line). Then, the 3D points can be computed by intersecting the ray $\boldsymbol{r}_{u,2}$ with the elliptical cone associated with the mirror position s. Using the elliptical cone offers a clear advantage when compared with the ray intersection technique because the ray-cone intersection has a closed form solution, and there is no iteration process as opposed to the parameter α triangulation. However, this requires an extra calibration step because the elliptical cone for each angle s at which the scanner will work has to be computed (see Section 4.1.5).

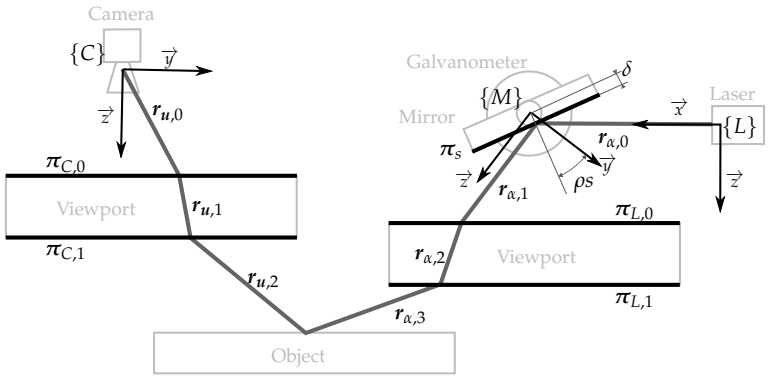

Figure 3. Illustration with the different elements of the sensor (light grey), the elements of the mathematical model (black) and the light path (dark grey).

3.2. Fixed-Based Underwater Manipulator System

The first system used to demonstrate the underwater laser capabilities is a redundant eight DoF robot manipulator (see Figure 4). This manipulator consists of a two DoF Cartesian manipulator and a six DoF robot arm attached to its head. The laser scanner was mounted on a pan and tilt attached to the head of the Cartesian manipulator. A brief description of the components follows.

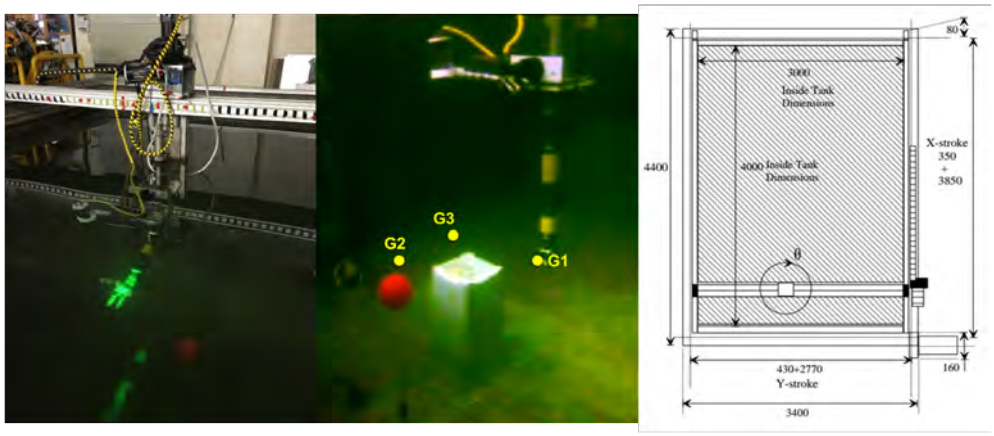

Figure 4. Water tank with the six DoF robot arm mounted on the head of the Cartesian manipulator (**left**); underwater scene with the three way-points defined for the experiment (centre; see Section 5.2); sketch of the Cartesian manipulator (**right**; units in mm).

3.2.1. Cartesian Manipulator

The Cartesian manipulator has three DoF (X, Y and Z) with a length of 3.85 m, 2.77 m and 0.3 m, respectively. Given the small length of the Z axis, only the other two were used. At the end of the Z axis, there is a mechanical head where we attached the robot arm and the laser scanner previously described. The robot controller accepts simple commands to drive the head towards a desired position or to follow desired trapezoidal velocity profiles, amongst others. Moreover, a Robot Operating System (ROS) wrapper developed at the Ocean Systems Laboratory (OSL) was already available, simplifying the integration process with the other systems.

3.2.2. 6 DoF Robotic Arm

The robot arm used was an HDT-Global Adroit-M arm with six DoF equipped with a dexterous hand with three fingers and four DoF. This electrically-driven robot arm rated for a 100-m depth has a length of around 1 m, weighs 10 kg in air and may lift up to 16 kg in air. The arm control software works in ROS providing interfaces to control it in joint or end-effector space. The arm can be controlled in position, velocity and torque.

3.3. Underwater Vehicle Manipulator System

The second system used to demonstrate the underwater laser capabilities for manipulation purposes is a free-floating redundant eight DoF robot manipulator (see Figure 5). In this case, the system consists of the Girona 500 AUV [18] and an ECA/CSIP 5E lightweight underwater arm. The laser scanner was mounted fixed on the Girona 500 payload area.

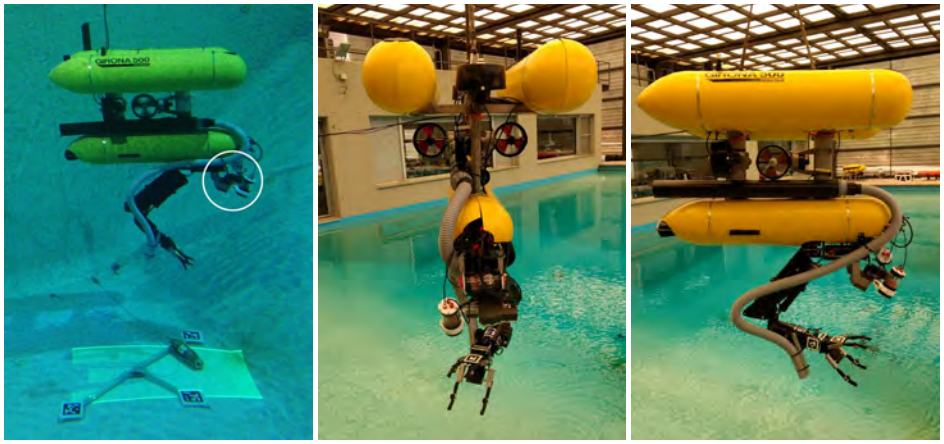

Figure 5. Girona 500 AUV with the four DoF robotic arm and the laser scanner. On the left, the robot is scanning an amphora, and the scanner is highlighted with a white circle. On the centre and on the right, the robot is ready for deployment.

3.3.1. Girona 500 AUV

The Girona 500 AUV is a compact and lightweight vehicle rated for a 500-m depth with survey and intervention capabilities. The overall dimensions of the AUV are 1 m in heigh, 1 m in width and 1.5 m in length with a weight under 200 kg. The two upper hulls contain the flotation, while the lower hull contains more heavy elements such as batteries or the payload area. This makes Girona 500 AUV an especially good vehicle for intervention purposes because its difference between the flotation centre and mass centre provides the AUV with a very good passive stability. With the current thruster configuration, the AUV has four DoF. The vehicle can be controlled in position, velocity and force and is integrated with ROS.

3.3.2. Four DoF Robotic Arm

The robot arm used was an ECA/CSIP Light-Weight ARM 5E. This underwater electrical arm is composed of four revolute joints with reachable distances of 1 m and is equipped with a one DoF gripper. The arm is composed of aluminium partially covered with foam and rated to a 300-m depth. It weighs 29 kg in air, which decreases to 12 kg underwater, and can lift up to 12 kg at full reach. This robotic arm is integrated with ROS, has interfaces to its joint positions and can be controlled in joint or end-effector space.

4. Calibration

This section gives an overall view of the calibration process of the laser scanner presented in Section 4.1. Then, Section 4.2 proposes a calibration method to integrate the laser scanner and the robotic arm so they can be used together in the advanced manipulation tasks presented in Section 5.

4.1. Laser Scanner Calibration

The laser scanner calibration process consists of four steps used to estimate the elements of the model: (1) in-air camera calibration (see Section 4.1.1); (2) in-air laser calibration (see Section 4.1.2); (3) camera viewport calibration (see Section 4.1.3); and (4) laser viewport calibration (see Section 4.1.4). Moreover, instead of using a plane, an elliptic cone is used to model the laser light corresponding to each mirror position (see Section 4.1.5), to deal with the beam distortion induced by the flat viewport. The calibration method presented here is further detailed in [19].

4.1.1. In-Air Camera Calibration

The camera calibration process uses multiple views of a chessboard pattern to produce pairs of 2D image points (pixels detections of each chessboard corner) with the 3D object points (the actual 3D position of each chessboard corner with respect to the chessboard frame in metric units). These pairs of points for different views are used to fit the pin-hole camera model, as well as the lens distortion model. In this work, we use a pin-hole camera model $\{f_x, f_y, c_x, c_y\}$ with a radial $\{k_1, k_2, k_3\}$ and tangent $\{p_1, p_2\}$ distortion model such as the one presented in [20]. During the estimation of these parameters, the camera position with respect to the object is also estimated for each image of the object. The camera calibration is done using the Open Source Computer Vision (OpenCV) library [21] built-in functions.

4.1.2. In-Air Laser Calibration

Using the in-air camera calibration and pairs of laser points retro-projected in the image plane (2D points) and the corresponding 3D laser points (laser projections onto a calibration plane), it is possible to estimate the mirror-galvanometer model $\mathbf{\Pi} = \{\rho, \delta, {}^{\{C\}}\boldsymbol{t}_{\{M\}}\}$ and the laser pose ${}^{\{C\}}\boldsymbol{t}_{\{L\}}$. The calibration data are generated by projecting the laser light at n different galvanometer-mirror steps ($\boldsymbol{s} = \{s_1, \ldots, s_j, \ldots, s_n\}$) onto a planar surface $\boldsymbol{\pi}_{p_i}$ for m camera relative poses $\boldsymbol{t}_i$ ($\boldsymbol{T} = \{\boldsymbol{t}_1, \boldsymbol{t}_2, \ldots, \boldsymbol{t}_m | \boldsymbol{t}_i = \begin{bmatrix} t_{i,x}, t_{i,y}, t_{i,z}, t_{i,\phi}, t_{i,\theta}, t_{i,\psi} \end{bmatrix}\}$) as shown in Figure 6. For each projection plane $\boldsymbol{\pi}_{p_i}$, an estimate ($\hat{\boldsymbol{\pi}}_{p_i}$) of the plane, as well as an estimate of its pose ($\hat{\boldsymbol{t}}_i$) are computed using a visual pattern placed on it. Next, for each combination of estimated projection plane $\hat{\boldsymbol{\pi}}_{p_i}$ and angle step s_j, the set of 3D plane points lit by the laser ($\boldsymbol{P}_{i,j} = \{\boldsymbol{p}_{i,j,1}, \boldsymbol{p}_{i,j,2}, \ldots, \boldsymbol{p}_{i,j,o} | \boldsymbol{p}_{i,j,k} = \begin{bmatrix} p_x & p_y & p_z \end{bmatrix}\}$) is computed by intersecting the ray that passes through each laser detection pixel on the image plane (2D point), with the estimate $\hat{\boldsymbol{\pi}}_{p_i}$ of the corresponding projection plane. Each one of the calibration pairs of points belongs at the same time to two groups: (1) the group of points reconstructing the projection plane $\boldsymbol{P}_{\boldsymbol{\pi}_{p_i}} = \bigcup_{j=1}^{n} \boldsymbol{P}_{i,j}$ (all the points gathered within one scan by steering the mirror along its complete range, scanning a projection plane fixed at a certain pose); and (2) the group of points of a specific mirror position $\boldsymbol{P}_{s_j} = \bigcup_{i=1}^{m} \boldsymbol{P}_{i,j}$ (all the points gathered with the mirror positioned at a certain angle, for all the different poses of the projection plane).

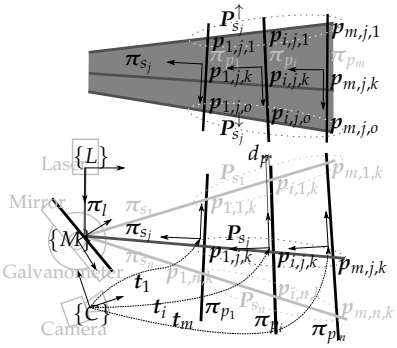

Figure 6. Illustration with all the elements from the air laser calibration. The top part of the figure shows the vertical view of the laser plane $\boldsymbol{P}_{s_j}$. The bottom part shows the top view of the laser scanner and the calibration planes.

The most basic in-air calibration consists of fitting a plane $\hat{\boldsymbol{\pi}}_{s_j}$ amongst the 3D points of each mirror position s_j. With these planes, the first estimation of the mirror-galvanometer model can be computed. The rotation axis of the galvanometer can be computed by averaging all the direction vectors of the intersection line between two consecutive planes $\hat{\boldsymbol{\pi}}_{s_j}$ and $\hat{\boldsymbol{\pi}}_{s_{j+1}}$. This axis defines the $\overrightarrow{x}$ direction of the mirror-galvanometer reference frame. The $\overrightarrow{z}$ direction is the vector perpendicular to the $\overrightarrow{x}$, as well as to the normal of the first plane $\hat{\boldsymbol{\pi}}_{s_0}$. The $\overrightarrow{y}$ is perpendicular to $\overrightarrow{x}$ and $\overrightarrow{z}$. With these three directions defined, the rotation part of ${}^{\{C\}}\boldsymbol{t}_{\{M\}}$ is estimated. The translational part can be computed by averaging the points of the intersecting lines of the planes $\hat{\boldsymbol{\pi}}_{s_j}$ and $\hat{\boldsymbol{\pi}}_{s_{j+1}}$ and the plane $z = 0$. The galvanometer mechanical step ρ can be computed by averaging the angle between all the pairs of planes $\hat{\boldsymbol{\pi}}_{s_j}$ and $\hat{\boldsymbol{\pi}}_{s_{j+1}}$. With the first estimation of the $\boldsymbol{\Pi}$ model, the original laser plane $\boldsymbol{\pi}_l$ that generated each one of the $\boldsymbol{\pi}_{s_j}$ planes for each mirror position s_j can be estimated ($\hat{\boldsymbol{\pi}}_l$) by reflecting each laser plane $\hat{\boldsymbol{\pi}}_{s_j}$ on the mirror and averaging all the reflected planes. With this simplified model for each 3D point, an error can be defined by intersecting the camera ray associated with the 3D point and the reflection of the laser plane $\hat{\boldsymbol{\pi}}_l$ on the mirror at the corresponding position. This error can then be minimized to better estimate this sensor model.

The final part of the in-air laser calibration is estimating the laser focal point, in other words the laser pose ${}^{\{C\}}\boldsymbol{t}_{\{L\}}$, which will be on $\hat{\boldsymbol{\pi}}_l$. For this purpose, each end point of the projected lines is grouped taking into account its mirror position and to which line extreme it corresponds. Therefore, for each galvanometer-mirror position, two groups are created $\boldsymbol{P}^{\uparrow}_{s_j}$ and $\boldsymbol{P}^{\downarrow}_{s_j}$ that contain as many points as relative positions of the laser scanner with respect to the projection plane. Each group of points represents the reflection of the two extreme laser rays on the mirror at step s_j, where $\boldsymbol{P}^{\uparrow}_{s_j}$ is the top and $\boldsymbol{P}^{\downarrow}_{s_j}$ the bottom one. The ray can be computed by fitting a line for each group of points. Then, each fitted ray is reflected with its corresponding mirror position. The laser focal point is computed by finding the point on the plane $\hat{\boldsymbol{\pi}}_l$ that is closer to all the reflected rays. Finally, the laser orientation is fixed by setting the $\overrightarrow{z}$ direction coincident with the normal of the plane $\hat{\boldsymbol{\pi}}_l$, the $\overrightarrow{y}$ direction perpendicular to the $\overrightarrow{z}$ and the normal of the plane $\boldsymbol{\pi}_{s_0}$ and the $\overrightarrow{x}$ direction perpendicular to $\overrightarrow{y}$ and $\overrightarrow{z}$.

4.1.3. Camera Viewport

In this calibration step, the algorithm uses multiple underwater views of a chessboard pattern to produce pairs of 2D image points and the 3D object points, similar to the data used in Section 4.1.1. Given the camera viewport $\boldsymbol{\Omega}_C$ and the transformation of the object to the camera ${}^{\{C\}}\boldsymbol{t}_{\{O\}}$, an error can be defined between the ray that passes through the detected pixel and is refracted on both sides of the viewport and the object point. Using multiple views of the object, a minimization problem can be defined and optimized to estimate the camera viewport $\boldsymbol{\Omega}_C$ and all the object to camera transformations. Figure 7 presents an illustration of the error computation for one position. In this

Sensors **2018**, *18*, 1086 9 of 18

illustration, the object has two 3D points (the two end points of the line). The ray that passes through each one of the pixels corresponding with the end points of the object is refracted on both viewport interfaces $\pi_{C,0}$ and $\pi_{C,1}$. Then, the error e_0 and e_1 between each object end point and its associated ray is computed.

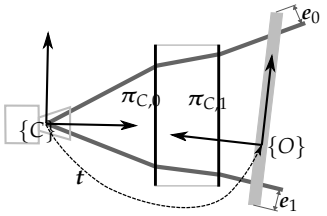

Figure 7. Illustration of the camera viewport calibration error for an object with two 3D points.

4.1.4. Laser Viewport

The laser viewport calibration uses the same type of data as the in-air laser calibration (see Section 4.1.2), but in this case, the plane and the sensor are underwater. For each view of the projection plane, the same minimization process used in the camera viewport calibration (see Section 4.1.3) can be used to estimate the relative pose t_i of the camera and the pattern by setting the camera viewport $\mathbf{\Omega}_C$ as constant. Then, each 3D point associated with each 2D image point of the laser can be computed by refracting the ray that passes through the image point on both sides of the camera viewport $\mathbf{\Omega}_C$ and intersecting it with the projection plane (see the star in Figure 8).

Given the laser viewport $\mathbf{\Omega}_L$ and the rest of the sensor parameters already calibrated, a point can be triangulated by intersecting the camera ray $r_{u,2}$ and the laser ray $r_{\alpha,3}$ (see the pentagon in Figure 8). Although the camera ray is known and computed from the camera intrinsic parameters and the camera viewport (elements from the sensor that have already been calibrated), there is no knowledge of the angle α of the laser ray that intersects the camera ray $r_{u,2}$. However, there is only one ray from the laser that lights up the camera pixel u associated with $r_{u,2}$. The angle α of this laser ray can be computed by minimizing the distance between the two rays $r_{u,2}$ and $r_{\alpha,3}$. An error between this point and its associated original 3D points (see e in Figure 8) can be defined. Minimizing the total error of all the points leads to the laser viewport $\mathbf{\Omega}_L$ estimation.

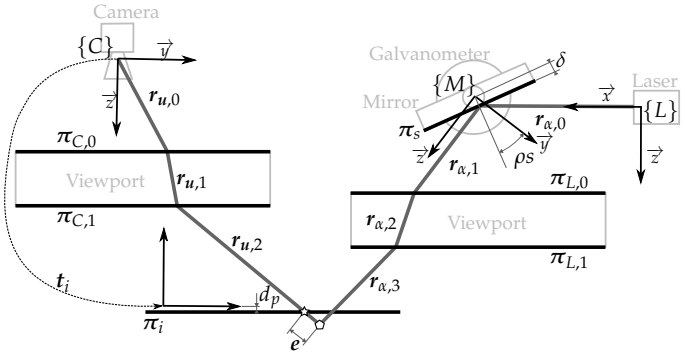

Figure 8. Illustration of the laser viewport calibration error. The star represents the point computed by intersecting the camera ray with the object while the pentagon represents the point computed intersecting the camera ray with the laser ray. Note that the laser ray $r_{\alpha,3}$ and the camera ray $r_{u,2}$ do not intersect in the projection plane π_i because the laser viewport is not estimated properly.

4.1.5. Elliptical Cone Fitting

In [17], the authors presented results proving that an elliptical cone better represents the surface containing the laser light in the underwater medium when a flat viewport is used to seal a laser projector such as the one of the laser scanner. The advantage of such a surface is that it represents well the refraction of the laser plane traversing a flat viewport, and a closed form solution for the ray-surface intersection exists, allowing for a quick triangulation computation.

Using the sensor model fitted during the calibration process, an elliptical cone is computed for each mirror-galvanometer position at which the sensor will operate. For each mirror position, rays are traced from the laser source, reflected on its corresponding mirror and refracted on both sides of the laser viewport. Then, points are sampled along the rays. These points represent the laser light in the underwater medium and are used to fit the elliptical cone for that mirror-galvanometer position.

$\boldsymbol{c}(h,\beta)$ (see Equation (1)) being a cone with its vertex in the origin, its revolution axis along the $\overrightarrow{z}$ direction and aperture a and b in the $\overrightarrow{x}$ and $\overrightarrow{y}$ directions, respectively, the generic cone $\boldsymbol{g}(h,\beta)$ can be computed using a transformation ${}^{\{W\}}\boldsymbol{t}_{\{Q\}}$ (see Equation (2)). Defining $\mathrm{d}(\boldsymbol{p},\boldsymbol{g}(h,\beta))$ as the distance between a point $\boldsymbol{p}$ and the generic elliptical cone $\boldsymbol{g}(h,\beta)$, the parameters a, b and ${}^{\{W\}}\boldsymbol{t}_{\{Q\}}$ minimizing the total addition of the distances of the points sampled on the rays created with the sensor model can be computed. Therefore, the generic cone that represents the laser projected light for that specific mirror-galvanometer position is computed and can be later used for on-line triangulation.

$$\boldsymbol{c}(h,\beta) = \begin{bmatrix} a\,h\,\cos(\beta) & b\,h\,\sin(\beta) & h \end{bmatrix}^T \tag{1}$$

$$\boldsymbol{g}(h,\beta) = {}^{\{W\}}\boldsymbol{t}_{\{Q\}} \oplus \boldsymbol{c}(h,\beta) \tag{2}$$

4.2. Laser Scanner-Arm Calibration

The calibration process consists of finding the relative poses of the different elements of the system so it becomes possible to relate their respective frames. In the case of the AUV equipped with a four DoF manipulator, the scanner was mounted fixed with respect to the manipulator arm (see Section 3.3). In the case of the eight DoF manipulator, the scanner was mounted on a pan and tilt unit whose base was fixed with respect to the base of the robotic arm (see Section 3.2).

To be able to estimate the relative pose of the arm end-effector with respect to the laser scanner, a marker was placed on the end-effector. This marker can be easily located (${}^{\{S\}}\boldsymbol{t}_{\{M\}}$) with respect to the scanner's camera using simple state of the art computer vision techniques [22].

In Figure 9, two kinematics chains linking $\{A_b\}$ and the marker $\{M\}$ are found: (1) $\{A_b\} \rightarrow \{A_{ee}\} \rightarrow \{M\}$ defined by the transformations $\boldsymbol{t}_2 = {}^{\{A_b\}}\boldsymbol{t}_{\{A_{ee}\}}$ and $\boldsymbol{t}_3 = {}^{\{A_{ee}\}}\boldsymbol{t}_{\{M\}}$; and (2) $\{A_b\} \rightarrow \{P_b\} \rightarrow \{P_t\} \rightarrow \{S\} \rightarrow \{M\}$ defined by the transformations $\boldsymbol{t}_4 = {}^{\{A_b\}}\boldsymbol{t}_{\{P_b\}}$, $\boldsymbol{t}_5 = {}^{\{P_b\}}\boldsymbol{t}_{\{P_t\}}$, $\boldsymbol{t}_6 = {}^{\{P_t\}}\boldsymbol{t}_{\{S\}}$ and $\boldsymbol{t}_7 = {}^{\{S\}}\boldsymbol{t}_{\{M\}}$. For a given configuration of the arm and the pan and tilt unit, $\boldsymbol{t}_2$ and $\boldsymbol{t}_5$ are known due to the feedback of the arm and the pan and tilt. Moreover, $\boldsymbol{t}_7$ can be estimated using computer vision techniques, as was done in the calibration section (see Section 4.1.4). Hence, the only unknown transformations are $\boldsymbol{t}_3$, $\boldsymbol{t}_4$ and $\boldsymbol{t}_6$, and the three of them are constant.

Moving the end-effector, as well as the pan and tilt along several poses for which the visual mark is visible by the scanner camera, every time that the marker is detected, four points referenced to the marker frame $\{M\}$ can be added to the set of point used to compute the transformation $\boldsymbol{t}_7$. Since there are two kinematics chains to link the position of $\{M\}$ with $\{A_b\}$, we can define an error on each of these four points by subtracting their positions in the arm base frame $\{A_b\}$ computed through the two different kinematics chains:

$$\boldsymbol{e}_i = \boldsymbol{t}_2 \oplus \boldsymbol{t}_3 \oplus \boldsymbol{p}_i - \boldsymbol{t}_4 \oplus \boldsymbol{t}_5 \oplus \boldsymbol{t}_6 \oplus \boldsymbol{t}_7 \oplus \boldsymbol{p}_i \tag{3}$$

Sensors **2018**, *18*, 1086 11 of 18

With this point error, we can define the following non-linear least squares problem:

$$[\boldsymbol{t}_3,\ \boldsymbol{t}_4,\ \boldsymbol{t}_6] = \underset{[\boldsymbol{t}_3,\, \boldsymbol{t}_4,\, \boldsymbol{t}_6]}{\operatorname{argmin}} \sum_{k} \sum_{i=0}^{3} \boldsymbol{e}_{i,k}^{T} \boldsymbol{e}_{i,k} \tag{4}$$

where k is the set of different configurations of arm pan and tilt where each marker was observed. In the same way, the error can be defined in the AUV with a four DoF manipulator to find the two transformations unknown in that system: ${}^{\{A_b\}}\boldsymbol{t}_{\{S\}}$ and ${}^{\{A_{ee}\}}\boldsymbol{t}_{\{M\}}$. Figure 10 shows a very simple visual confirmation of a correct calibration result. The scanner was used to image the fore arm and the wrist of the eight DoF manipulator. The figure shows how the estimated 3D point cloud overlays the manipulator 3D model, providing an idea about the calibration accuracy.

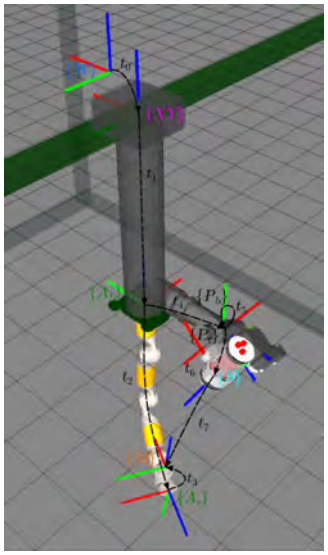

Figure 9. Schematics of the frames involved in the calibration process of the eight DoF manipulator. Each block/actuator has a different colour: $\{W\}$ (blue) is the world reference frame; $\{XY\}$ (pink) is the position of the plotter head; $\{A_b\}$ is the base; $\{A_{ee}\}$ (green) is the end-effector of the robotic arm; $\{M\}$ (red) is the frame of a marker used for the calibration; $\{P_b\}$ is the base; $\{P_t\}$ (black) is the rotated axis of the pan and tilt actuator; and finally, $\{S\}$ (blue) is the frame of the laser scanner. Each one of the $\boldsymbol{t}_i$ represents the transformation between the corresponding reference frames.

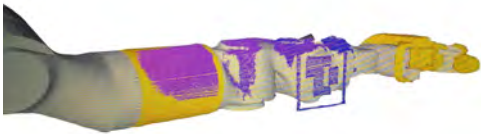

Figure 10. Eight DoF manipulator calibrated. It can be seen how the sensed point cloud overlays the six DoF arm.

5. Experiments and Results

In this section, first an experiment to assess the sensor accuracy is presented followed by the two experiments involving each one of the mechatronics systems. In the two experiments where the sensor is integrated with a manipulator system, it is shown how the scanner allows one to implement an advanced underwater manipulation task beyond the state of the art of current underwater intervention systems, illustrating the utility of the proposed system.

5.1. Sensor Accuracy

This experiments consists of scanning a triangular prism to assess how accurately the 3D points represent the real object. The prism consist of two 58 degree angles separated 200 mm and a third angle of 64 degrees (see Figure 11). In the experiment, it is positioned in a way that both faces with a respective angle of 64 degrees, as well as the 200-mm edge are clearly visible. Then, this angle and longitude are measured for each one of the reconstructions by manually selecting points in the cloud. In the case of the edge of the prism, two points are selected, while in the case of the angle, an area is selected on each face, and the angle between the two normal vectors of the two selected areas is computed. Figure 12 presents one of the evaluated scans gathered underwater. In the figure, it can be seen how the error of the measurement of the edge is below 1 mm and the error of the measured angle is below 0.1 degrees. This has been done for a total of 10 different positions of the prism. The average error for the 10 different positions of the is 0.53 mm with a standard deviation of 0.27 mm. The angle mean error is 0.072 degrees with a standard deviation of 0.015 degrees.

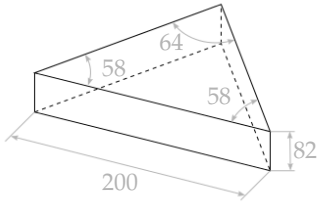

Figure 11. Sketch of the triangular prism used for the experiment. The units are millimetres for the distances and degrees for the angles.

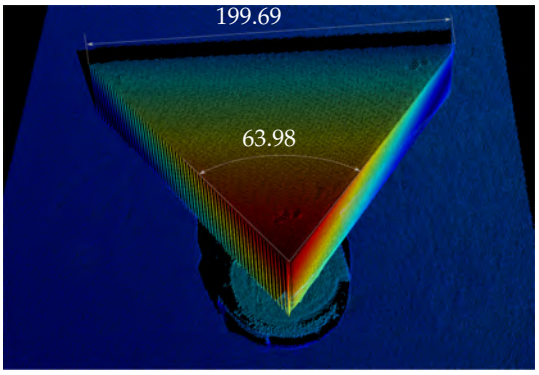

Figure 12. Partial view of a reconstructed area. The cloud has been coloured according to each point's distance to the background for easier interpretation. The units are millimetres for the distance and degrees for the angle.

5.2. Motion Planning of a Fixed-Base Manipulator in the Presence of Unknown Fixed Obstacles

In this experiment MoveIt! [23] is used to plan and control the trajectory of the eight DoF underwater manipulator. MoveIt! is a mobile manipulation software making available state of the art techniques implemented in standard libraries like the Kinematics and Dynamics Library (KDL), the Open Motion Planning Library (OMPL) [24] the Fast Collision Check Library (FCL) [25] and the OCTOMAP [26]. The motion planning problem tackled falls under the category of an unknown/time-invariant environment, given that the robot surroundings are initially unknown to the system, but populated only with static obstacles that will be gradually added to the system map when scanned during the arm motion.

Sensors **2018**, *18*, 1086

For this work, the RRT-connect algorithm [27] was chosen amongst the wide variety of planning algorithms already available at the OMPL. This planner uses the free and occupied space from an OCTOMAP, which is constantly updated using the laser scanner 3D data. Therefore, it is able to plan an obstacle-free path. Moreover, the plan is constantly being checked with the latest OCTOMAP data. In the eventual case that the already planned path collides with a region that becomes occupied when a new obstacle is discovered during the motion, it is aborted. In this case, a new path is computed to reach the final goal without colliding with the new discovered object. This implementation is similar to our previous work in [28], but in this case, instead of dealing with an a priori known map, the laser scanner is used to map the environment in real time during the arm motion.

The experiment consisted of moving the end-effector of the eight DoF manipulator cyclically through three way-points located in a water tank within an area cluttered with unknown obstacles. At the beginning of the experiment, the occupancy map was empty, allowing the trajectories to be planned everywhere in the robot work space due to the absence of obstacles. During the execution of the experiment, the map was constantly updated with the new 3D points of the laser scanner. If the computed trajectory collided with some newly discovered object, the execution was stopped, and a new trajectory towards the goal was computed. The experiment was performed in the water tank of the OSL at Heriot Watt University. A big plastic container (box), as well as two small obstacles (a cup and a sphere) were placed close to each other separating the direct line between the three way-points. Figure 4 shows the environment along with the goals.

Figure 13 shows the end-effector motion along time. The goal way-points are marked with black stars. It can be appreciated from the graph that the arm was reaching each requested goal with accuracy. The end-effector attitude is omitted in Figure 13 as it was kept constant for all three goals during the mission ($[\phi\ \theta\ \psi]^T = [0\ 2\pi\ 0]^T$). Note that the end-effector trajectory changed along the cycles due to the random nature of the RRT-connect path-planning algorithm from one side and due to the fact that during the transit, the environment was being discovered, provoking, sometimes, a trajectory re-planning. Figure 14 shows the arm motion through the working area while it transits for the first time from Way-point 1 to Way-point 2. There, it can be seen how the trajectory stops when the OCTOMAP updates the voxels corresponding to the cup (Frame 4) and how it re-plans to reach Way-point 2 without colliding with the environment. Please see the Supplementary Material for the video of the overall experiment.

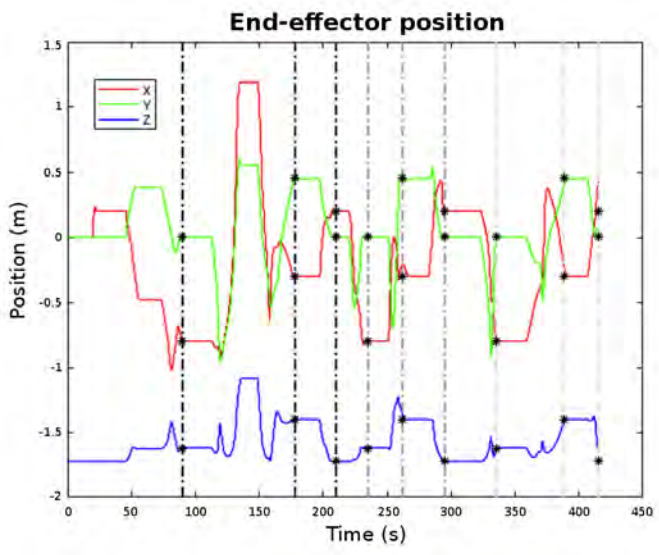

Figure 13. End-effector position with different way-points marked.

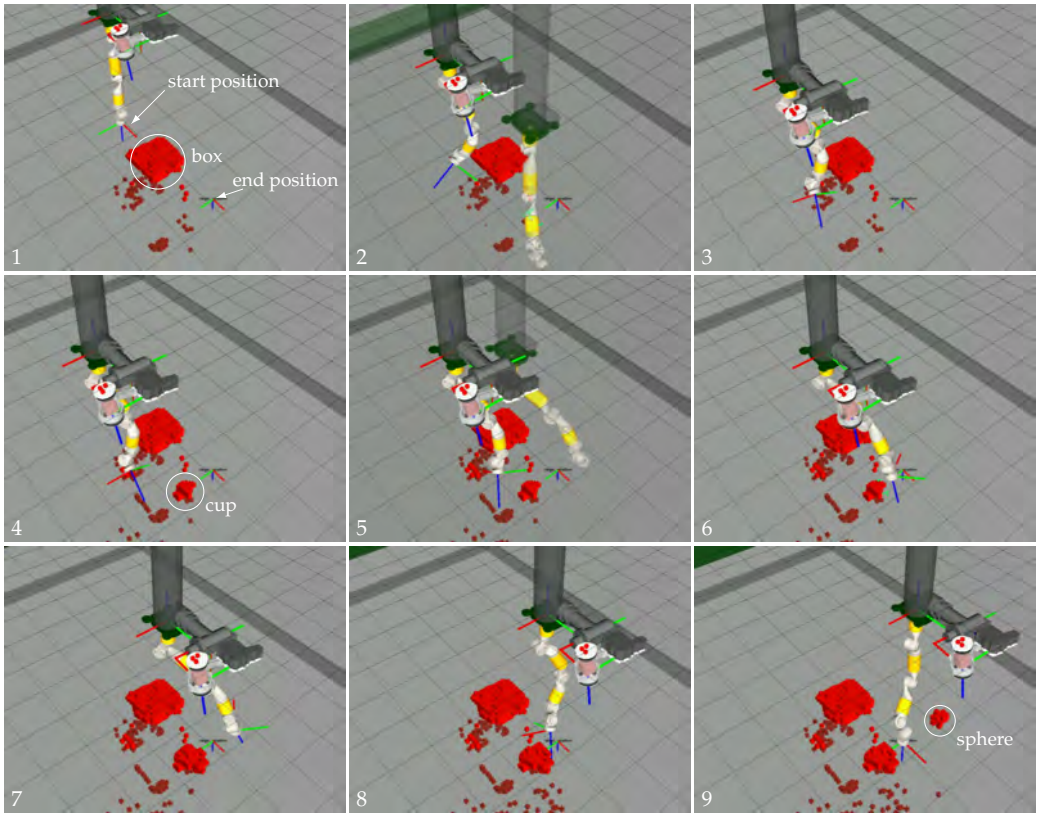

Figure 14. Sequence (**1**–**9**) of one of the trajectories of the eight DoF manipulators from Goal 1 to Goal 2. The shadow robot represents the simulation of the robot following the computed trajectory.

5.3. Object Grasping with a UVMS

In this experiment, the Girona 500 AUV was equipped with the ECA/CSIP Light-Weight ARM 5E and controlled using the task priority framework. The task priority approach is out of the scope of this publication; please see [15] for a detailed description of a similar control system. The experiment consisted of picking up an amphora from the bottom of a water tank, in this case, free of obstacles. During the experiment, the amphora position was computed for every newly available data, providing continuous feedback to the task priority control on the grasping pose. Please see [29] for a description of the grasping pose computation from a point cloud, which is out of the scope of this publication. To avoid end-effector and object collisions, the grasping procedure consisted on two stages. First, the UVMS end-effector was moved to a pose aligned with the grasping pose, but at a safe distance along the $\overrightarrow{z}$ of the grasping pose (approximately 20 cm). Then, the task priority moved the UVMS end-effector to the grasping pose. Finally, when the end-effector reached the grasping pose, the claw was closed, and the UVMS was sent to surface. The experiment was done in the context of the MERBOTS project [30], were two underwater robots cooperate during a semi-autonomous intervention operation. The visual markers placed on the floor of the water tank were used for accurate visual-based navigation, as well as to allow both robots to accurately navigate within the same frame of reference, not being relevant for the the experiment described here.

It can be seen in Figure 15 how the green mesh corresponding to the detected position of the amphora, using a ground-truth marker located on it, corresponds to the amphora position in the point cloud. Moreover, in this same figure, the approach and grasping process is presented in a sequence to demonstrate that the 3D point cloud was being updated in real time during the complete

Sensors **2018**, *18*, 1086

grasping operation (note that the misalignment between the sensed jaw of the robotic arm and the point cloud is because the opening of the jaw is not properly modelled in the 3D viewer). Please see the Supplementary Materials for the video of the overall experiment.

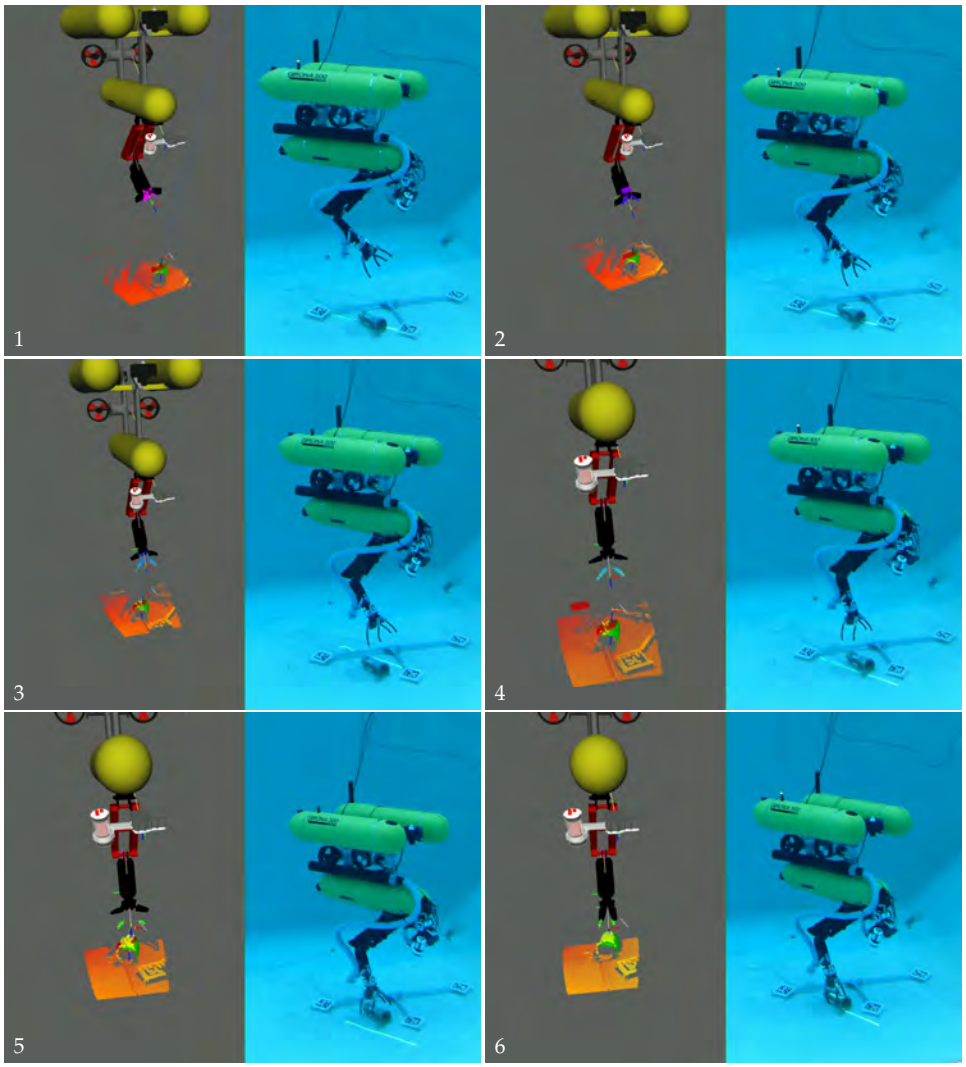

Figure 15. Sequence of images (**1**–**6**) of the 3D visualizer alongside the real scenario while the robot approaches and grasps the amphora.

6. Conclusions and Future Work

This paper has presented an underwater 3D laser scanner and its application to advanced underwater manipulation tasks using two different manipulation systems. The paper described the laser scanner and outlined its calibration method. Moreover, in order to integrate it with an underwater robot arm, a scanner-to-arm calibration method was also proposed and implemented. The sensor accuracy was tested using a known object reconstructed at different distances with measurement errors smaller than one millimetre and 0.1 degrees. Next, the system was demonstrated using and eight DoF fixed-base manipulation system following paths planned in real time. The arm was moved through an environment populated with fixed obstacles located at unknown positions that were discovered during the motion. A second demonstration was done using a UVMS to autonomously

grasp an object from the bottom of a water tank. In both cases, the 3D information provided by the laser scanner was fundamental to complete the task and its accuracy proved to be suitable for the manipulation purposes.

Future work includes further work in correcting the internal error in the scan as a consequence of sensor motion. Increasing the sensor frame rate, this distortion will be reduced because the sensor movement during a scan will decrease. Another approach will be incorporating data from a navigation sensor (such as an Internal Navigation Systems (INS)) to be able to estimate the sensor motion during a scan. It also includes testing of the laser scanning with the state of the art methods for 3D object recognition, in order to introduce semantics for subsea intervention. Moreover, integrating this type of data and object recognition and pose estimation with underwater manipulation systems can help to push the underwater manipulation from the research level to an every-day used technique in the underwater industry.

Supplementary Materials: The Supplementary Materials are available online at http://www.mdpi.com/1424-8220/18/4/1086/s1.

Acknowledgments: This work was supported by the Spanish Project DPI2014-57746-C3-3-R (MERBOTS-ARCHROV), the H2020 Project H2020-TWINN-2015 (CSA)-692427 (STRONGMAR). Pere Ridao was funded by the Salvador Madariaga Grant Number PRX 15/00580 funded by the Spanish Ministry of Education, Culture and Sport. Dina Youakim is funded by the FIGrant Number 2017FI_B1 00177. We would like to thank the team at the Universitat Jaume I in Castelló, Spain, led by Pedro J. Sanz, who provided the four DoF robotic arm for the free-floating UVMS experiment, especially Antonio Peñalver, who implemented the task priority control for that experiment.

Author Contributions: David Ribas designed the mechanical parts and of the the laser scanner. Dina Youakim implemented the motion planing techniques. Albert Palomer designed and implemented both the laser scanner calibration, with the supervision of Josep Forest, as well as the laser scanner to arm calibration procedure. Pere Ridao supervised the work of Dina Youakim and Albert Palomer, programmed the control of the eight DoF robot arm and is the principal investigator of the research project. Yvan Petillot, provided the eight DoF robot arm mechatronics and contributed to the first experiment providing valuable comments and feedback. Albert Palomer, Pere Ridao, Dina Youakim and Yvan Petillot designed and performed the eight DoF manipulator experiment, while the UVMS one was designed and performed by Albert, Dina, Pere and members of the MERBOTS consortium. Albert Palomer wrote the paper, which was supervised by Pere Ridao.

Conflicts of Interest: The authors declare no conflict of interest.

References

1. Hinterstoisser, S.; Cagniart, C.; Ilic, S.; Sturm, P.; Navab, N.; Fua, P.; Lepetit, V. Gradient response maps for real-time detection of textureless objects. *IEEE Trans. Pattern Anal. Mach. Intell.* **2012**, *34*, 876–888.
2. Willow Garage, R.C. ORK: Object Recognition Kitchen. Available online: https://github.com/wg-perception/object_recognition_core (accessed on 3 April 2018).
3. Wang, H.H.; Rock, S.M.; Lees, M.J. Experiments in automatic retrieval of underwater objects with an AUV. In Proceedings of the Conference MTS/IEEE Challenges of Our Changing Global Environment (OCEANS'95), San Diego, CA, USA, 9–12 October 1995; Volume 1, pp. 366–373.
4. Choi, S.; Takashige, G.; Yuh, J. Experimental study on an underwater robotic vehicle: ODIN. In Proceedings of the 1994 Symposium Autonomous Underwater Vehicle Technology (AUV'94), Cambridge, MA, USA, 19–20 July 1994; pp. 79–84.
5. Rigaud, V.; Coste-Maniere, E.; Aldon, M.; Probert, P.; Perrier, M.; Rives, P.; Simon, D.; Lang, D.; Kiener, J.; Casal, A.; et al. UNION: Underwater intelligent operation and navigation. *IEEE Robot. Autom. Mag.* **1998**, *5*, 25–35.
6. Lane, D.; O'Brien, D.J.; Pickett, M.; Davies, J.; Robinson, G.; Jones, D.; Scott, E.; Casalino, G.; Bartolini, G.; Cannata, G.; et al. AMADEUS-Advanced Manipulation for Deep Underwater Sampling. *IEEE Robot. Autom. Mag.* **1997**, *4*, 34–45.
7. Evans, J.; Redmond, P.; Plakas, C.; Hamilton, K.; Lane, D. Autonomous docking for Intervention-AUVs using sonar and video-based real-time 3D pose estimation. In Proceedings of the OCEANS 2003, San Diego, CA, USA, 22–26 September 2003; Volume 4, pp. 2201–2210.
8. Marani, G.; Choi, S.; Yuh, J. Underwater Autonomous Manipulation for Intervention Missions AUVs. *Ocean Eng. Spec. Issue AUV* **2009**, *36*, 15–23.

9. Prats, M.; García, J.; Fernandez, J.; Marín, R.; Sanz, P. Advances in the specification and execution of underwater autonomous manipulation tasks. In Proceedings of the IEEE Oceans 2011, Santander, Spain, 6–9 June 2011; pp. 10361–10366.
10. Prats, M.; García, J.; Wirth, S.; Ribas, D.; Sanz, P.; Ridao, P.; Gracias, N.; Oliver, G. Multipurpose autonomous underwater intervention: A systems integration perspective. In Proceedings of the 2012 20th Mediterranean Conference on Control & Automation (MED), Barcelona, Spain, 3–6 July 2012; pp. 1379–1384.
11. Sanz, P.; Marín, R.; Sales, J.; Oliver, G.; Ridao, P. *Recent Advances in Underwater Robotics for Intervention Missions. Soller Harbor Experiments*; Low Cost Books; Psylicom Ediciones: València, Spain, 2012.
12. Palomeras, N.; Penalver, A.; Massot-Campos, M.; Vallicrosa, G.; Negre, P.; Fernandez, J.; Ridao, P.; Sanz, P.; Oliver-Codina, G.; Palomer, A. I-AUV docking and intervention in a subsea panel. In Proceedings of the 2014 IEEE/RSJ International Conference on Intelligent Robots and Systems (IROS 2014), Chicago, IL, USA, 14–18 September 2014; pp. 2279–2285.
13. Vallicrosa, G.; Ridao, P.; Ribas, D.; Palomer, A. Active Range-Only beacon localization for AUV homing. In Proceedings of the 2014 IEEE/RSJ International Conference on Intelligent Robots and Systems (IROS 2014), Chicago, IL, USA, 14–18 September 2014; pp. 2286–2291.
14. Carrera, A.; Palomeras, N.; Ribas, D.; Kormushev, P.; Carreras, M. An Intervention-AUV learns how to perform an underwater valve turning. In Proceedings of the OCEANS 2014-TAIPEI, Taipei, Taiwan, 7–10 April 2014; pp. 1–7.
15. Cieslak, P.; Ridao, P.; Giergiel, M. Autonomous underwater panel operation by GIRONA500 UVMS: A practical approach to autonomous underwater manipulation. In Proceedings of the 2015 IEEE International Conference on Robotics and Automation (ICRA), Seattle, WA, USA, 26–30 May 2015; pp. 529–536.
16. Digumarti, S.T.; Chaurasia, G.; Taneja, A.; Siegwart, R.; Thomas, A.; Beardsley, P. Underwater 3D capture using a low-cost commercial depth camera. In Proceedings of the 2016 IEEE Winter Conference on Applications of Computer Vision (WACV), Lake Placid, NY, USA, 7–10 March 2016; Volume 1.
17. Palomer, A.; Ridao, P.; Ribas, D.; Forest, J. Underwater 3D laser scanners: The deformation of the plane. In *Lecture Notes in Control and Information Sciences*; Fossen, T.I., Pettersen, K.Y., Nijmeijer, H., Eds.; Springer: Berlin, Germany, 2017; Volume 474, pp. 73–88.
18. Ribas, D.; Palomeras, N.; Ridao, P.; Carreras, M.; Mallios, A. Girona 500 AUV: From Survey to Intervention. *IEEE/ASME Trans. Mech.* **2012**, *17*, 46–53.
19. Palomer, A.; Ridao, P.; Forest, J.; Ribas, D. Underwater Laser Scanner: Ray-based Model and Calibration. *IEEE/ASME Trans. Mech.* **2018**, under review.
20. Heikkila, J.; Silven, O. A four-step camera calibration procedure with implicit image correction. In Proceedings of the IEEE Computer Society Conference on Computer Vision and Pattern Recognition, Washington, DC, USA, 17–19 June 1997; pp. 1106–1112.
21. Bradski, G. The OpenCV Library. *Dobbs J. Softw. Tools* **2000**, *25*, 120–125.
22. Garrido-Jurado, S.; Muñoz-Salinas, R.; Madrid-Cuevas, F.; Marín-Jiménez, M. Automatic generation and detection of highly reliable fiducial markers under occlusion. *Pattern Recognit.* **2014**, *47*, 2280–2292.
23. Sucan, I.A.; Sachin, C. MoveIt! 2013. Available online: http://moveit.ros.org (accessed on 3 April 2018).
24. Şucan, I.A.; Moll, M.; Kavraki, L.; Sucan, I.; Moll, M.; Kavraki, E. The open motion planning library. *IEEE Robot. Autom. Mag.* **2012**, *19*, 72–82.
25. Pan, J.; Chitta, S.; Manocha, D. FCL: A general purpose library for collision and proximity queries. In Proceedings of the IEEE International Conference on Robotics and Automation, Saint Paul, MN, USA, 14–18 May 2012; pp. 3859–3866.
26. Hornung, A.; Wurm, K.M.; Bennewitz, M.; Stachniss, C.; Burgard, W. OctoMap: An Efficient Probabilistic 3D Mapping Framework Based on Octrees. *Auton. Robots* **2013**, *34*, 189–206.
27. Kuffner, J.; LaValle, S. RRT-connect: An efficient approach to single-query path planning. In Proceedings of the 2000 Millennium Conference IEEE International Conference on Robotics and Automation (ICRA), San Francisco, CA, USA, 24–28 April 2000; Volume 2, pp. 995–1001.
28. Youakim, D.; Ridao, P.; Palomeras, N.; Spadafora, F.; Ribas, D.; Muzzupappa, M. MoveIt!: Autonomous Underwater Free-Floating Manipulation. *IEEE Robot. Autom. Mag.* **2017**, *24*, 41–51.

29. Peñalver, A.; Fernández, J.J.; Sanz, P.J. Autonomous Underwater Grasping using Multi-View Laser Reconstruction. In Proceedings of the IEEE OCEANS, Aberdeen, UK, 19–22 June 2017.
30. Sanz, P.J.; Peñalver, A.; Sales, J.; Fernández, J.J.; Pérez, J.; Fornas, D.; García, J.C.; Marín, R. Multipurpose Underwater Manipulation for Archaeological Intervention. In Proceedings of the Sixth International Workshop on Marine Technology MARTECH, Cartagena, Spain, 15–17 September 2015; pp. 96–99.

7

Results and Discussion

In this chapter the main results of the thesis are presented. First we present the results of the multibeam SLAM from Chapter 2 in Section 7.1. Then, the results obtained with the underwater laser scanner are presented in Section 7.2 divided into the model and calibration results (see Section 7.2.1) and the two applications (see Sections 7.2.2 and 7.2.3). Please, note that the figures from Chapters 2 to 6 are not repeated here, only new results incorporate new figures.

7.1 Multibeam SLAM

The SLAM framework presented in Chapter 2 [6] has been tested using two different datasets. The first one, referred as Tasmania dataset, is a dataset kindly provided by Prof. Stefan Williams and Prof. Oscar Pizarro from the Australian Center for Field Robotics (ACFR). It corresponds to an experiment the the robot explores an area of geological interest in Tasmanian waters (Australia). In this experiment, the Sirus AUV was used to gather bathymetric data from a multibeam echosounder mounted in a standard down-looking configuration. Moreover, the vehicle was equipped with navigation sensors for depth (pressure sensor), velocities (DVL) and attitude (AHRS). Because of the multibeam down-looking configuration, this experiment is considered to be 2.5D. The second experiment explores an area in the Sant Feliu de Guíxols harbor (Spain) with Girona 500 AUV. In this experiment, referred as Sant Feliu dataset, the vehicle was also equipped with a pressure sensor, a DVL and an AHRS as well as a USBL to estimate the vehicle position. Moreover, in this case the multibeam echosounder was mounted on a pan and tilt unit. This made the multibeam gather profiles, mechanically scanning an spherical sector, from a down looking configuration to a forward looking one. We consider this is 3D set up.

Besides the datasets reported in the paper corresponding to Chapter 2, the method was also applied to other datasets generated in the context of the CALDERA-Eurofleets (see Section 7.1.3) and the MORPH EU projects (see Section 7.1.4).

7.1.1 Tasmania Dataset

In the 2.5D experiment, the maps resulting of the DR navigation and the SLAM present significant differences, specially in the pockmarks. In the DR map, the pockmarks appear more blurred and with more bathymetric-related artefacts than in the SLAM map. To better assess the quality of the maps, the bathymetric discrepancy can be computed using the Consistency Based Error Evaluation (CBEE) [3]. Using this error metric, we can see how the SLAM map improved the consistency of the DR map around 19%. This is clearly seen in the consistency maps where the yellow to dark red areas in the DR are drastically reduced when compared to the SLAM. Moreover, using the 3D statistic #Cells which consist on counting the number of cells that two different maps occupy in the same grid, the SLAM approach has around 2.17% less occupied cells indicating that their sub-maps are more consistent.

7.1.2 Sant Feliu Dataset

In the 3D experiment, the DR map occupies 34559 cells while the SLAM occupies 32570 cells, 5.76% less. The USBL-aided navigation produced a map occupying 32057 cells (7.24% less than the DR). The increment in consistency pointed out by the occupied cells can be seen in the produced maps and in the highlighted areas. In the detail of the harbor wall we can observe that in the DR navigation there appear two distinct walls separated by 1.33 m. These are the first and second laps of the mission and it is an effect of the accumulated drift of the AUV navigation. In both the SLAM and USBL maps this effect is minimized. In the case of the USBL it is still possible to appreciate some residues of the two observations while in the SLAM that does not appear.

7.1.3 Santorini Dataset

During the Caldera 2012 Eurofleets cruise, the Girona 500 AUV was used to explore the Santorini volcano [23]. The presented results correspond to an exploration mission where the Girona 500 AUV was equipped with a down-looking multibeam to map a lava tongue of geological interest at depth from 280 to 330 m and covering an area of approximately 230 × 300 m navigating at an altitude of 15 m. In this case, the consistency of the maps in the results (see Fig. 7.1) is computed using the standard deviation in depth of the point in each bathymetric cell. The algorithm parameters for this experiments where the same as in the experiments reported in Chapter 2. The error maps show how, the DR error map with total standard deviation 19589.4 m and mean standard deviation 0.247 m is slightly corrected using the SLAM, producing a total standard deviation of 19354.09 m and mean standard deviation of 0.244 m, which represents a 1.20% of improvement with respect to the DR solution. In this case very little improvement is observed. In our opinion this is due to the fact that most of the error present in the map is probably due to a poor roll calibration of the multibeam which cannot be corrected with our SLAM method. This can be appreciated with the cyan color along overlapped parallel tracks corresponding to a different terrain depth observed when the robot moves in inverse directions. Most of the map correction is actually focused on the red spot.

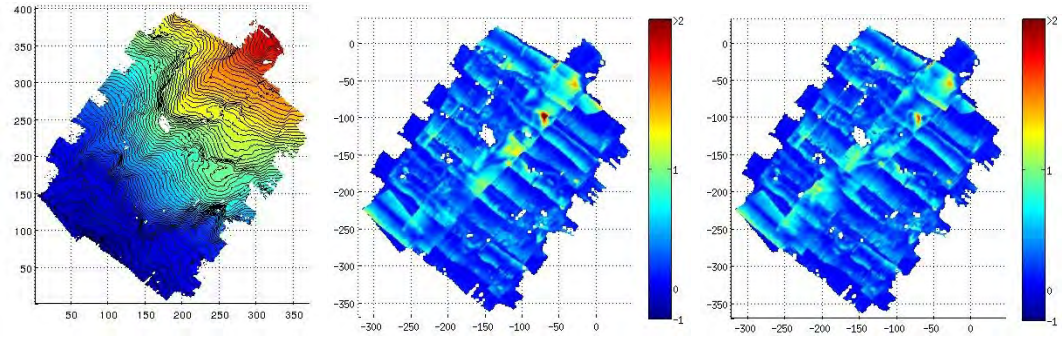

Figure 7.1: Bathymetric map with contours produced using the proposed SLAM algorithm (left) and the standard deviation error maps (m) of the DR (center) and SLAM (right).

7.1.4 Porto Pim Dataset

The data was gathered during the final field trials of the MORPH European project in 2015. Depending on the experiment, 4 or 5 vehicles where involved (at least one Autonomous Surface Craft (ASC) and 3 AUVs). However, the produced maps only use the Girona 500 AUV data. During the field trials, the pan and tilt actuator on Girona 500 AUV was broken, for this reason, the multibeam was mounted into a down-looking configuration as opposed to the Sant Feliu de Guíxols experiment of the project earlier in the year.

The first experiment started on September 10 at 11:44 UTC and consisted on exploring the area in front of an unknown cliff. The second experiment started on September 11 at 11:45 UTC and consisted on following an oval path 5 times over the same area after approaching it from a cross track. The last experiment started on September 11 at 17:08 UTC and consisted on completing 3 turns around a rock of approximately 40x20 m (with a step on the eastern side). The algorithm parameters for this experiments where the

Experiment Number	1	2	3
Experiment Date	Sept 10 11:44	Sept 11 11:45	Sept 11 17:08
DR CBEE	4886.67	8400.57	6379.62
SLAM CBEE	4274.04 (14.29%)	4925.65 (41.37%)	5836.97 (8.51%)
USBL CBEE	3523.93 (29.33%)	3674.66 (56.26%)	5836.97 (4.50%)
DR #Cells	51319	52735	63354
SLAM #Cells	49491 (3.56%)	40342 (23.50%)	60443 (4.59%)
USBL #Cells	49914 (2.74%)	36209 (32.34%)	62125 (1.94%)

Table 7.1: Numerical results of the bathymetric experiments. The percentage indicates the improvement with respect to the DR solution.

same as in the experiments reported in Chapter 2 except for the normal occupancy, set to 30%, and the point cloud subsampling, set to 1 m. The results are presented in Table 7.1 as well as in Figs. 7.2 to 7.4 for experiments 1 to 3 respectively. The results show how the maps produced using our proposed SLAM improve the DR navigation significantly although the results are not as good as with the USBL navigation. In experiment 1 (see Fig. 7.2) the error maps show how the error is reduced, specially in the southern part of the map although it was not completely removed. In experiment 2 (see Fig. 7.3) the DR navigation drifted enough to cover the inner empty part of the oval-shaped trajectory while the SLAM approach produces a much better trajectory. Finally, in experiment 3 the DR did not drift as much as in the previous experiments and the consistency map does not show significant errors (see Fig. 7.4). However, the SLAM is still capable of improving the consistency of the map.

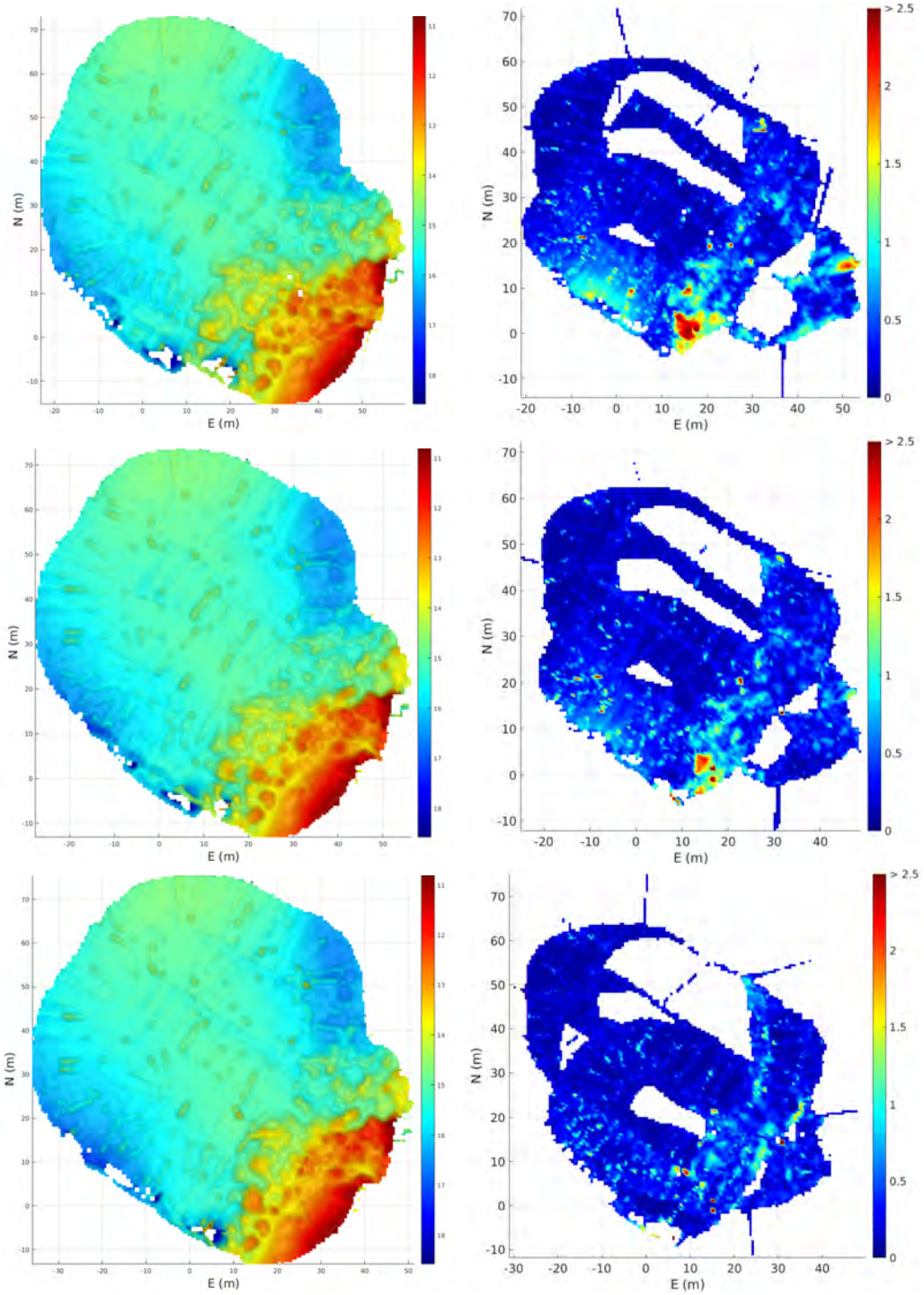

Figure 7.2: Porto Pim experiment 1 bathymetric maps (left) and error maps (right) for DR (top) SLAM (mid) and USBL (bottom). Depth and error (color scale) in m.

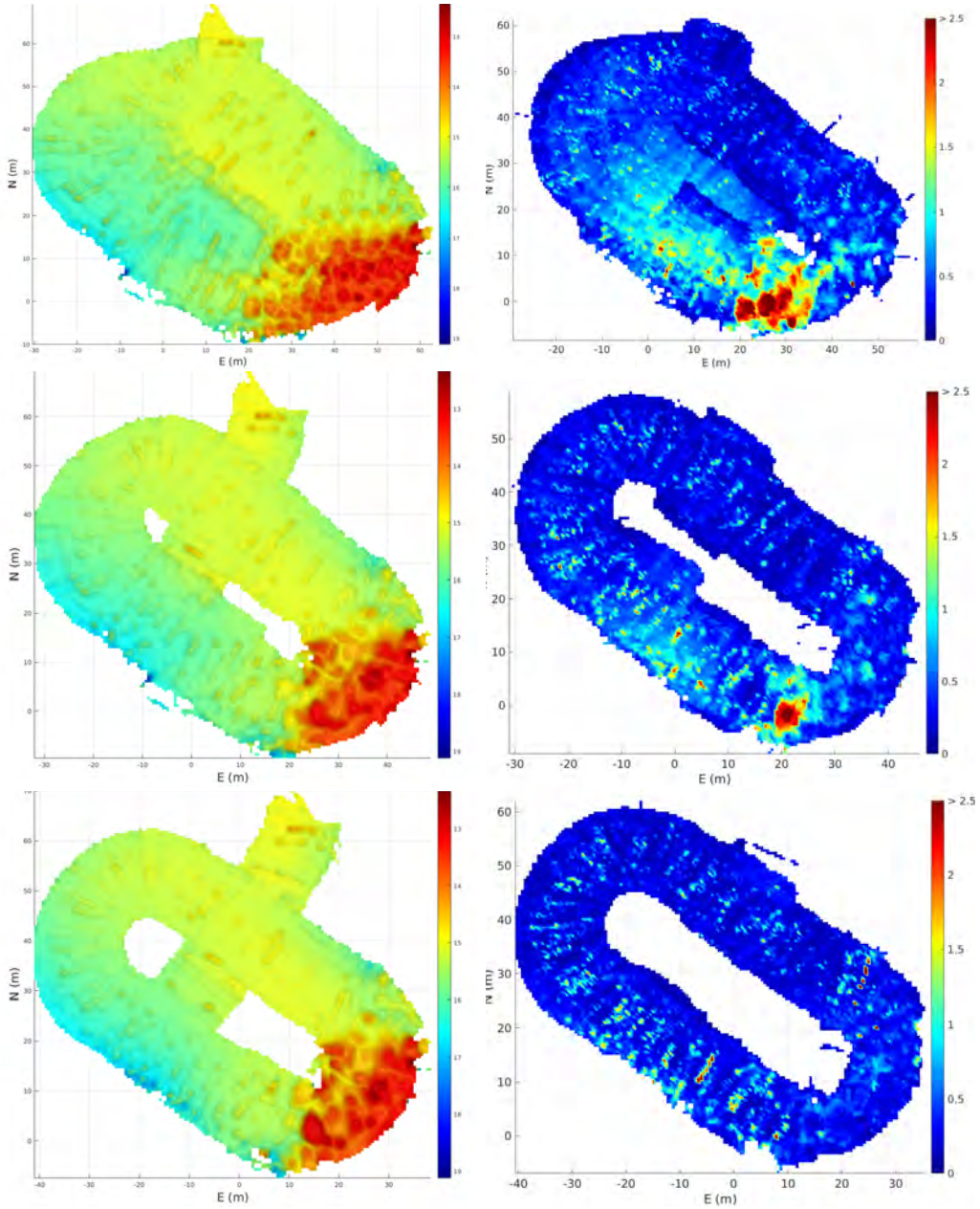

Figure 7.3: Porto Pim experiment 2 bathymetric maps (left) and error maps (right) for DR (top) SLAM (mid) and USBL (bottom). Depth and error (color scale) in m.

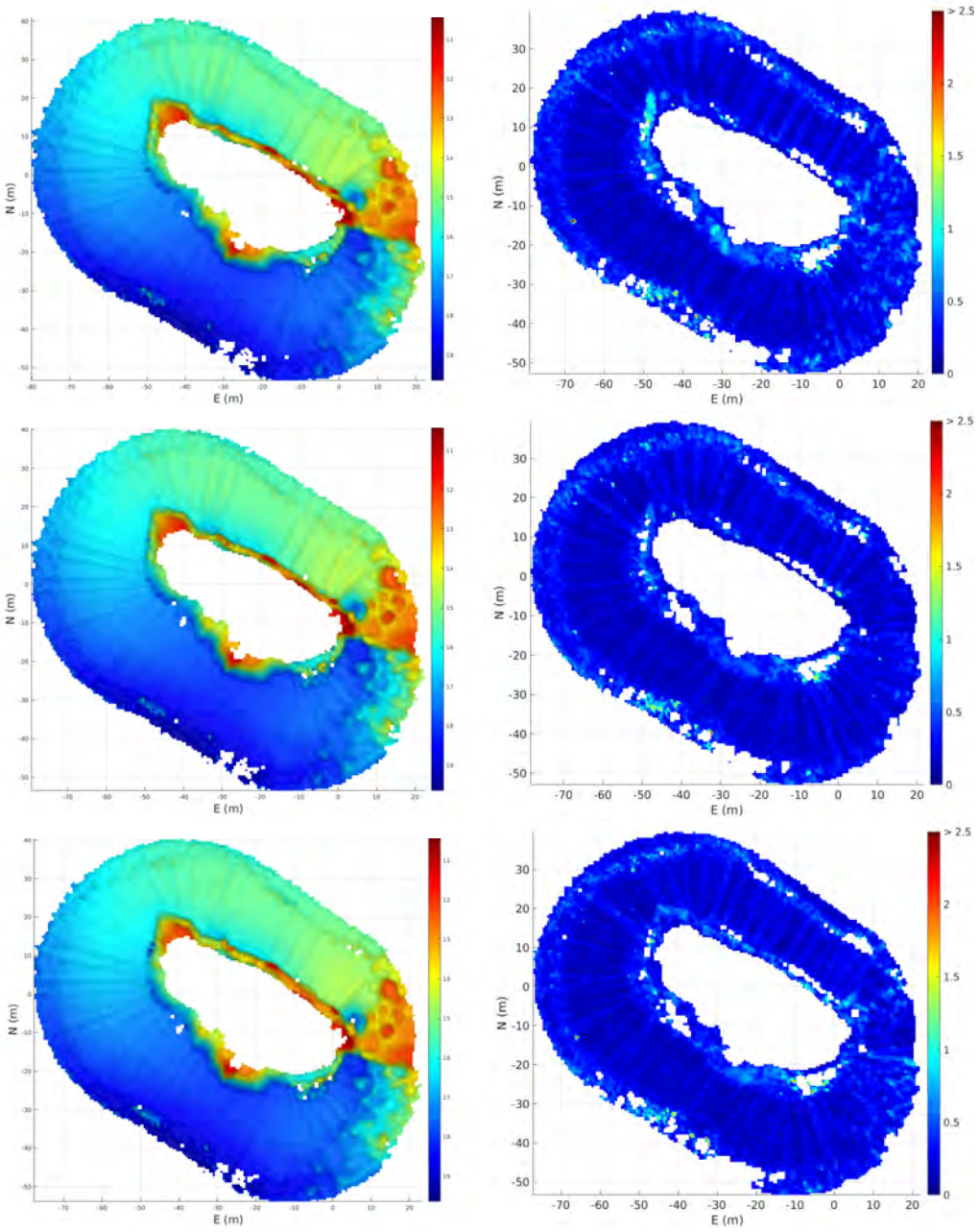

Figure 7.4: Porto Pim experiment 3 bathymetric maps (left) and error maps (right) for DR (top) SLAM (mid) and USBL (bottom). Depth and error (color scale) in m. Note that the step in the eastern side of the map is not an artifact.

7.2 Underwater Laser Scanner

This section discusses the different results of the four works regarding the underwater laser scanner. Section 7.2.1 presents a summary of the results of the model and calibration of the underwater laser scanner Then, the results of the SLAM algorithm proposed in Chapter 5 [5] are presented in Section 7.2.2. Finally, Section 7.2.3 presents the results of the manipulator system introduced in Chapter 6 [6].

7.2.1 Model and Calibration

The model and calibration results include the elliptical cone proposed in Chapter 3 [7], the overall ray-based model and calibration procedure in Chapter 4 [4] and also accuracy results from Chapter 6 [6]. Moreover, this section incorporates the discussion of the limits of the elliptical cone representation of the laser light as well as a comparison between a reconstructed underwater scene using the planar model and the elliptical cone one.

Elliptical Cone

The laser light projection model matched the empiric observations of the laser scanner showing that the light is bent in a way that, when the incidence angle between the laser plane and the viewport is not perpendicular, the projection of the light becomes non linear. This means that the surface containing the different rays of light underwater is not planar, hence, we proposed to use an elliptical cone to represent the underwater laser light. To assess how an elliptical cone better describes the projected light underwater, we compared to the standard plane representation used by the state of the art methods.

Using the ray-based model of the laser light projection, we computed 35 synthetic rays distributed in 55° of laser aperture for angles between the laser incidence plane and the viewport ranging from 0° to 22°. These rays are reflected and refracted according to the model and 5 points are taken on each ray at 100 mm intervals starting 100 mm far from the outer part of the viewport. Using these synthetic points that represent the modeled light, we fit a plane and an elliptical cone for each incidence angle. While the worst fitting error of the plane is almost 0.85 mm in the most extreme angle, the maximum error of the elliptical cone fitting is 0.19 mm representing an improvement of 77.1%. Moreover, it does not increase with the angle of incidence.

To confirm the hypothesis that the elliptical cone is a better representation of the light projected surface, the same two surfaces were fitted amongst real 3D points. The laser scanner was used to project light onto a planar surface at different relative positions of the scanner and the surface. Then, the 3D points used to fit the plane and the elliptical cone were computed in the same way as the underwater viewport calibration 3D points (see Chapter 4). Although the fitting errors are bigger than the ones obtained with the synthetic dataset, the overall behavior is similar. In this case, the fitting error results confirm that the elliptical cone, with fitting errors around 0.5 mm for all the angles, does describe better than a plane the projected light, with errors from 1 mm up to 2.5 mm.

Using the laser projection ray model from Chapter 3 and Chapter 4, the limits of the elliptical cone model are analyzed. In this case 171 laser rays (see Fig. 7.5, Laser ray) are sampled across a laser aperture of 175° for 9 different laser-viewport incidence angles γ varying from -20° to 20°. The intersection between each laser ray α at each incidence angle γ and a projection plane at 0.5 m distance from the viewport is computed. This

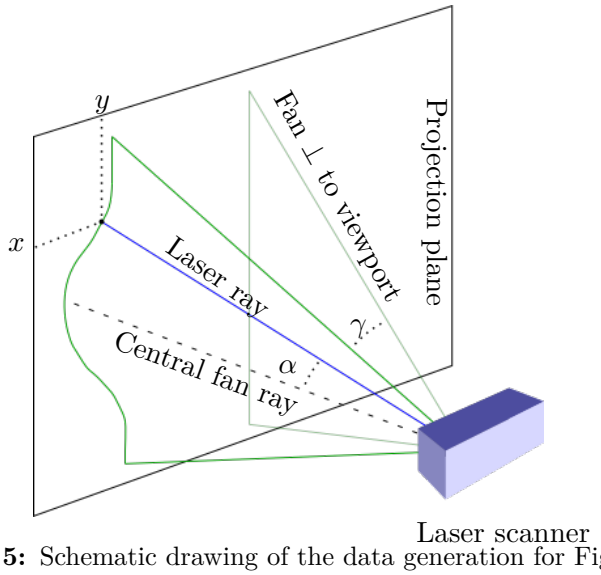

Figure 7.5: Schematic drawing of the data generation for Fig. 7.6.

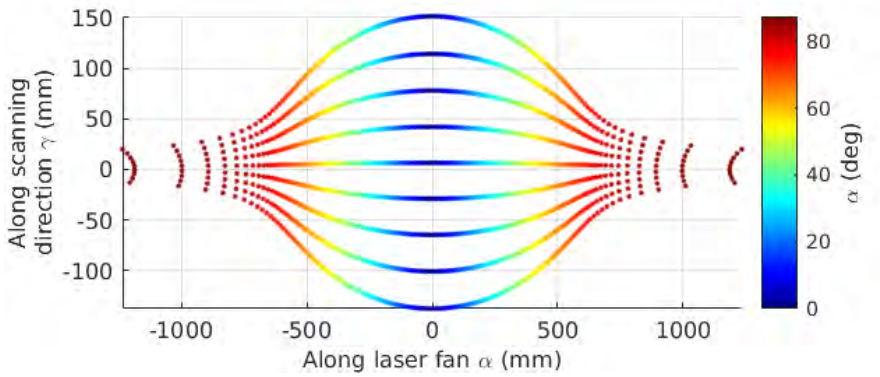

Figure 7.6: Projection of the simulated laser at 0.5 m distance. Each stripe corresponds to the projection of the laser for a specific angle of incidence between the laser and the viewport (in the figure varying from -20° to 20°). Each laser projection is colored according to the angle α of the laser ray.

intersections are plotted into Fig. 7.6 colored with it's α value. This figure presents the curved shape of the laser at 0.5 m distance from the viewport for the 9 different laser-viewport incidence angles. There, it can be seen how, the curvature of the projected laser changes as the angle α increases, concluding that the elliptical cone surface would not be able to represent the laser light beyond a certain laser fan aperture. Fig. 7.7 shows the cone fitting error (i.e. final cost of the fitting cone minimization problem from Eq. (30) in Chapter 4) for different laser apertures with a constant incidence angle γ of 20°. There, it can be seen how the error fitting grows with the laser aperture, specially for apertures beyond 80°. This covers most of the commercially available laser line projectors, which have apertures up to 90°. Moreover, when the aperture of the laser increases, the optical density of the projected line decreases making the line detection more challenging. Therefore, using big laser apertures is not recommended, specially underwater where light attenuation is higher than in air. Using bigger fan angles would also force to use a wider lens with the camera, otherwise, some part of the line would not be contained in the images

wasting some of the already decreased optical density of the projected line. Moreover, a wider camera lens would introduce bigger image distortions producing less accurate reconstructions. Finally, a wider lens would also increment the area on the scene covered by each pixel (assuming a fixed resolution for the camera), this would decrease the quality of the laser line sub-pixel detector.

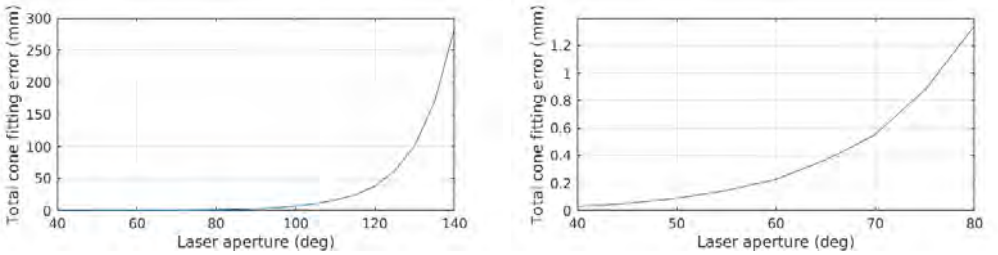

Figure 7.7: Cone fitting error at a 20° incidence angle between the laser plane and the viewport for different laser apertures.

Finally, with the laser scanner calibrated, the ray-based model triangulation and the elliptical cone one were compared. This comparison was done by computing the euclidean distance between all the pairs of 3D points computed using the two triangulation techniques corresponding to the same illuminated pixel. The average distance between points was 0.05 mm with a standard deviation of 0.06 mm. This confirms that the elliptical cone is a good representation of the overall set of light rays. When comparing the triangulation time for a high resolution scan (i.e. the lowest frame rate at which the sensor can scan), the triangulation using the ray triangulation is more than 4 times slower the triangulation time using the elliptical cone: 21 s and 5 s respectively for a full resolution complete scan.

Laser Scanner 3D Reconstructions

To assess the accuracy of the laser scanner using the elliptical cone triangulation we first scanned at different distances (from 0.5 m to 1.2 m) a set of 3 calibrated ceramic gauges (20 mm, 50 mm and 100 mm long) both in air and underwater. In this experiment, the size of the gauge was determined in each scan by manually picking two points on each gauge. From the 29 scans used in this quality assessment the average error was 0.44 mm and 0.98 mm with a standard deviation of 0.35 mm and 0.72 mm in air and underwater respectively. Moreover, with the histogram of the error and the distance to the center of the measured gauge we observed that the error grows more slowly with the distance in air than underwater. In the same way, a triangular prism was scanned 10 times at different positions from the scanner to assess the accuracy in the measurement of angles. For this experiment the prism was positioned in a way that the two faces defining one of the angles were always clearly visible from the scanner. In this set up we measured not only the angle but also the distance of the opposite edge. The average error for the 10 scans was 0.072° with an standard deviation of 0.015° while the edge measurement error was 0.53 mm with a standard deviation of 0.27 mm.

Although these results are good, they do not express how well the overall shape of an object is reconstructed. To assess this, a second experiment was performed where a 3D printed propeller of 100 mm diameter was scanned at an approximate distance of 65 cm both in air and underwater. The points from the scan that belong to the propeller were manually selected and the original CAD model was aligned using Iterative Closest Point

(ICP). Then, the distance between each point and the CAD model was computed. In both cases, air and underwater, the average error was well below one millimeter being the in air reconstruction slightly better than the underwater one. Moreover, the maximum error was just above 1 millimeter in both cases (1.17 mm in air and 1.19 mm underwater).

The last accuracy experiment consisted on scanning a flat surface at different distances. To assess the reconstruction error, the best fitting plane was computed for each scan and the error was defined as the distance from each point to this plane. This experiment shows smaller errors when the planes are scanned in air than when they are underwater and the error evolves with the distance from less than one millimeter at short scanning distance, up to 2.53 mm in air and 4.39 mm underwater at longer distances. Moreover, we studied what the source of these errors could be by using the synthetic model of the scanner and slightly changing some of the parameters. When comparing the in air deformations to the synthetic expected deformations from the model we can see how it is potentially similar to a combination of a bad estimate of the camera distortion as well as a bad estimate of the laser position. In contrast, underwater deformations appear to be mainly driven by a bad estimate of the normal of the laser viewport.

Finally, Fig. 7.8 presents the distortion that appears when using a plane to represent the laser light underwater. In this experiment, the scanner was used to scan an approximately flat water tank wall. Comparing Fig. 7.8a, computed using planes for triangulation, with Fig. 7.8b, computed using cones for triangulation, it is clear that the cone reconstruction describes more accurately the reality because in the case of Fig. 7.8a the water tank wall appears completely bent.

7.2.2 SLAM

This experiment consisted on mapping an underwater pipe and valve structure in the CIRS water tank at a distance between 2 and 3.5 m. The experiment was done with the Girona 500 AUV and the laser scanner mounted in its payload area looking forward and approximately 45° down. The AUV was teleoperated around the structure and kept approximately static (keeping position with a zero velocity control) while each scan of the map was gathered in order to minimize the deformation of the 3D point clouds. The results show how the AUV drift accumulated in the mission produces a non-consistent map when using the DR navigation. In contrast, using the EKF SLAM proposed in Chapter 5 as the navigation solution, the map appears much more consistent. The two produced maps can be evaluated with the #Cells statistic as we have previously done in Section 7.1. In this case, the SLAM produced map occupies 5062 cells which is an 18.77% less than in the DR map (6232 cells).

7.2.3 Manipulation

The laser scanner was also applied to underwater manipulation tasks. Two different manipulation applications were tested were the system was used to retrieve the 3D of the workspace (i.e. the structure and the amphora for each respective experiment). The first experiment was done with a fixed-based 8 DoF manipulator working in the water tank of OSL at Heriot Watt University. In the experiment, the manipulator was moving cyclically through 3 way-points in a working area with unknown fixed obstacles. Using MoveIt! [122] and the RRT-connect algorithm [123] available in the Open Motion Planning Library (OMPL), a path was computed between the current position and the next way-point. To

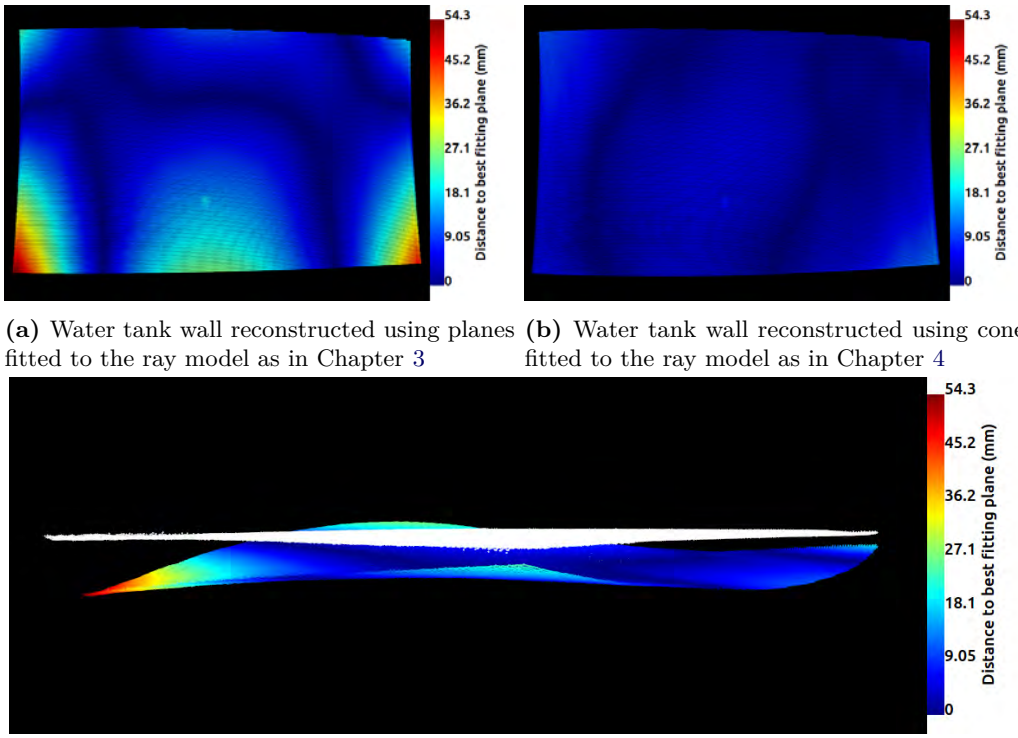

(a) Water tank wall reconstructed using planes fitted to the ray model as in Chapter 3

(b) Water tank wall reconstructed using cones fitted to the ray model as in Chapter 4

(c) Comparison of the two reconstructed water tank walls. In white, the one corresponding to elliptical cone triangulation. In color, the one corresponding to the plane triangulation.

Figure 7.8: Water tank wall scanned using triangulation using plane and cone triangulation. The point clouds are colored with the distance to the best fitting plane of the cloud.

ensure that the robot does not collide to any of the present objects the trajectory was planned in the free space of an occupancy map. This map was empty at the beginning of the experiment and was constantly updated with the new data coming from the laser scanner. When a potential collision between the computed trajectory and an obstacle mapped after the planning was detected, the robot stopped and a re-planned. The results show how the robot was able to move from way-point to way-point three times without colliding with the environment. Moreover, the first planned trajectory is stopped and re-planned because it was colliding with a newly discovered object.

In the second experiment, the ECA/CSIP Light-Weight ARM 5E was mounted on Girona 500 AUV to pick up an amphora at the bottom of the water tank. In this experiment, the grasping pose was computed every time a new point cloud was provided by the laser scanner. During this experiment, the amphora was located also with artificial landmarks used to compute its position with state of the art computer vision techniques. The results show how the position of the computed amphora using the markers and the point cloud are consistent, allowing the manipulator system to grasp the amphora.

8

Conclusions and Future Work

This chapter concludes this thesis by reviewing the main conclusions and the achieved objectives in Section 8.1 and proposing some research lines for future work in Section 8.2.

8.1 Conclusions and Contributions

This thesis has extended the state of the art presenting two methods for 3D underwater SLAM using range sensors: a multibeam echosounder and a laser scanner. The objectives formulated in Chapter 1 have been successfully completed as shown in the following paragraphs.

Underwater 3D SLAM using a multibeam echosounder A Method for doing 3D SLAM underwater using a multibeam echosounder has been presented, implemented and validated experimentally. The conclusions and contributions of to this part of the work follow:

Probabilistic Registration: We have presented a full 3D probabilistic registration framework by extending the previously presented one. This algorithm is an ICP method with point-to-point association for coarse registration and point-to-plane association for fine registration. To decrease the computation time as well as to reduce the potential to fall in local minimums, the two registered surfaces are sub-sampled. Moreover, the complexity of the association step of the ICP is reduced from $O(n^2)$ to $O(n)$ using the presented heuristic based in the probabilistic representation of the points.

SLAM framework: We developed a full SLAM framework to estimate the robot trajectory and correct it by incorporating the results of the probabilistic registration.

Experimental Validation: The proposed method has been extensively demonstrated using data collected in field experiments performed with GIRONA 500 AUV (Sant Feliu, Porto Pim and Santorini datasets) as well as with the Tasmania dataset kindly provided by the ACFR researchers. In all cases the maps produced using the proposed algorithm are more consistent than the ones obtained with DR navigation. When USBL data was available, results were also compared with maps including absolute positioning, showing a consistency close to them.

Contributions: The preliminary version of the algorithm was published in [2] using the Tasmania dataset. Then, different subsampling criterias are presented in [8, 9] using the Santorini and Tasmania datasets respectively. Finally, the complete version of the systems was reported in [20] using the Tasmania and Sant Feliu de Guíxols datasets. The results using the Porto Pim datasets have not been presented in any publication.

Underwater Laser Scanner A novel real-time laser scanner able to gather variable-resolution/speed 3D point clouds of a subsea scene has been designed, modeled, calibrated and applied to inspection/mapping as well as to intervention applications. Hereafter, the conclusions and contributions related to this part are detailed.

Ray distortion model: We have developed a model that represents the rays of light in the projection side of the laser scanner. Moreover, we have proposed to use an elliptical cone to represent the set of refracted rays in the underwater media after passing through a flat viewport. This speeds up the triangulation time while keeping the accuracy when compared to the ray-based model.

Moreover, the elliptical model cone better describes the projected light than the state of the art methods using a plane surface. Finally, we have studied the limits of the elliptical cone model demonstrating that it holds for most of the laser aperture angles commercially available.

Sensor Model and Calibration: We have developed a full model for the underwater laser scanner taking into account the refraction of the light in both the emission side as well as the receiving side. Moreover, we have proposed a calibration procedure to estimate all the elements of the laser scanner model as well as the elliptical cones to be used in real-time 3D estimation. The sensor model together with the calibration procedure developed allowed us to use the underwater laser scanner as a real-time 3D perception sensor with sub-millimetric accuracy.

Point Cloud 3D SLAM: The underwater laser scanner developed has been used to correct the navigational drift of the Girona 500 AUV using a SLAM framework. These experiments were done by inspecting an underwater pipe and valve structure and have a potential application to IMR tasks.

3D Perception for Intervention: The developed underwater laser scanner has been used in conjunction with 2 different underwater manipulators in 2 different manipulation tasks. The first one using an 8 DoF fixed-base manipulator to move around an environment with unknown obstacles without colliding, and the second one, to estimate the position of an amphora to grasp it with a UVMS.

Contributions: A patent for the proposed laser scaner has been filed [10]. The ray projection model of the system is reported in [7] together with the experiments proving that the elliptical cone representation is better than the plane to represent the projected laser light. The sensor model and calibration procedure are presented in [4]. Finally the two applications are presented in [5] (point cloud 3D SLAM) and [6] (3D perception for intervention).

8.2 Future work

This thesis can not be considered a final and definitive solution to underwater 3D SLAM using sonars and laser sensor. However, this work does contribute to step towards better and more capable AUVs. In this way, we established the basis for the future work to continue extending the capabilities of AUVs:

Underwater multibeam 3D SLAM: The future work regarding this SLAM framework will have to focus in corrected the internal patch error that the robot drift introduces to each sub-map. Moreover, if the parameters of the algorithm are not chosen appropriately, the computational cost of the algorithm does not allow for on-line usage. In this way, future research will have to tackle the on-line formulation of multibeam 3D SLAM. Finally, explore the use of pose-based graph optimization techniques that have been replacing EKF SLAM in the past years [71, 124, 125, 126].

Underwater laser line scanner: Future work in the underwater laser scanner field will have to tackle mainly the sensor's error in the planarity of surfaces as well as to correct the distortion of the point cloud produced by the motion of the vehicle while gathering a scan. The first can be addressed by improving the currently

presented calibration procedure. One example could be to incorporate planarity restrictions in the different minimization problems during the different calibration steps. Regarding the distortion produced by the motion of the sensor, it can be minimized by increasing the scanning frame rate or by incorporating data from navigation sensors at high enough frequency so that the motion is estimated for each scanned line. Moreover, a deep extensive and systematic analysis of the effects of bad estimations of the sensor model parameters is necessary to better assess misscalibrations in further details. Another very important future work will focus in studying the sensor's error induced by the viewport deformation at depth. First analyzing the deformations of the viewport using finite elements analysis to get the deformed viewports shapes and the ray triangulation model and then, by testing the sensor at depth scanning known objects. Finally, studying possible surfaces that better represent the laser light than the elliptical cone for big laser apertures is a must if a wide angle laser scanner is designed.

The future work in SLAM framework using the underwater laser scanner includes testing if some of the non-rigid registration algorithms present in the literature [127] could potentially be used to correct the internal error of the scan produced by the motion of the sensor. In the same way, the use of pose-based graph optimization techniques should be explored for the inspection and mapping problems. Moreover, In the manipulation domain, the future work will focus on object recognition and pose estimation using 3D point clouds in order to push the autonomy of the manipulation tasks.

A

Line-Cone Intersection

This appendix specifies the steps to solve Eq. (14) (i.e. obtain Eq. (15)) in Chapter 4. Given the elliptical cone equation:

$$\boldsymbol{c}(h,\beta) = \begin{bmatrix} a\ h\ \cos(\beta) \\ b\ h\ \sin(\beta) \\ h \end{bmatrix} \tag{A.1}$$

being a and b the scale factors of the unit circle for the x and y directions, and the parametric line equation:

$$\boldsymbol{r}(\lambda) = \lambda \begin{bmatrix} v_x \\ v_y \\ v_z \end{bmatrix} + \begin{bmatrix} o_x \\ o_y \\ o_z \end{bmatrix} \tag{A.2}$$

being $\boldsymbol{v} = (v_x, v_y, v_z)^T$ the line direction vector and $\boldsymbol{p} = (o_x, o_y, o_z)^T$ a point on the line. It is possible to find the intersection, if it exist, by solving the following system of equations:

$$\boldsymbol{r}(\lambda) = \boldsymbol{c}(h,\beta) \rightarrow \lambda \begin{bmatrix} v_x \\ v_y \\ v_z \end{bmatrix} + \begin{bmatrix} o_x \\ o_y \\ o_z \end{bmatrix} = \begin{bmatrix} a\ h\ \cos(\beta) \\ b\ h\ \sin(\beta) \\ h \end{bmatrix} \rightarrow \begin{cases} \lambda v_x + o_x = a\ h \cos(\beta) & \text{(A.3a)} \\ \lambda v_y + o_y = a\ h \sin(\beta) & \text{(A.3b)} \\ \lambda v_z + o_z = h & \text{(A.3c)} \end{cases}$$

Eq. (A.3) defines a non-linear system of equations with three unknowns λ, h and β. By solving this system for either λ or h and β the intersection point can be found.
The unkown β can be easily removed from the system of equations by combining Eq. (A.3a) and Eq. (A.3b) and taking into account that $\sin^2(\beta) + \cos^2(\beta) = 1$. Hence, Eq. (A.3a) is rearenged:

$$(v_x\lambda + o_x)^2 = (ah\cos(\beta))^2 \tag{A.4}$$

$$(v_x\lambda)^2 + (o_x)^2 + 2v_x\lambda o_x = a^2h^2\cos^2(\beta) \tag{A.5}$$

In the same way, Eq. (A.3b) is rearenged:

$$\frac{a}{b}v_y\lambda + \frac{a}{b}o_y = \frac{a}{b}bh\sin(\beta) \tag{A.6}$$

$$\frac{a}{b}v_y\lambda + \frac{a}{b}o_y = ah\sin(\beta) \tag{A.7}$$

$$\left(\frac{a}{b}v_y\lambda + \frac{a}{b}o_y\right)^2 = (ah\sin(\beta))^2 \tag{A.8}$$

$$\left(\frac{a}{b}v_y\lambda\right)^2 + \left(\frac{a}{b}o_y\right)^2 + 2\frac{a^2}{b^2}v_yo_y\lambda = a^2h^2\sin^2(\beta) \tag{A.9}$$

Adding Eq. (A.5) and Eq. (A.9):

$$(v_x\lambda)^2 + (o_x)^2 + 2v_x\lambda o_x + \left(\frac{a}{b}v_y\lambda\right)^2 + \left(\frac{a}{b}o_y\right)^2 + 2\frac{a^2}{b^2}v_yo_y\lambda = a^2h^2\cos^2(\beta) + a^2h^2\sin^2(\beta) \tag{A.10}$$

$$(v_x\lambda)^2 + (o_x)^2 + 2v_x\lambda o_x + \left(\frac{a}{b}v_y\lambda\right)^2 + \left(\frac{a}{b}o_y\right)^2 + 2\frac{a^2}{b^2}v_yo_y\lambda = a^2h^2\left(\cos^2(\beta) + \sin^2(\beta)\right) \tag{A.11}$$

$$(v_x\lambda)^2 + (o_x)^2 + 2v_x\lambda o_x + \left(\frac{a}{b}v_y\lambda\right)^2 + \left(\frac{a}{b}o_y\right)^2 + 2\frac{a^2}{b^2}v_yo_y\lambda = a^2h^2 \tag{A.12}$$

$$b^2v_x^2\lambda^2 + b^2o_x^2 + 2b^2v_x\lambda o_x + a^2v_y^2\lambda^2 + a^2o_y^2 + 2a^2v_yo_y\lambda = a^2b^2h^2 \tag{A.13}$$

$$\lambda^2\left(b^2v_x^2 + a^2v_y^2\right) + \lambda\left(2b^2v_xo_x + 2a^2v_yo_y\right) + \left(b^2o_x^2 + a^2o_y^2\right) = a^2b^2h^2 \tag{A.14}$$

Incorporating Eq. (A.3c) into Eq. (A.14), it is possible to remove the unknown h:

$$\lambda^2\left(b^2v_x^2 + a^2v_y^2\right) + \lambda\left(2b^2v_xo_x + 2a^2v_yo_y\right) + \left(b^2o_x^2 + a^2o_y^2\right) = a^2b^2\left(v_z\lambda + o_z\right)^2 \tag{A.15}$$

Hence, we can solve this equation for the unkown λ:

$$\lambda^2\left(b^2v_x^2 + a^2v_y^2\right) + \lambda\left(2b^2v_xo_x + 2a^2v_yo_y\right) + \left(b^2o_x^2 + a^2o_y^2\right) = a^2b^2\left(v_z^2\lambda^2 + o_z^2 + 2v_zo_z\lambda\right) \tag{A.16}$$

$$\lambda^2\left(b^2v_x^2 + a^2v_y^2\right) + \lambda\left(2b^2v_xo_x + 2a^2v_yo_y\right) + \left(b^2o_x^2 + a^2o_y^2\right) = a^2b^2v_z^2\lambda^2 + a^2b^2o_z^2 + a^2b^2 2v_zo_z\lambda \tag{A.17}$$

which can be rearenged into a standard second degree equation:

$$\lambda^2\left(b^2v_x^2 + a^2v_y^2 - a^2b^2v_z^2\right) + \lambda 2\left(b^2v_xo_x + a^2v_yo_y - a^2b^2v_zo_z\right) + \left(b^2o_x^2 + a^2o_y^2 - a^2b^2o_z^2\right) = 0 \tag{A.18}$$

Bibliography

[1] **Albert Palomer**, Pere Ridao, and David Ribas. "Multibeam 3D Underwater SLAM with Probabilistic Registration". In: *Sensors* 16.4 (2016). DOI: 10.3390/s16040560 (cited on pages ix, 11, 12, 17, 71).

[2] Simone Zandara, Pere Ridao, David Ribas, Angelos Mallios, and **Albert Palomer**. "Probabilistic Surface Matching for Bathymetry Based SLAM". In: *Proceedings of the IEEE International Conference on Robotics and Automation*. 2013 (cited on pages ix, xi, 11, 120).

[3] Chris Roman and Hanumant Singh. "Consistency based error evaluation for deep sea bathymetric mapping with robotic vehicles". In: *IEEE International Conference on Robotics and Automation*. May. Ieee, 2006, pages 3568–3574. DOI: 10.1109/ROBOT.2006.1642247 (cited on pages ix, 108).

[4] **Albert Palomer**, Pere Ridao, Josep Forest, and David Ribas. "Underwater Laser Scanner: Ray-based Model and Calibration". Submitted to IEEE/ASME Transactions on Mechatronics on November 2017 (cited on pages ix, 12, 59, 114, 121).

[5] **Albert Palomer**, Pere Ridao, and David Ribas. "Inspection of an Underwater Structure using Point Cloud SLAM with an AUV and a Laser Scanner". Submitted to Journal of Field Robotics on July 2018. 2018 (cited on pages x, 12, 71, 114, 121).

[6] **Albert Palomer**, Pere Ridao, Dina Youakim, David Ribas, Josep Forest, and Yvan Petillot. "3D Laser Scanner for Underwater Manipulation." In: *Sensors* 18.4 (2018), pages 1–14. DOI: 10.3390/s18041086 (cited on pages x, 13, 87, 108, 114, 121).

[7] **Albert Palomer**, Pere Ridao, David Ribas, and Josep Forest. "Underwater 3D laser scanners: The deformation of the plane". In: *Sensing and Control for Autonomous Vehicles: Applications to Land, Water and Air Vehicles*. Edited by Thor I. Fossen, Kristin Y. Pettersen, and Henk Nijmeijer. Volume 474. Springer International Publishing, 2017, pages 73–88. DOI: 10.1007/978-3-319-55372-6_4 (cited on pages x, 12, 41, 59, 114, 121).

[8] **Albert Palomer**, Pere Ridao, David Ribas, Angelos Mallios, Nuno Gracias, and Guillem Vallicrosa. "Bathymetry-Based SLAM with Difference of Normals Point-Cloud Subsampling and Probabilistic ICP Registration". In: *Proceedings of the IEEE OCEANS 2013 conference*. 2013. DOI: 10.1109/OCEANS-Bergen.2013.6608091 (cited on pages xi, 120).

[9] **Albert Palomer**, Pere Ridao, David Ribas, Angelos Mallios, and Guillem Vallicrosa. "Octree-Based Subsampling Criteria for Bathymetric SLAM". In: *Proceedings of the XXXV Jornadas de Automática* (2014), pages 1–6 (cited on pages xi, 120).

[10] **Albert Palomer**, David Ribas, Pere Rodríguez, and Josep Forest. "Conjunto de Escaneo por Láser, Vehículo y Procedimiento de Escaneo por Láser Correspondientes". P201730372. Mar. 2017 (cited on pages xi, 121).

[11] **Albert Palomer**, Pere Ridao, David Ribas, Angelos Mallios, and Guillem Vallicrosa. "A comparison of G2o graph SLAM and EKF pose based SLAM with bathymetry grids". In: *IFAC Proceedings Volumes (IFAC-PapersOnline)*. Volume 9. PART 1. 2013. DOI: 10.3182/20130918-4-JP-3022.00065 (cited on page xi).

[12] Nuno Gracias, Pere Ridao, Rafael Garcia, Javier Escartin, Franca Cibecchini, Ricard Campos, Marc Carreras, David Ribas, Lluis Magi, **Albert Palomer**, Tudor Nicosevici, Ricard Prados, Laszlo Neumann, Francesco De Filippo, and Angelos Mallios. "Mapping the Moon: Using a lightweight AUV to survey the site of the 17th Century ship 'La Lune'". In: *Proceedings of the MTS/IEEE OCEANS conference*. 2013 (cited on pages xii, 9, 15).

[13] Guillem Vallicrosa, **Albert Palomer**, David Ribas, and Pere Ridao. "Realtime AUV Terrain Based Navigation with Octomap". In: *XXXIV Jornadas de Automática*. Universitat de Girona (UdG). 2013 (cited on page xii).

[14] Guillem Vallicrosa, **Albert Palomer**, David Ribas, and Pere Ridao. "Realtime AUV Terrain Based Navigation with Octomap in a natural environment". In: *ROBOT 2013: First Iberian Robotics Conference*. 2013, pages 41–53 (cited on page xii).

[15] Guillem Vallicrosa, **Albert Palomer**, David Ribas, and Pere Ridao. "Towards Realtime AUV SLAM with Occupancy Grids". In: *Fifth International Workshop on Marine Technology (MARTECH)*. 2013 (cited on page xii).

[16] Enric Galceran, Sharad Nagappa, Marc Carreras, Pere Ridao, and **Albert Palomer**. "Uncertainty-driven Survey Path Planning for Bathymetric Mapping". In: *IEEE/RSJ International Conference on Intelligent Robots and Systems*. Tokyo Big Sight, Japan, 2013, pages 6006–6012. DOI: 10.1109/IROS.2013.6697228 (cited on page xii).

[17] Guillem Vallicrosa, Pere Ridao, David Ribas, and **Albert Palomer**. "Active Range-Only Beacon Localization for AUV Homing". In: *IEEE International Conference on Intelligent Robots and Systems ICRA*. Chicago, IL, USA, 2014, pages 2286–2291 (cited on page xii).

[18] Guillem Vallicrosa, **Albert Palomer**, David Ribas, and Pere Ridao. *Realtime AUV terrain based navigation with octomap in a natural environment*. Volume 252. 2014. DOI: 10.1007/978-3-319-03413-3_4 (cited on pages xii, 9).

[19] Narcís Palomeres, Antonio Peñalver, Miquel Massot-Campos, Guillem Vallicrosa, Pep Lluís P.L. Negre, J.J. Javier Fernández, Pere Ridao, Pedro J. P.J. Sanz, Gabriel Oliver, and **Albert Palomer**. "I-AUV Docking and Intervention in a Subsea Panel". In: *IEEE International Conference on Intelligent Robots and Systems (IROS)*. 2014, pages 2279–2285. DOI: 10.1109/IROS.2014.6942870 (cited on page xii).

[20] **Albert Palomer**, Pere Ridao, David Ribas, and Guillem Vallicrosa. "Multi-beam Terrain / Object Classification for Underwater Navigation Correction". In: *MTS/IEEE OCEANS*. Genova, 2015. DOI: 10.1109/OCEANS-Genova.2015.7271587 (cited on pages xii, 120).

[21] Ricard Campos, Nuno Gracias, **Albert Palomer**, and Pere Ridao. "Global Alignment of a Multiple-Robot Photomosaic using Opto-Acoustic Constraints". In: *NGCUV2015 Girona*. Volume 48. 2. Elsevier Ltd., 2015, pages 20–25. DOI: 10.1016/j.ifacol.2015.06.004 (cited on pages xii, 10).

[22] National Oceanic and Atmospheric Administration (NOAA), U.S. Department of Commerce. *Oceans & Coasts*. http://www.noaa.gov/oceans-coasts. [Online; accessed 3-July-2018]. 2018 (cited on page 8).

[23] Richard Camilli, Paraskevi Nomikou, Javier Escartín, Pere Ridao, Angelos Mallios, Stephanos P. Kilias, Ariadne Argyraki, Muriel Andreani, Valerie Ballu, Ricard Campos, Christine Deplus, Taoufic Gabsi, Rafael Garcia, Nuno Gracias, Natàlia Hurtós, Lluis Magí, Catherine Mével, Manuel Moreira, Narcís Palomeras, Olivier Pot, David Ribas, Lorraine Ruzié, and Dimitris Sakellariou. "The Kallisti Limnes, carbon dioxide-accumulating subsea pools". In: *Scientific Reports* 5 (2015), pages 1–9. DOI: 10.1038/srep12152 (cited on pages 8, 109).

[24] J. Escartín, R. García, O. Delaunoy, J. Ferrer, N. Gracias, A. Elibol, X. Cufi, L. Neumann, D. J. Fornari, S. E. Humphris, and J. Renard. "Globally aligned photomosaic of the Lucky Strike hydrothermal vent field (Mid-Atlantic Ridge, 37°18.5'N): Release of georeferenced data, mosaic construction, and viewing software". In: *Geochemistry, Geophysics, Geosystems* 9.12 (2008), pages 1–17. DOI: 10.1029/2008GC002204 (cited on page 8).

[25] Hanumant Singh, Jonathan Howland, and Oscar Pizarro. "Advances in large-area photomosaicking underwater". In: *IEEE Journal of Oceanic Engineering* 29.3 (2004), pages 872–886. DOI: 10.1109/JOE.2004.831619 (cited on pages 8, 10).

[26] Brian Bingham, Brendan Foley, Hanumant Singh, Richard Camilli, Katerina Delaporta, Ryan Eustice, Angelos Mallios, David Mindell, Chris Roman, and Dimitris Sakellariou. "Robotic Tools for Deep Water Archaeology: Surveying an Ancient Shipwreck with an Autonomous Underwater Vehicle". In: *J. Field Robotics* 27.6 (2010), pages 702–717. DOI: 10.1002/rob (cited on page 8).

[27] Armagan Elibol, Nuno Gracias, Rafael Garcia, Art Gleason, and Brooke Gintert. "Efficient autonomous image mosaicing with applications to coral reef monitoring". In: *Proceedings of theWorkshop on Robotics for Environmental Monitoring held at IEEE/RSJ IROS*. 2011 (cited on page 8).

[28] a. C. R. Gleason, D. Lirman, N. Gracias, T. Moore, S. Griffin, M. Gonzales, B. Gintert, and P. Reid. "Damage Assessment of Vessel Grounding Injuries on Coral Reef Habitats Using Underwater Landscape Mosaics". In: *Proceedings of the 63rd Gulf and Caribbean Fishereies Insitute* April 2016 (2011), pages 126–129. DOI: 10.4319/lom.2010.8.88 (cited on page 8).

[29] Pere Ridao, Marc Carreras, David Ribas, and Rafael Garcia. "Visual Inspection of Hydroelectric Dams Using an Autonomous Underwater Vehicle". In: *Journal of Field Robotics* 27.6 (2010), pages 759–778. DOI: 10.1002/rob (cited on pages 8, 15).

[30] Ingrid Schjølberg, Tor B. Gjersvik, Aksel A. Transeth, and Ingrid B. Utne. "Next Generation Subsea Inspection, Maintenance and Repair Operations". In: *IFAC-PapersOnLine* 49.23 (2016), pages 434–439. DOI: 10.1016/j.ifacol.2016.10.443 (cited on page 8).

[31] Ehrlich Desa, R Madhan, and P Maurya. "Potential of autonomous underwater vehicles as new generation ocean data plaforms". In: *Current Science* 90.9 (2006), pages 1202–1209. DOI: 10.2307/24092021 (cited on page 8).

[32] G.T. Reader, J. Potter, and J.G. Hawley. "The evolution of AUV power systems". In: *Oceans '02 Mts/Ieee* 1 (2002), pages 191–198. DOI: 10.1109/OCEANS.2002.1193270 (cited on page 8).

[33] Lee Freitag, Matthew Grund, Sandipa Singh, James Partan, Peter Koski, and Keenan Ball. "The WHOI Micro-Modem: An acoustic communications and navigation system for multiple platforms". In: *Proceedings of MTS/IEEE OCEANS, 2005* 2005 (2005). DOI: 10.1109/OCEANS.2005.1639901 (cited on page 8).

[34] Sandra Sendra, Jaime Lloret, Jose Miguel Jimenez, and Lorena Parra. "Underwater Acoustic Modems". In: *IEEE Sensors Journal* 16.11 (2016), pages 4063–4071. DOI: 10.1109/JSEN.2015.2434890 (cited on page 8).

[35] N. Farr, A. D. Chave, L. Freitag, J. Preisig, S. N. White, D. Yoerger, and F. Sonnichsen. "Optical modem technology for seafloor observatories". In: *Oceans 2006* (2006), pages 1–7. DOI: 10.1109/OCEANS.2006.306806 (cited on page 8).

[36] Clifford Pontbriand, Norm Farr, Johanna Hansen, James C. Kinsey, L.-P. Pelletier, Jonathan Ware, and Dehann Fourie. "Wireless data harvesting using the AUV Sentry and WHOI optical modem". In: *OCEANS 2015 - MTS/IEEE Washington* August (2015), pages 1–6. DOI: 10.23919/OCEANS.2015.7401985 (cited on page 8).

[37] James C. Kinsey, Ryan Eustice, and Louis L. Whitcomb. "A Survey of Underwater Vehicle Navigation: Recent Advances and New Challenges". In: *7th Conference on Manoeuvring and Control of Marine Craft (MCMC'2006)* (2006), pages 1–12 (cited on page 8).

[38] Liam Paull, Sajad Saeedi, Mae Seto, and Howard Li. "AUV Navigation and Localization: A Review". In: *IEEE Journal of Oceanic Engineering* 39.1 (Jan. 2014), pages 131–149. DOI: 10.1109/JOE.2013.2278891 (cited on page 8).

[39] Rafael Garcia, Nuno Gracias, Tudor Nicosevici, Ricard Prados, Natalia Hurtos, Ricard Campos, Javier Escartin, Armagan Elibol, Ramon Hegedus, and Laszlo Neumann. "Exploring the Seafloor with Underwater Robots". In: *Computer Vision in Vehicle Technology* (2017), pages 75–99. DOI: 10.1002/9781118868065.ch4 (cited on page 8).

[40] Enric Galceran and Marc Carreras. "A survey on coverage path planning for robotics". In: *Robotics and Autonomous Systems* 61.12 (2013), pages 1258–1276. DOI: 10.1016/j.robot.2013.09.004 (cited on page 8).

[41] Dina Youakim and Pere Ridao. "Motion planning survey for autonomous mobile manipulators underwater manipulator case study". In: *Robotics and Autonomous Systems* 107 (2018), pages 20–44. DOI: 10.1016/j.robot.2018.05.006 (cited on page 8).

[42] Pere Ridao, Marc Carreras, David Ribas, Pedro J. Sanz, and Gabriel Oliver. "Intervention AUVs: The next challenge". In: *Annual Reviews in Control* 40 (2015), pages 227–241. DOI: 10.1016/j.arcontrol.2015.09.015 (cited on page 8).

[43] Robert Panish and Mikell Taylor. "Achieving high navigation accuracy using inertial navigation systems in autonomous underwater vehicles". In: *Proceedings of the MTS/IEEE Oceans*. IEEE, June 2011, pages 1–7. DOI: 10.1109/Oceans-Spain.2011.6003517 (cited on page 8).

[44] James C Kinsey and Louis L Whitcomb. "Preliminary field experience with the DVLNAV integrated navigation system for oceanographic submersibles". In: *Control Engineering Practice* 12.12 (Dec. 2004), pages 1541–1549. DOI: 10.1016/j.conengprac.2003.12.010 (cited on page 9).

[45] Pedro Batista, Carlos Silvestre, and Paulo Oliveira. "Single Beacon Navigation: Observability Analysis and Filter Design". In: *American Control Conference (ACC)*. 2010, pages 6191–6196 (cited on page 9).

[46] Guillem Vallicrosa and Pere Ridao. "Sum of gaussian single beacon range-only localization for AUV homing". In: *Annual Reviews in Control* 42 (2016), pages 177–187. DOI: 10.1016/j.arcontrol.2016.09.007 (cited on page 9).

[47] Hubert G. Thomas. "GIB Buoys: An Interface Between Space and Depths of the Oceans". In: *Proceedings of the workshop on Autonomous underwater vehicles.* (1998), pages 181–184. DOI: 10.1109/AUV.1998.744453 (cited on page 9).

[48] A. Alcocer, P. Oliveira, and A. Pascoal. "Study and implementation of an EKF GIB-based underwater positioning system". In: *Control Engineering Practice* 15.6 (2007), pages 689–701. DOI: 10.1016/j.conengprac.2006.04.001 (cited on page 9).

[49] Magne Mandt, Kenneth Gade, and Bjorn Jalving. "Integrateing DGPS-USBL position measurements with inertial navigation in the HUGIN 3000 AUV". In: *Proceedings of the 8th Saint Petersburg international Conference on Integrated Navigation Systems* (2001) (cited on page 9).

[50] Sebastian Carreño, Philip Wilson, Pere Ridao, Yvan Petillot, Sebastian Carreno, Philip Wilson, Pere Ridao, and Yvan Petillot. "A survey on Terrain Based Navigation for AUVs". In: *Proceedings of the MTS/IEEE Oceans* (Sept. 2010), pages 1–7. DOI: 10.1109/OCEANS.2010.5664372 (cited on page 9).

[51] José Melo and Aníbal Matos. "Survey on advances on terrain based navigation for autonomous underwater vehicles". In: *Ocean Engineering* 139.May (2017), pages 250–264. DOI: 10.1016/j.oceaneng.2017.04.047 (cited on page 9).

[52] Ricard Campos, Nuno Gracias, and Pere Ridao. "Underwater multi-vehicle trajectory alignment and mapping using acoustic and optical constraints". In: *Sensors* 16.3 (2016). DOI: 10.3390/s16030387 (cited on pages 9, 10, 15).

[53] Chris Roman and Hanumant Singh. "Estimation of Error in Large Area Underwater Photomosaics Using Vehicle Navigation Data". In: *OCEANS, 2001. MTS/IEEE Conference and Exhibition.* 2001, pages 1849–1853. DOI: 10.1109/OCEANS.2001.968127 (cited on page 10).

[54] Y. Marcon, H. Sahling, and G. Bohrmann. "LAPM: a tool for underwater large-area photo-mosaicking". In: *Geoscientific Instrumentation, Methods and Data Systems* 2.2 (2013), pages 189–198. DOI: 10.5194/gi-2-189-2013 (cited on page 10).

[55] S.B. Williams, O.R. Pizarro, M.V. Jakuba, C.R. Johnson, N.S. Barrett, R.C. Babcock, G.a. Kendrick, P.D. Steinberg, A.J. Heyward, P.J. Doherty, I. Mahon, M. Johnson-Roberson, D. Steinberg, and A. Friedman. "Monitoring of Benthic Reference Sites: Using an Autonomous Underwater Vehicle". In: *Robotics and Automation Magazine, IEEE* 19.1 (2012), pages 73–84. DOI: 10.1109/MRA.2011.2181772 (cited on page 10).

[56] Ayoung Kim and Ryan M. Eustice. "Real-Time Visual SLAM for Autonomous Underwater Hull Inspection Using Visual Saliency". In: *IEEE Transactions on Robotics* 29.3 (June 2013), pages 719–733. DOI: 10.1109/TRO.2012.2235699 (cited on page 10).

[57] Klemen Istenič, Viorela Ila, Lukáš Polok, Nuno Gracias, and Rafael García. "Mission-time 3D Reconstruction with Quality Estimation". In: *Oceans 2017*. September. 2017, pages 47–55 (cited on pages 10, 15).

[58] Matthew Johnson-Roberson, Oscar Pizarro, Stefan B Williams, and Ian Mahon. "Generation and Visualization of Large-Scale Three-Dimensional Reconstructions from Underwater Robotic Surveys". In: *Journal of Field Robotics* 27.1 (2010), pages 21–51. DOI: 10.1002/rob (cited on page 10).

[59] James Servos, Michael Smart, and Steven L. Waslander. "Underwater stereo SLAM with refraction correction". In: *IEEE International Conference on Intelligent Robots and Systems* (2013), pages 3350–3355. DOI: 10.1109/IROS.2013.6696833 (cited on page 10).

[60] Pep Lluis Negre, Francisco Bonin-Font, and Gabriel Oliver. "Cluster-based loop closing detection for underwater slam in feature-poor regions". In: *Proceedings - IEEE International Conference on Robotics and Automation* 2016-June (2016), pages 2589–2595. DOI: 10.1109/ICRA.2016.7487416 (cited on page 10).

[61] Murat D Aykin and Shahriar Negahdaripour. "On Feature Matching and Image Registration for Two-dimensional Forward-scan Sonar Imaging". In: *Journal of Field Robotics* 30.4 (2013), pages 602–623. DOI: 10.1002/rob.21461 (cited on page 10).

[62] Natalia Hurtós, David Ribas, Xavier Cufí, Yvan Petillot, and Joaquim Salvi. "Fourier-based Registration for Robust Forward-looking Sonar Mosaicing in Low-visibility Underwater Environments". In: *Journal of Field Robotics* 32.1 (2015), pages 123–151. DOI: 10.1002/rob (cited on pages 10, 15).

[63] Robert N Carpenter. "Concurrent Mapping and Localization with FLS". In: *Autonomous Underwater Vehicles, 1998. AUV'98. Proceedings of the 1998 workshop on1*. Volume 02841. 401. 1998, pages 133–148. DOI: 10.1109/AUV.1998.744449 (cited on page 10).

[64] John J. Leonard, Robert N Carpenter, and Hans Jacob S. Feder. "Stochastic Mapping Using Forward Look Sonar". In: *Robotica* 19.5 (2001), pages 467–480. DOI: 10.1017/S0263574701003411 (cited on page 10).

[65] Stefan B Williams, Paul Newman, J. Rosenbaltt, Gamini Dissanayake, Hugh Durrant-whyte, Julio Rosenblatt, Gamini Dissanayake, and Hugh Durrant-whyte. "Autonomous Underwater Navigation and Control". In: *Robotica* 19 (2001), pages 481–496 (cited on page 10).

[66] David Ribas, Pere Ridao, Juan Domingo Domingo, and José Neira. "Underwater SLAM in Man-Made Structured Environments". In: *Journal of Field Robotics* 25.11-12 (2008), pages 898–921. DOI: 10.1002/rob (cited on pages 10, 15).

[67] Angelos Mallios, Pere Ridao, David Ribas, Marc Carreras, and Richard Camilli. "Toward autonomous exploration in confined underwater environments". In: *Journal of Field Robotics* (2015) (cited on pages 10, 11, 13, 15).

[68] Guillem Vallicrosa and Pere Ridao. "H-SLAM: Rao-Blackwellized Particle Filter SLAM Using Hilbert Maps". In: *Sensors* 18.5 (2018), page 1386. DOI: 10.3390/s18051386 (cited on pages 10, 15).

[69] Chris Roman and Hanumant Singh. "A Self-Consistent Bathymetric Mapping Algorithm". In: *Journal of Field Robotics* 24.1-2 (2007), pages 23–50. DOI: 10.1002/rob (cited on pages 10, 15).

[70] S. Barkby, S. B. Williams, O. Pizarro, and M. V. Jakuba. "Bathymetric particle filter SLAM using trajectory maps". In: *The International Journal of Robotics Research* 31.12 (Sept. 2012), pages 1409–1430. DOI: 10.1177/0278364912459666 (cited on page 10).

[71] James Ian S Vaughn. "Factor graphs and submap simultaneous localization and mapping for microbathymetry". PhD thesis. University of Rhode Island, 2015, page 162 (cited on pages 10, 11, 121).

[72] Heiko Bülow and Andreas Birk. "Spectral registration of noisy sonar data for underwater 3D mapping". In: *Autonomous Robots* 30 (2011), pages 307–331. DOI: 10.1007/s10514-011-9221-8 (cited on page 10).

[73] Nathaniel Fairfield, George Kantor, and David Wettergreen. "Real-Time SLAM with Octree Evidence Grids for Exploration in Underwater Tunnels". In: *Journal of Field Robotics* 24.1-2 (2007), pages 3–21. DOI: 10.1002/rob (cited on page 10).

[74] Emili Hernández, Pere Ridao, David Ribas, and Angelos Mallios. "Probabilistic sonar scan matching for an AUV". In: *Procdeedings of the IEEE/RSJ International Conference on Intelligent Robots and Systems (IROS)* (Oct. 2009), pages 255–260. DOI: 10.1109/IROS.2009.5354656 (cited on pages 11, 13).

[75] Angelos Mallios, Pere Ridao, David Ribas, and Emili Hernández. "Scan Matching SLAM in Underwater Environments". In: *Autonomous Robots* (June 2013). DOI: 10.1007/s10514-013-9345-0 (cited on page 11).

[76] Sundara Tejaswi Digumarti, Gaurav Chaurasia, Aparna Taneja, Roland Siegwart, Amber Thomas, and Paul Beardsley. "Underwater 3D capture using a low-cost commercial depth camera". In: *2016 IEEE Winter Conference on Applications of Computer Vision, WACV 2016*. Volume 1. 2016. DOI: 10.1109/WACV.2016.7477644 (cited on page 11).

[77] Atif Anwer, Syed Saad Azhar Ali, Amjad Khan, and Fabrice Meriaudeau. "Underwater 3-D Scene Reconstruction Using Kinect v2 Based on Physical Models for Refraction and Time of Flight Correction". In: *IEEE Access* 5 (2017), pages 15960–15970. DOI: 10.1109/ACCESS.2017.2733003 (cited on page 11).

[78] Wikipedia contributors. *Electromagnetic absorption by water — Wikipedia, The Free Encyclopedia*. [Online; accessed 8-July-2018]. 2018 (cited on page 11).

[79] F Bruno, G Bianco, M Muzzupappa, S Barone, and A V Razionale. "Experimentation of structured light and stereo vision for underwater 3D reconstruction". In: *ISPRS Journal of Photogrammetry and Remote Sensing* 66 (2011), pages 508–518. DOI: 10.1016/j.isprsjprs.2011.02.009 (cited on page 11).

[80] Gabrielle Inglis, Clara Smart, Ian Vaughn, and Chris Roman. "A pipeline for structured light bathymetric mapping". In: *IEEE/RSJ International Conference on Intelligent Robots and Systems*. 2012, pages 4425–4432 (cited on page 11).

[81] Adrian Bodenmann, Blair Thornton, and Tamaki Ura. "Generation of High-resolution Three-dimensional Reconstructions of the Seafloor in Color using a Single Camera and Structured Light". In: *Journal of Field Robotics* (2016), pages 1–19. DOI: 10.1002/rob.21682 (cited on page 11).

[82] Miquel Massot-Campos, Gabriel Oliver, Adrian Bodenmann, and Blair Thornton. "Submap bathymetric SLAM using structured light in underwater environments". In: *Autonomous Underwater Vehicles 2016, AUV 2016* (2016), pages 181–188. DOI: 10.1109/AUV.2016.7778669 (cited on page 11).

[83] Mario Prats, J. Javier Fernandez, and Pedro J. Sanz. "Combining template tracking and laser peak detection for 3D reconstruction and grasping in underwater environments". In: *IEEE International Conference on Intelligent Robots and Systems* (2012), pages 106–112. DOI: 10.1109/IROS.2012.6385792 (cited on pages 11, 12).

[84] Michael Bleier and Andreas Nüchter. "Low-Cost 3D laser scanning in air or water using self-calibrating structured light". In: *International Archives of the Photogrammetry, Remote Sensing and Spatial Information Sciences - ISPRS Archives* 42.2W3 (2017), pages 105–112. DOI: 10.5194/isprs-archives-XLII-2-W3-105-2017 (cited on page 12).

[85] Miquel Massot-Campos and Gabriel Oliver-Codina. "Underwater Laser-based Structured Light System for one-shot 3D reconstruction". In: *IEEE SENSORS 2014 Proceedings* (2014), pages 1138–1141. DOI: 10.1109/ICSENS.2014.6985208 (cited on page 12).

[86] Marc Hildebrandt, Jochen Kerdels, Jan Albiez, and Frank Kirchner. "A practical underwater 3D-Laserscanner". In: *Oceans 2008* (2008). DOI: 10.1109/OCEANS.2008.5151964 (cited on page 12).

[87] Takeshi Nakatani, Shuhao Li, Tamaki Ura, Adrian Bodenmann, and Takashi Sakamaki. "3D visual modeling of hydrothermal chimneys using a rotary laser scanning system". In: *2011 IEEE Symposium on Underwater Technology, UT'11 and Workshop on Scientific Use of Submarine Cables and Related Technologies, SSC'11* (2011), pages 4–8. DOI: 10.1109/UT.2011.5774140 (cited on page 12).

[88] Michael J. Chantler, James Clark, and Manickan Umasuthan. “Calibration and operation of an underwater laser triangulation sensor: the varying baseline problem”. In: *Optical Engineering* 36.9 (1997), page 2604. DOI: 10.1117/1.601500 (cited on page 12).

[89] D.M. Kocak, F.M. Caimi, P.S. Das, and J.A. Karson. “A 3-D laser line scanner for outcrop scale studies of seafloor features”. In: *Proc. of OCEANS Conf.* 3 (1999), pages 1105–1114. DOI: 10.1109/OCEANS.1999.800144 (cited on page 12).

[90] Shukai Chi, Zexiao Xie, and Wenzhu Chen. “A Laser Line auto-scanning system for underwater 3D reconstruction”. In: *Sensors* 16.9 (2016). DOI: 10.3390/s16091534 (cited on page 12).

[91] Tali Treibitz, Yoav Y. Schechner, Clayton Kunz, and Hanumant Singh. “Flat refractive geometry”. In: *IEEE Transactions on Pattern Analysis and Machine Intelligence* 34.1 (2012), pages 51–65. DOI: 10.1109/TPAMI.2011.105 (cited on page 12).

[92] Angelos Mallios, Pere Ridao, David Ribas, F Maurelli, and Yvan Petillot. “EKF-SLAM for AUV navigation under probabilistic sonar scan-matching”. In: *IEEE/RSJ International Conference on Intelligent Robots and Systems*. Ieee, Oct. 2010, pages 4404–4411. DOI: 10.1109/IROS.2010.5649246 (cited on page 13).

[93] J. Amat, A. Monferrer, J. Batlle, and X. Cufí. “GARBI: A low-cost underwater vehicle”. In: *Microprocessors and Microsystems* 23.2 (1999), pages 61–67. DOI: 10.1016/S0141-9331(99)00013-7 (cited on page 14).

[94] J. Batlle, P. Ridao, R. García, M. Carreras, X. Cufí, A. El-Fakdi, D. Ribas, T. Nicosevici, E. Batlle, G. Oliver, A. Ortiz, and J. Antich. “URIS : Underwater Robotic Intelligent System”. In: *Automation for the Maritime Industries* 1 (2004), pages 177–203 (cited on page 14).

[95] D. Ribas, N. Palomeras, P. Ridao, M. Carreras, and E. Hernàndez. “ICTINEUAUV wins the first SAUC-E competition”. In: *Proceedings - IEEE International Conference on Robotics and Automation* April (2007), pages 151–156. DOI: 10.1109/ROBOT.2007.363779 (cited on page 14).

[96] *SAUC-E: Student AUV Challange Europe*. http://sauc-europe.org/about.html. [Online; accessed 13-July-2018]. 2018 (cited on page 14).

[97] David Ribas, Narcís Palomeras, Pere Ridao, Marc Carreras, and Angelos Mallios. “Girona 500 AUV: From Survey to Intervention”. In: *IEEE/ASME Transactions on Mechatronics* 17.1 (Feb. 2012), pages 46–53. DOI: 10.1109/TMECH.2011.2174065 (cited on page 14).

[98] IQUA Robotis S.L. *IQUA Robotics - AUVs that fit your needs*. http://iquarobotics.com/. [Online; accessed 13-July-2018]. 2018 (cited on page 14).

[99] M Carreras, C Candela, D Ribas, A Mallios, L Magí, E Vidal, N Palomeras, and P Ridao. “Sparus II, design of a lightweight hovering AUV”. In: *Proceedings of the 5th international workshop on marine technology. Martech’13*. 2013, pages 152–155 (cited on page 14).

[100] Marc Carreras, Juan David Hernandez, Eduard Vidal, Narcis Palomeras, David Ribas, and Pere Ridao. "Sparus II AUV - A Hovering Vehicle for Seabed Inspection". In: *IEEE Journal of Oceanic Engineering* 43.2 (2018), pages 344–355. DOI: 10.1109/JOE.2018.2792278 (cited on page 14).

[101] Eurathlon consortium. *Eurathlon — An Outdoor Robotics Challange for Land, Sea and Air*. https://www.eurathlon.eu/. [Online; accessed 13-July-2018]. 2018 (cited on page 14).

[102] *European Robotics League*. https://www.eu-robotics.net/robotics_league/index.html. [Online; accessed 13-July-2018]. 2018 (cited on page 14).

[103] Emili Hernández, Marc Carreras, Javier Antich, Pere Ridao, and Alberto Ortiz. "A topologically guided path planner for an AUV using homotopy classes". In: *Proceedings - IEEE International Conference on Robotics and Automation* (2011), pages 2337–2343. DOI: 10.1109/ICRA.2011.5980108 (cited on page 15).

[104] E Galceran. "Coverage Path Planning for Autonomous Underwater Vehicles". PhD thesis. 2014 (cited on page 15).

[105] Juan David Hernández, Klemen Istenič, Nuno Gracias, Narcís Palomeras, Ricard Campos, Eduard Vidal, Rafael García, and Marc Carreras. "Autonomous underwater navigation and optical mapping in unknown natural environments". In: *Sensors* 16.8 (2016). DOI: 10.3390/s16081174 (cited on page 15).

[106] Eduard Vidal, Juan David Hernández, Klemen Istenič, and Marc Carreras. "Online View Planning for Inspecting Unexplored Underwater Structures". In: *IEEE Robotics and Automation Letters* 2.3 (2017), pages 1436–1443. DOI: 10.1109/LRA.2017.2671415 (cited on page 15).

[107] Arnau Carrera, Narcís Palomeras, Natàlia Hurtós, and Marc Carreras. "Free-floating panel intervention by means of learning by demonstration". In: *IFAC Proceedings Volumes (IFAC-PapersOnline)* 48.2 (2015), pages 38–43. DOI: 10.1016/j.ifacol.2015.06.007 (cited on page 15).

[108] Narcís Palomeras, Antonio Peñalver, Miquel Massot-Campos, Guillem Vallicrosa, Pep Lluís P.L. Negre, J.J. Javier Fernández, Pere Ridao, Pedro J. P.J. Sanz, Gabriel Oliver, and **Albert Palomer**. "I-AUV Docking and Intervention in a Subsea Panel". In: *IEEE International Conference on Intelligent Robots and Systems (IROS)*. 2014, pages 2279–2285. DOI: 10.1109/IROS.2014.6942870 (cited on page 15).

[109] Dina Youakim, Pere Ridao, Narcis Palomeras, Francesco Spadafora, David Ribas, and Maurizio Muzzupappa. "MoveIt!: Autonomous Underwater Free-Floating Manipulation". In: *IEEE Robotics and Automation Magazine* 24.3 (2017), pages 41–51. DOI: 10.1109/MRA.2016.2636369 (cited on page 15).

[110] Patryk Cieslak, Pere Ridao, and Mariusz Giergiel. "Autonomous underwater panel operation by GIRONA500 UVMS: A practical approach to autonomous underwater manipulation". In: *Proceedings - IEEE International Conference on Robotics and Automation* 2015-June.June (2015), pages 529–536. DOI: 10.1109/ICRA.2015.7139230 (cited on page 15).

[111] Angelos Mallios. "Sonar Scan Matching for Simultaneous Localization and Mapping in Confined Underwater Environments". PhD thesis. 2014 (cited on page 15).

[112] Josep Bosch, Nuno Gracias, Pere Ridao, and David Ribas. "Omnidirectional Underwater Camera Design and Calibration". In: *Sensors* 15.3 (2015), pages 6033–6065. DOI: 10.3390/s150306033 (cited on page 15).

[113] Josep Bosch, Nuno Gracias, Pere Ridao, Klemen Istenič, and David Ribas. "Close-range tracking of underwater vehicles using light beacons". In: *Sensors* 16.4 (2016), pages 1–26. DOI: 10.3390/s16040429 (cited on page 15).

[114] Codruta O. Ancuti, Cosmin Ancuti, Christophe De Vleeschouwer, Laszlo Neumann, and Rafael Garcia. "Color transfer for underwater dehazing and depth estimation". In: *IEEE International Conference on Image Processing*. 2017, pages 695–699 (cited on page 15).

[115] Ricard Prados, Nuno Gracias, Laszlo Neumann, and Håvard Vågstøl. "Real-time Fish Detection in Trawl Nets". In: *Oceans 2017*. 2017, pages 1–5 (cited on page 15).

[116] M. Prats, J. C. Garcia, S. Wirth, D. Ribas, P. J. Sanz, P. Ridao, N. Gracias, and G. Oliver. "Multipurpose autonomous underwater intervention: A systems integration perspective". In: *2012 20th Mediterranean Conference on Control and Automation, MED 2012 - Conference Proceedings* 03 (2012), pages 1379–1384. DOI: 10.1109/MED.2012.6265831 (cited on page 15).

[117] Chris Roman, Gabrielle Inglis, and James Rutter. "Application of structured light imaging for high resolution mapping of underwater archaeological sites". In: *Oceans'10 Ieee Sydney*. Ieee, May 2010, pages 1–9. DOI: 10.1109/OCEANSSYD.2010.5603672 (cited on page 15).

[118] Chris Roman, Gabrielle Inglis, Ian Vaughn, Clara Smart, Bertrand Douillard, and Stefan Williams. "The Development of High-Resolution Seafloor Mapping Techniques". In: *Oceanography* 25.1 (2012), pages 42–45. DOI: 10.5670/oceanog.2011.supplement.01 (cited on page 15).

[119] Nikolaos Tsiogkas, Valerio De Carolis, and David M. Lane. "Energy-constrained informative routing for AUVs". In: *OCEANS 2016 - Shanghai* (2016). DOI: 10.1109/OCEANSAP.2016.7485386 (cited on page 15).

[120] Georgios Fagogenis, David Flynn, and David M. Lane. "Improving underwater vehicle navigation state estimation using locally weighted projection regression". In: *2014 IEEE International Conference on Robotics and Automation* (2014), pages 6549–6554. DOI: 10.1109/ICRA.2014.6907825 (cited on page 15).

[121] David M. Lane, Francesco Maurelli, Petar Kormushev, Marc Carreras, Maria Fox, and Konstantinos Kyriakopoulos. "PANDORA - Persistent autonomy through learning, adaptation, observation and replanning". In: *IFAC-PapersOnLine* 28.2 (2015), pages 238–243. DOI: 10.1016/j.ifacol.2015.06.039 (cited on page 15).

[122] Ioan A. Sucan and Sachin Chitta. *Moveit!* http://moveit.ros.org. [Online; accessed 19-July-2018] (cited on page 117).

[123] James J Kuffner and Steven M LaValle. "RRT-Connect : An Efficient Approach to Single-Query Path Planning". In: *IEEE International Conference on Robotics And Automation*. April. 2000, pages 995–1001 (cited on page 117).

[124] Kaustubh Pathak, Andreas Birk, Narunas Vaskevicius, Max Pfingsthorn, Sören Schwertfeger, and Jann Poppinga. "Online Three-Dimensional SLAM by Registration of Large Planar Surface Segments and Closed-Form Pose-Graph Relaxation". In: *Journal of Field Robotics* 27.1 (2010), pages 52–84. DOI: 10.1002/rob.20322 (cited on page 121).

[125] Renato F. Salas-Moreno, Richard a. Newcombe, Hauke Strasdat, Paul H.J. Kelly, and Andrew J. Davison. "SLAM++: Simultaneous Localisation and Mapping at the Level of Objects". In: *2013 IEEE Conference on Computer Vision and Pattern Recognition* (June 2013), pages 1352–1359. DOI: 10.1109/CVPR.2013.178 (cited on page 121).

[126] Peter Henry, Michael Krainin, Evan Herbst, Xiaofeng Ren, and Dieter Fox. "RGB-D mapping: Using depth cameras for dense 3D modeling of indoor environments". In: *Springer Tracts in Advanced Robotics* 79 (2014), pages 477–491. DOI: 10.1007/978-3-642-28572-1_33 (cited on page 121).

[127] Xuming Ge. "Non-rigid registration of 3D point clouds under isometric deformation". In: *ISPRS Journal of Photogrammetry and Remote Sensing* 121 (2016), pages 192–202. DOI: 10.1016/j.isprsjprs.2016.09.009 (cited on page 122).